Ultralong-range Rydberg molecules: Investigation of a novel binding

Vera Bendkowsky

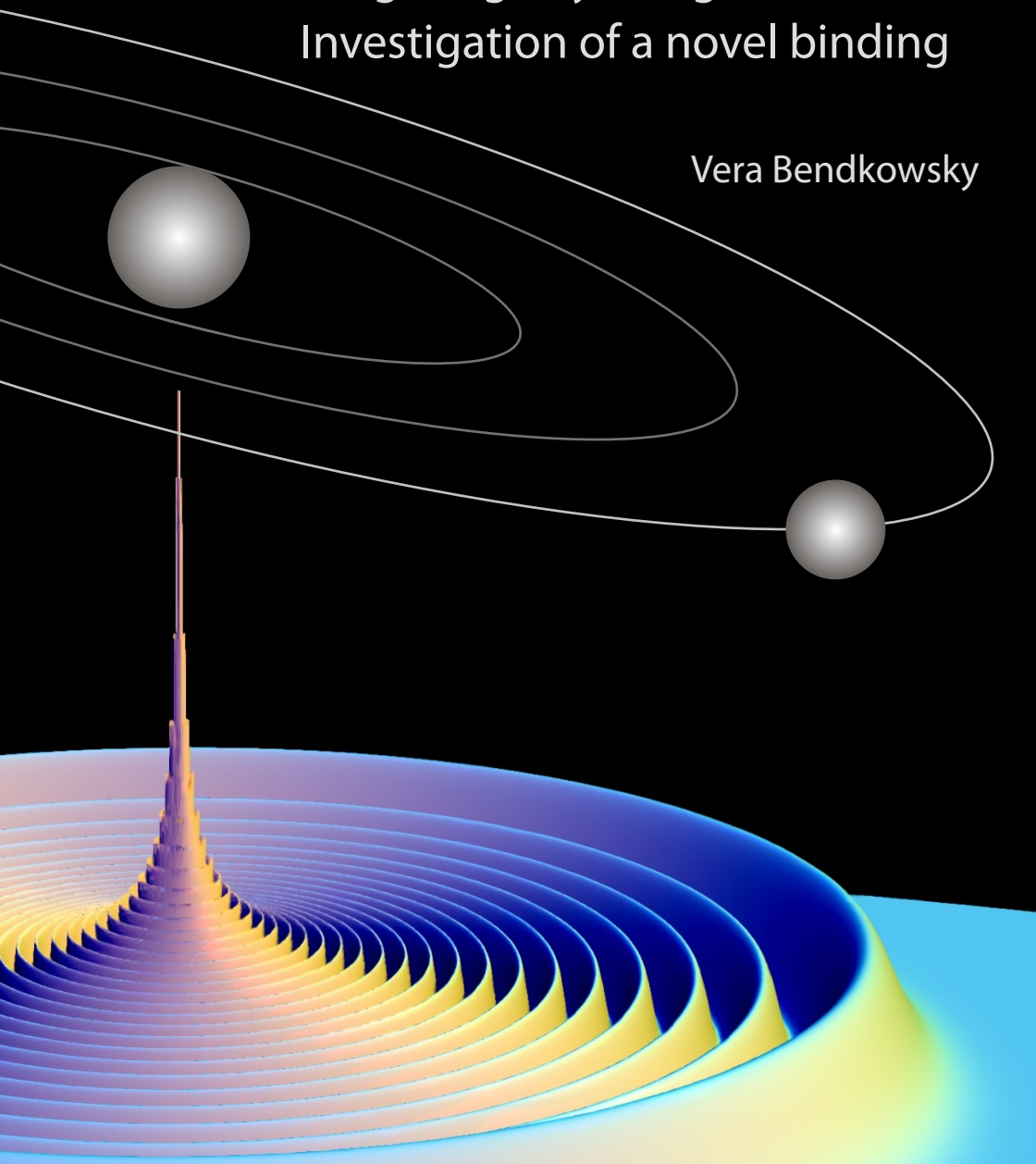

2010

ULTRALONG–RANGE RYDBERG MOLECULES:

INVESTIGATION OF A NOVEL BINDING

Von der Fakultät Mathematik und Physik der
Universität Stuttgart zur Erlangung der Würde eines
Doktors der Naturwissenschaften (Dr. rer. nat.)
genehmigte Abhandlung

vorgelegt von

Vera Bendkowsky

aus Bassum

Betreuer und Hauptberichter:	Prof. Dr. Tilman Pfau
Mitberichter:	Prof. Dr. Uwe Schumacher
Prüfungsvorsitzender:	Prof. Dr. Günter Wunner
Tag der mündlichen Prüfung:	24.03.2010

Physikalisches Institut der Universität Stuttgart

2010

Diese Arbeit wurde angefertigt am

5. Physikalischen Institut
Universität Stuttgart
Pfaffenwaldring 57
D-70569 Stuttgart

A molecule that until now existed only in theory has finally been made.

BBC News

Vorwort

Diese Arbeit beschäftigt sich mit langreichweitigen Rydberg-Molekülen. Sie sind nur sehr schwach gebunden und deshalb nur unter speziellen Bedingungen erzeugbar und nachweisbar. Darin liegt auch der Grund, weshalb ihre Existenz zwar schon lange von Theoretikern angenommen wurde, bisher aber nicht im Experiment gezeigt werden konnte. Es gab schon früh Hinweise auf diese Art von Molekülen, beginnend mit den Arbeiten der Italiener Edoardo Amaldi, Emilio Segrè [1] und Enrico Fermi [2] im Jahr 1934, bis hin zu neueren Daten von Niemax und Kollegen von 2006 [3]. Aber bisher fehlte der "Beweis" ihrer Existenz in der Form, daß sie gezielt erzeugt und isoliert studiert werden konnten. Genau darum wird es in dieser Arbeit gehen.
Aber ich möchte hier vorn beginnen, nicht etwa im chronologischen Sinne, sondern mit der Frage: Was sind langreichweitige Rydberg-Moleküle?
Als die erste Veröffentlichung zu dieser Arbeit entstand, nahm meine Großmutter ihr Lexikon zur Hand und schlug nach:

Rydberg-Konstante *(nach dem schwedischen Physiker Johannes R. Rydberg, * 1854, † 1919), Formelzeichen R, atomphysikalische Konstante in den Serienfolgen für die Spektrallinien:* $R_\infty = 1,0974 \cdot 10^7\ m^{-1}$.

Molekül *(frz.), Baustein der Materie; besteht aus mindestens zwei, bei chemischem Element gleichartigen, bei chemischer Verbindung verschiedenartigen Atomen.*

Meyers Taschenlexikon

Damit ist die Frage natürlich noch nicht beantwortet, aber es ist ein Anfang. Langreichweitige Rydberg-Moleküle bestehen aus einem Rydberg-Atom und einem (oder mehreren) Atomen im Grundzustand. Sie werden von einem besonderen Bindungsmechanismus zusammengehalten, den es bei chemischen Bindungen nicht gibt und der dafür verantwortlich ist, daß die Bindungslänge, d.h. der Abstand der Atome, etwa 100mal größer ist als bei normalen Molekülen.
Unter einem Rydberg-Atom versteht man ein Atom, bei dem ein Elektron hochangeregt und nur noch schwach an den Rest des Atoms

gebunden ist. Dadurch verhält sich das Elektron nahezu klassisch: in Analogie zum Planetenmodell kreist es auf einer Bahn mit sehr großem Durchmesser um den Atomrumpf (s. Abb.) und je größer der Bahndurchmesser ist, desto langsamer wird auch die Umlaufgeschwindigkeit des Elektrons. Diese hochangeregten Zustände gibt es bei Atomen aller chemischen Elemente und man bezeichnet die Atome nach ihrem schwedischen Entdecker Johannes Rydberg als Rydberg-Atome und das zugehörige Elektron auch als Rydberg-Elektron.
Der Bindungsmechanismus der langreichweitigen Rydberg-Moleküle beruht ausschließlich auf dem Einfluß des Rydberg-Elektrons auf das zweite Atom: Es wird im elektrischen Feld des Elektrons polarisiert und dadurch an das Rydberg-Atom gebunden. Die Größe des Moleküls wird deshalb direkt durch die Umlaufbahn des Rydberg-Elektrons bestimmt. Damit zählt dieses Molekül mit einem Durchmesser von mehr als 100 Nanometern zu den größten bekannten zweiatomigen Molekülen.
Quantenmechanisch bewegen sich die Elektronen in einem Atom allerdings nicht auf Kreisbahnen, sondern haben eine räumliche Verteilung, die durch die Wellenfunktion beschrieben wird. Vom Zentrum des Rydberg-Atoms ausgehend besitzt diese Verteilung abwechselnd Maxima und Minima (s. Abb.). Dort, wo das Maximum am größten ist, ist auch die Wahrscheinlichkeit am größten, das Elektron anzutreffen. Hier liegt die klassische Bahn des Elektrons. Damit sich nun ein Rydberg-Molekül bilden kann, muß sich genau in diesem Abstand ein Atom im Grundzustand befinden.

Soweit die anschauliche Darstellung der Theorie der Bindung. Formal wird sie als Streuproblem behandelt: Da das Coulomb-Feld des Elektrons kugelsymmetrisch ist, kann der Streuprozeß durch Partialwellen beschrieben werden [4], und da die kinetische Energie des Elektrons im Bereich von 1 meV liegt und damit sehr klein ist, trägt nur die s-Welle signifikant zum Wechselwirkungspotential des Rydberg-Elektrons mit dem Grundzustandsatom bei. Bereits die Zentrifugalbarriere der p-Welle ist mit 171 meV so groß, daß Beiträge der p-Welle und aller höheren Wellen zum Streuprozeß vernachlässigt werden können. Aus einer quantenmechanischen Behandlung der Elektron-Atom-Streuung folgt außerdem, daß die Wechselwirkung

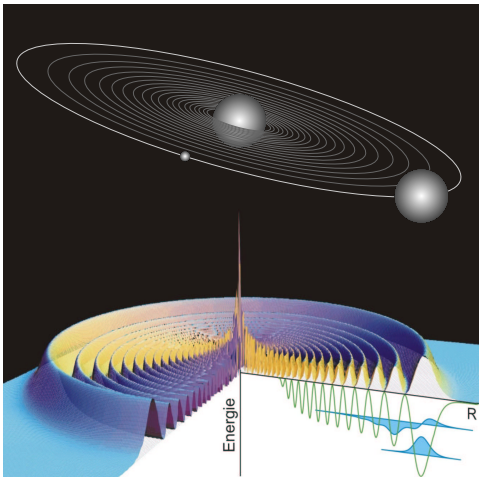

zwischen Elektron und Atom nicht grundsätzlich attraktiv ist, sondern abhängig von der elektronischen Struktur des Grundzustandsatoms auch repulsiv sein kann. Art und Stärke der Wechselwirkung mit einem Elektron werden durch die Streulänge A eines Atoms ausgedrückt, die positiv oder negativ sein kann [2], und folglich die Wechselwirkung repulsiv oder attraktiv.

Der Franzose Alain Omont verwendete 1977 das Konzept des Pseudopotentials von E. Fermi [2] und leitete die Molekülpotentiale erstmals her [5]. Zu diesem Zeitpunkt fehlten aber noch zwei wichtige technische Voraussetzungen für die Erzeugung der langreichweitigen Rydberg-Moleküle: die Entwicklung schmalbandiger Laser zur Adressierung der Molekülzustände sowie die Methoden der Laser- und evaporativen Kühlung zur Erzeugung ultrakalter Gase mit hoher Teilchenzahldichte.
Die Methoden der Laserkühlung wurden in den 90er Jahren des letzten Jahrhunderts entwickelt und fanden ihren Höhepunkt in der Bose-Einstein Kondensation eines ultrakalten Gases. Sowohl die Laserkühlung als auch die Bose-Einstein Kondensation wurden mit einem Nobel-Preis ausgezeichnet[1]: 1997 erhielten Steven Chu, Claude

[1]Für detaillierte Informationen siehe Homepage der Nobel Stiftung http://nobelprize.org/nobelprizes/physics/laureates/

Cohen-Tannoudji und William D. Philips die Auszeichnung für "die Entwicklung der Methoden zum Kühlen und Fangen von Atomen mit Laserlicht" und im Jahr 2001 wurde der Nobelpreis Eric A. Cornell, Wolfgang Ketterle und Carl E. Wieman für "das Erreichen der Bose-Einstein Kondensation in verdünnten Gasen von Alkali-Atomen, und für frühe fundamentale Untersuchungen der Eigenschaften von Kondensaten" verliehen.
Bereits ein Jahr früher erkannte der Amerikaner Chris Greene, daß die hohen Dichten in einem Bose-Einstein Kondensat und das Ausfrieren der thermischen Bewegung der Atome es erlauben könnten, die langreichweitigen Rydberg-Moleküle endlich im Labor zu erzeugen. Denn erst bei Temperaturen um 1 μK bewegen sich die Atome so wenig, daß ein Grundzustandsatom tatsächlich an ein Rydberg-Atom gebunden werden kann. Außerdem erfordert die Erzeugung der Rydberg-Moleküle Abstände zwischen den Atomen, die der Bindungslänge entsprechen, die also nur etwa 100 nm betragen. Solch kleine Abstände oder hohe Dichten lasssen sich in einem Gas nur bei extrem niedrigem Druck und niedriger Temperatur erreichen. Chris Greene veröffentlichte im Jahr 2000 erstmals konkrete Rechnungen zu Molekülpotentialen für Rubidium und deren Vibrationsspektren [6]. Die Abbildung zeigt das s-Wellen-Potential des Zustands 35s in Rubidium und die zugehörigen gebundenen Molekülzustände, die neben anderen Zuständen in dieser Arbeit untersucht werden. Das Molekülpotential spiegelt die radiale Wellenstruktur der Aufenthaltswahrscheinlichkeit des Rydberg-Elektrons wider und jeder "Berg" in der Aufenthaltswahrscheinlichkeit führt zu einem Minimum im Potential. Der tiefste dieser Potentialtöpfe rührt vom äußersten "Berg" - der klassischen Bahn des Elektrons - her. Er besitzt zwei gebundene Zustände, d. h. in diesem Abstand vom Zentrum des Rydberg-Atoms wird das zweite Atom durch das Elektron gebunden. Die eingezeichneten Wellenfunktionen beschreiben die Schwingungsbewegung des Grundzustandsatoms im Potential, die sich im Experiment als Vibrationsspektrum beobachten läßt.

In dieser Arbeit werden die langreichweitigen Rydberg-Moleküle für Rb(ns) Zustände durch Photoassoziation erzeugt und ihre grundlegenden Eigenschaften untersucht. Die Messungen umfassen Photoassoziationsspektren für Hauptquantenzahlen n zwischen 34 und

40, in denen die Vibrationsstruktur der Rydberg-Moleküle erstmals aufgelöst werden kann. Die Abhängigkeit der Bindungsenergie des Schwingungsgrundzustands $\nu = 0$ von der Hauptquantenzahl wird systematisch studiert und mit theoretischen Vorhersagen verglichen. Dabei zeigt sich, daß das theoretische Modell für eine Streulänge von $A = -18.0$ Bohr-Radien für die Elektron-Atom-Streuung in Rubidium hervorragend mit den experimentellen Ergebnissen übereinstimmt [7]. Neben dem Vibrationsspektrum werden der Stark-Effekt und die Lebensdauern der langreichweitigen Rydberg-Moleküle untersucht. Während die Polarisierbarkeiten der Rydberg-Moleküle gut mit denen der Rydberg-Atome übereinstimmen und damit das theoretische Modell bestätigen, zeigen die Rydberg-Moleküle deutlich verkürzte Lebensdauern. Diese Beobachtung steht im Gegensatz zu der Annahme des Modells, daß die Wellenfunktion des Rydberg-Atoms durch die Präsenz des Grundzustandsatoms nicht beeinflußt wird. Ferner werden molekulare Ionen Rb_2^+ im Experiment identifiziert, die eindeutig auf einen Zerfallskanal unter Mitwirkung des Grundzustandsatoms hinweisen.
Neben den Untersuchungen von zweiatomigen Rydberg-Molekülen wird in dieser Arbeit die Photoassoziation von dreiatomigen Molekülen demonstriert, sogenannter Trimere, bei denen ein Rydberg-Atom zwei Grundzustandsatome an sich bindet. Dabei kann die Wechselwirkung zwischen den Grundzustandsatomen vernachlässigt werden, wie hier anhand der Bindungsenergien der Trimere für Hauptquantenzahlen von $n = 35 - 37$ gezeigt werden kann.

Damit weisen diese Messungen den Weg zu komplexeren Systemen, denn die bindende Kraft des Rydberg-Elektrons ist weder auf ein einzelnes Grundzustandsatom beschränkt, noch müssen Rydberg- und Grundzustandsatom grundsätzlich von derselben Spezies sein. Größere polyatomare Moleküle oder sogar heteronukleare Moleküle könnten zukünftig realisiert werden. Einzige Anforderung an die beteiligten chemischen Elemente ist eine negative Streulänge der Grundzustandsatome, damit ein attraktives Molekülpotential entsteht. Das heißt das chemische Element des Rydberg-Atoms spielt keine Rolle: Sogar gebundene Zustände zwischen einem chemisch gebundenen Molekül im Rydberg-Zustand und einem oder mehreren Grundzustandsatomen sind denkbar. Die Realisierung solch exoti-

scher Moleküle liegt aber wohl noch in weiter Ferne, denn die Kühlung von Molekülen in den Bereich von wenigen Mikrokelvin ist heute noch auf wenige chemische Verbindungen beschränkt [8, 9, 10] und erfordert sehr großen experimentellen Aufwand [11, 12].

Journal Publications

Parts of the work described in this thesis are published in the following articles:

- V. Bendkowsky, B. Butscher, J. Nipper, J. P. Shaffer, R. Löw, and T. Pfau
  Observation of ultralong-range Rydberg molecules
  Nature **458**, 1005 (2009)
- V. Bendkowsky, B. Butscher, J. Nipper, J. P. Shaffer, R. Löw, T. Pfau, W. Li, J. Stanojecic, T. Pohl, and J. M. Rost
  Rydberg trimers and excited dimers bound by internal quantum reflection
  submitted, arXiv:0912.4058

Additionally, an article for the general reader is published:

- B. Butscher, V. Bendkowsky, T. Pfau
  Moleküle aus Rydberg-Atomen
  Physik in unserer Zeit **40**, 173(2009)

Furthermore, the following articles by other scientists comment on the results presented in this thesis:

- Chris H. Greene
  News&Views: The little molecule that could
  Nature **458**, 975 (2009)
- S. D. Hogan and F. Merkt
  A New Perspective on the Binding Power of an Electron
  ChemPhysChem **10**, 2931 (2009)

Contents

1. Introduction

In the early days of the 20th century, scientists started systematic scattering experiments with electrons and α particles to study the structure of matter. The most famous ones are probably the experiments by Ernest Rutherford: In 1911, he explored the transmission of α and β particles through thin plates of different metals and observed "large single deflexions of the α and β particles", but most of the particles passed the plates just undistorted [13]. These measurements are the foundation of our today's picture about the composition of atoms. In 1934, the Italian scientists Edoardo Amaldi and Emilio Segrè worked with gases of alkali: they took absorption spectra of highly excited states and studied the influence of the presence of a foreign gas at high pressure [1]. They found that, in contrast to their expectation, the atomic lines were shifted without broadening the lines excessively. Thus the spectra could not be explained simply by a pressure broadening. Furthermore, even the sign of the observed line shifts seemed to depend on the foreign gas. Enrico Fermi attributed the line shifts to the scattering of the valence electron of the alkali with the foreign gas atoms and developed a simple pseudopotential to describe their interaction [2]. Therefore, he introduced the concept of *scattering length* which includes the repulsive or attractive character of the scattering process and quantifies the strength of the electron-atom interaction.
Collisions of electrons and atoms were further studied in the following decades with the aim to improve the theoretical model. Today, the highly excited states Amaldi and Segrè studied in 1934 are called Rydberg states. Their characteristic are their universal properties, as due to the large separation between atomic core and valence elec-

tron, they can be considered as hydrogenlike systems. The electronic structure of the atomic core has only a weak influence on the Rydberg electron and thus Rydberg atoms of all species have similar properties which strongly depend on the principal quantum number, n. Sophisticated descriptions of Rydberg wavefunctions and predictions for the scattering lengths and cross sections improved the understanding regarding the validity of the model assumptions.
Based on the approach by Fermi, the French physicist Alain Omont calculated the interaction potential for electron-atom scattering of a weakly bound Rydberg electron and an atom in the ground state in 1977 [5]. His formula for the interaction potential comprehends already the criteria for the existence of bound states between the Rydberg atom and the ground state atom. But at that time, it was not imaginable to create these weakly bound and fragile molecules in the laboratory, as the thermal energy in any gas was much larger than the interaction energies between the Rydberg electron and a ground state atom.

It was not until the year 2000, after the achievement of Bose-Einstein condensation of alkali, that Chris Greene rediscovered Omont's work and recognized, that the high densities and the extremely low temperatures of a Bose-Einstein condensate or even of an ultracold sample of rubidium atoms could allow for the formation of ultralong-range Rydberg molecules [6]. These bound states between a Rydberg atom and an atom in the ground state arises solely from the electron-atom scattering of the Rydberg electron with the ground state atom. For chemical elements with a negative scattering length like rubidium, the interaction is attractive and the ground state atom is bound to the "orbit" of the electron (see Fig.). From a classical point of view, the ground state atom is polarized by the electron and thus bound to the Rydberg atom. In a quantum mechanical treatment, the probability density of the Rydberg electron has to be taken into account, which is shown in the Figure for the state 35s of rubidium together with the resulting molecular potential:
The oscillatory character of the probability density is reflected in the molecular potential which consists of a large number of potential wells. The deepest potential well arises from the last lobe of

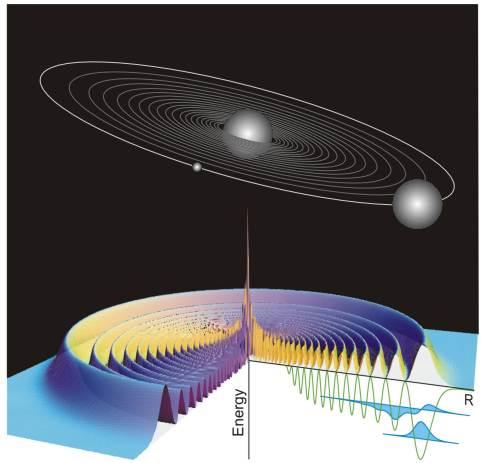

the wavefunction which corresponds to the classical turning point of the Rydberg electron. It supports two bound states, the vibrational ground state and one excited state.
Chris Greene was the first to calculate the molecular potential curves in rubidium for the principal quantum number $n = 30$ [6]. He showed that the binding energies of the molecular states strongly depend on the angular momentum, l, of the Rydberg electron: They range from several $h \cdot 10$ MHz for $l = 0$ to several $h \cdot 10$ GHz for $l \geq 3$, the hydrogenlike states in rubidium. The bond length of the ultralong-range Rydberg molecules are determined by the size of the Rydberg wavefunction and are thus on the order of 100 nm. These values make clear that the requirements for the creation of these molecules, i. e. atomic samples with firstly thermal energies well below the molecular binding energies, and secondly high densities to provide for interatomic separations equal to the bond length of the molecular state, are only fulfilled by an ultracold gas of atoms close to the temperature where quantum degeneracy occurs.

This work reports on the first formation of these ultralong-range Rydberg molecules in the laboratory and presents studies of their fundamental properties. The Rydberg molecules are created by pho-

toassociation from a dense and cold sample of ^{87}Rb atoms to the molecular triplet states $^3\Sigma(ns - 5s)$. The measurements cover photoassociation spectra for principal quantum numbers, n, between 34 and 40, in which the vibrational structure of the Rydberg molecules is clearly resolved. The dependence of the binding energy of the vibrational ground state $\nu = 0$ on the principal quantum number is studied systematically and compared to the theoretical predictions by Chris Greene. It is shown that the theoretical model is in excellent agreement with the experimental data if a s-wave scattering length of $A = -18.0$ Bohr radii is assumed [7].
Aside from the vibrational spectrum, also the Stark effect and the lifetimes of the ultralong-range Rydberg molecules are investigated. The polarizabilities of the Rydberg molecules are in good agreement with those of the atomic Rydberg states and confirm the assumption of the theoretical model that the Rydberg wavefunction is not perturbed by the presence of the ground state atom. In contrast to these results, the Rydberg molecules show significantly shorter lifetimes than the Rydberg atoms. Furthermore, molecular ions Rb_2^+ are detected in the experiment, which is a clear indication for a decay channel of the ultralong-range Rydberg molecules initiated by the presence of the ground state atom.
Finally, the photoassociation of triatomic Rydberg molecules is demonstrated, in which one Rydberg atom Rb(ns) binds even two ground state atoms simultaneously. In these Rydberg trimers, any interaction of the two ground state atoms can be neglected, as can be shown from their binding energies for principal quantum numbers $n = 35 - 37$.

These results pave the way towards the formation of more complex systems, as the binding force of the Rydberg electron is neither limited to a single ground state atom, nor do the constituents have to be of the same atomic species. In the future, larger polyatomic molecules or even heteronuclear molecules could be formed. The only requirement to the bound ground state atoms is a negative scattering length for electron collisions to allow for attractive molecular potentials.
In general, there are no restrictions for the chemical element of the Rydberg atom: even bound states between a chemically bound

molecule in a Rydberg state and one or more ground state atoms are imaginable. But the realisation of such exotic molecular states is a distant prospect, as the cooling of chemically bound molecules today is restricted to only few chemical bindings [8, 9, 10] and requires tremendous experimental effort [11, 12].

2. Theoretical foundations

Atoms of a certain species with one valence electron in a highly excited electronic state are called Rydberg atoms. They are of special interest for two reasons: Firstly, the small overlap between the wavefunction of the electron, in the following called Rydberg electron, and the atomic nucleus - consisting of the core and the remaining atomic shell - makes it possible to consider the Rydberg atom as hydrogen-like system. The Rydberg electron experiences the nucleus as a pointlike ion with net charge +1, and aside from small deviations the energies and wavefunctions can be described by the well-known solutions of the hydrogen atom.
But more importantly, the large separation between nucleus and Rydberg electron makes these atoms extremely sensitive to multipole forces and leads to giant dipole moments, polarizabilities, dipole-dipole or van der Waals interactions compared to those of ground-state atoms. These facts build the groundwork for precise studies of fundamental phenomena which are not accessible in other atomic systems.

In this work a new type of binding between a Rydberg atom and a ground state atom is studied. It is based entirely on the interaction of the Rydberg electron and a ground-state atom which is polarized by the electron and thus bound to the Rydberg electrons' orbit. Consequently, the molecular potential reflects the probability density of the Rydberg electron. Following the proposal by C. Greene and coworkers [6] the molecular potential can be modelled by pure s-wave scattering, whereas the probability density of the Rydberg electron has to be taken into account.

Thus the first part of this chapter (2.1) deals with general properties of Rydberg atoms, followed by treatments of calculating Rydberg wavefunctions (2.1.1), lifetimes (2.1.2) and the Stark effect of Rydberg states (2.1.3). Finally their interactions, especially the van der Waals interaction, are discussed (2.1.4). The second part focusses on the electron-atom scattering (2.2) giving rise to a new type of binding which is the topic of this thesis. Chapter 2.2.1 introduces the basic concepts of scattering theory before the molecular potentials arising from s-wave scattering are discussed (2.2.2). In the final part (2.3) the basic properties of diatomic molecules are summarized, starting with their symmetries and the conventional notation for molecular states. After a brief overview on the vibrational and rotational degrees of freedom (2.3.1) it focusses on the rotational structure of molecular Stark spectra (2.3.2). The photoassociation of ultracold molecules and their resulting properties, e.g. the populated molecular states and the expected linewidths, are discussed in chapter 2.3.3.

2.1 Rydberg atoms

The fact that one valence electron is in a highly excited state makes the Rydberg atom comparable to the hydrogen atom. The Rydberg wavefunction vanishes at the atomic core - consisting of the nucleus of charge $Z \cdot e$ and $Z-1$ electrons - and therefore the Rydberg electron experiences it - just like in the case of hydrogen with atomic number $Z = 1$ - as a point charge $+e$.
The electronic structure of the core plays a role only for those Rydberg states which have a non-vanishing probability density at the nucleus, i. e. the states with low angular momentum l. For these states, the nucleus is not shielded completely by the $Z-1$ electrons, meaning the electron in a low-l state experiences a larger effective atomic number $Z > 1$ and is therefore deeper bound than one with the same principal quantum number n but in a high-l state. The influence of the atomic nucleus on the binding energy can be taken into account by introducing a state dependent quantum defect δ_{nlj} and an effective principal quantum number $n^* = n - \delta_{nlj}$. Then the binding energies E_{nl} can be expressed in analogy to the hydrogen atom as

$$E_{nl} = -\frac{R_\infty}{(n-\delta_{nlj})^2}\,, \tag{2.1}$$

where $R_\infty = \frac{e^4 m_e}{8\epsilon_0^2 h^3 c} = 1.097 \cdot 10^7 m^{-1}$ is the Rydberg constant. In the case of rubidium the ionization energy of the ground state Rb($5s$) measures $E_{5s} = -33\,690.80\ cm^{-1}$ [14].

Rubidium is an alkali metal with only one valence electron. If this electron is excited to a Rydberg state, the remaining nucleus Rb^+ has the electron configuration of krypton which has a closed shell and thus a small atomic radius. Therefore, only the quantum defects for states with low angular momentum l differ significantly from zero. The quantum defect of a certain state can be calculated by the Rydberg-Ritz formula [15]

$$\delta_{nlj} = \delta_0 + \frac{\delta_2}{(n-\delta_0)^2} + \frac{\delta_4}{(n-\delta_0)^4} + \frac{\delta_6}{(n-\delta_0)^6} + ... \tag{2.2}$$

state	$n^2s_{1/2}$	$n^2p_{1/2}$	$n^2p_{3/2}$	$n^2d_{3/2}$	$n^2d_{5/2}$	n^2f_j
δ_0	3.1311804	2.6548849	2.6416737	1.3480917	1.3464657	0.016312
δ_2	0.1784	0.2900	0.2950	-0.6029	-0.5960	-0.064007
δ_4	-1.8	-7.904	-0.97495	-1.50517	-1.50517	-0.36005
δ_6	-	116.4373	14.6001	-2.4206	-2.4206	3.239
δ_8	-	-405.907	-44.7265	19.736	19.736	-
ref.	[16]	[15, 16]	[15, 16]	[15, 16]	[15, 16]	[15]

Tab. 2.1: Quantum defect parameter for ^{85}Rb.

where the coefficients $\delta_0, \delta_2, \delta_4, \delta_6$ and δ_8 have to be derived from spectroscopic data of a large range of Rydberg states. The coefficients for rubidium are summarized in Tab. 2.1. Only for s, p and d states the coefficients differ significantly from zero. Thus the Rydberg states of rubidium can be divided in two classes: the low-l states which are non-degenerate and the high-l states ($l > 3$) which are degenerate and thus show a linear Stark effect.

The classical Bohr atom

The small binding energy and the on average large separation between the Rydberg electron and the atomic nucleus makes the Rydberg atom to a quasi-classical "Bohr atom" showing the typical scaling of the properties with principal quantum number n. They can be derived from the quantization of the angular momentum L:

$$L = m_e v r \stackrel{!}{=} n\hbar \,. \tag{2.3}$$

and the classical condition

$$m_e \frac{v^2}{r} = \frac{1}{4\pi\epsilon_0} \frac{Ze^2}{r^2} \tag{2.4}$$

stating that the centrifugal force on the electron e moving on its orbit with radius r and velocity v has to be equal to the Coulomb force by the nucleus with charge Ze [17].
Tab. 2.2 summarizes the classical results. They can be used to deduce the n-dependence also for quantum mechanical properties, e.g.

- dipole moment $d = \langle nl \,|er|\, nl' \rangle \propto n^{*2}$

- polarizability $\alpha = \frac{d^2}{E_n - E_m} \propto n^{*7}$
- van der Waals interaction $C_6 = -\frac{(d_1 d_2)^2}{E_n - E_m} \propto n^{*11}$.

property	formula	scaling	Rb(35s)
binding energy	$E_n = -\frac{R_\infty}{n^{*2}}$	n^{*-2}	-108.05 cm^{-1}
level separation	$E_n - E_{n-1} \cong -\frac{2R_\infty}{n^*(n^*-1)^2}$	n^{*-3}	7.11 cm^{-1}
orbit radius	$r_n = \frac{4\pi\epsilon_0 \hbar^2 n^{*2}}{Ze^2 m_e}$	n^{*2}	998 a_0
class. velocity	$v_n = \frac{Ze^2}{4\pi\epsilon_0 \hbar n^*}$	n^{*-1}	48 mm/μs
Kepler period	$T_n = 2\pi \left(\frac{4\pi\epsilon_0}{Ze^2}\right)^2 \frac{\hbar^3 n^{*3}}{m_e}$	n^{*3}	4.8 10^{-12}s
kin. energy	$E_{kin} = \frac{1}{8\pi\epsilon_0}\frac{Ze^2}{r_n} = -\frac{1}{2}E_n$	n^{*-2}	6.7 meV

Tab. 2.2: Scaling of fundamental properties with principal quantum number n and examples for $Rb(35s)$.

Field ionization

The electron of a Rydberg atom has binding energies on the order of 100 cm^{-1} and compared to the ionization energy of the Rb(5s) ground state of $E_{5s} = -33\,690.80$ cm^{-1} it is only loosely bound. The energy for separating the Rydberg electron completely from the atom can be provided by only moderate electric fields. Therefore field ionization is a widely used technique for detecting Rydberg atoms. The effect of a constant electric field F in z-direction on a Rydberg atom is shown in Fig. 2.1. The additional electric field tilts the Coulomb potential and leads to an anisotropic potential

$$V_F(x,y,z) = -\frac{e^2}{4\pi\epsilon_0}\frac{1}{\sqrt{x^2+y^2+z^2}} + eFz \tag{2.5}$$

with a local maximum at

$$x = y = 0,\ z = z_b = -\sqrt{\frac{e}{4\pi\epsilon_0 |F|}}\,. \tag{2.6}$$

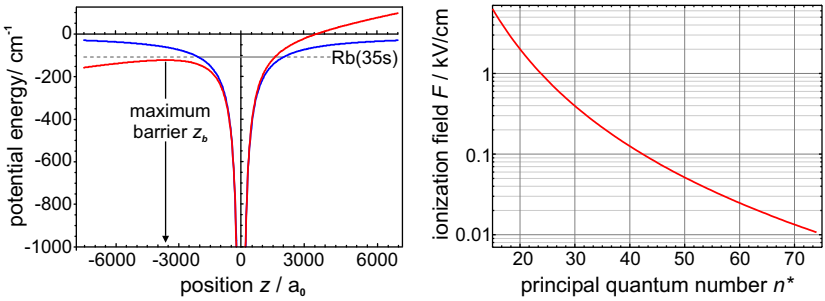

Fig. 2.1: Left: Atomic Coulomb potential (blue) and atomic potential in the presence of an electric field $F = 400$ V/cm (red). The atomic potential is lowered for $z < 0$ and the electron in the Rb(35s) state is no longer bound. Right: Scaling of the classical limit for field ionization with principal quantum number n^*.

Only electrons with binding energies $E_{n,l}$ lower than the local maximum $V_F(0,0,z_b)$ are classcially bound. The required electric field F for ionizing the Rydberg atom can be estimated by comparing the height of the barrier $V_F(0,0,z_b)$ with the binding energy:

$$V_F(0,0,z_b) = -\sqrt{\frac{e^3\,|F|}{\pi\epsilon_0}} \stackrel{!}{=} -\frac{R_\infty}{n^{*2}} \tag{2.7}$$

$$\Rightarrow \quad |F| = \frac{\pi\epsilon_0 R_\infty^2}{e^3\,n^{*4}} \tag{2.8}$$

$$= 3.2136\cdot 10^5\ \frac{\text{kV}}{\text{cm}}\cdot\frac{1}{n^{*4}}\,.$$

Although this condition neglects the Stark shift of the Rydberg levels and tunneling of the electron through the barrier it gives a good approximation, and the predictions for the ionization fields are close to the experimental observations.

2.1.1 Wavefunctions

The knowledge of the radial probability density of the Rydberg electron is crucial for the determination of the potentials of the long-range Rydberg molecules. Therefore it is not enough to approximate the rubidium wavefunctions by the analytic solutions of hydrogen. Instead, the radial wavefunctions $R(r)$ of the rubidium Rydberg states are calculated by solving the Schrödinger equation for the hydrogen atom (in a.u.)

$$-\frac{\partial^2 R}{\partial r^2} - \frac{2}{r}\frac{\partial R}{\partial r} + \left[\frac{l(l+1)}{r^2} - \frac{2}{r} + V_c\right] R(r) = -\frac{1}{n^{*2}}\, R(r), \quad (2.9)$$

where additionally the quantum defect $\delta_{nlj} = n - n^*$ and the core polarization of rubidium

$$V_c = -\frac{1}{2} \cdot \frac{\alpha_c}{r^4} \quad (2.10)$$

have been taken into account. The quantum defects are calculated as described in eq. (2.2) and the core polarizability was measured by Litzén to be $\alpha_c = 9.023$ a.u. [18]. The numerical solving is necessary as the hydrogen wavefunctions R_{nl} are only defined for whole-number principal quantum numbers n. Thus the hydrogen solutions are a good approximation for the Rydberg wavefunction only if the quantum defect δ_l is close to a whole number.
The program used here for calculating the radial wavefunctions $R(r)$ was developed by A. Grabowski and is already described in his thesis [19]. Therefore only a short summary of its methods is given.

The radial wavefunctions $R(r)$ are oscillatory and the spacing between neighboring nodes decreases near the core. As the Numerov method used here and in [19] samples the wavefunction at equidistant positions the accuracy of the solutions would strongly depend on the distance from the core. This effect can be avoided by using a square-root scaling of the variable r. The scaling leads to sinusoidal solutions for a large range of radii r and was introduced by Bhatti et al. [20]. One has to make the following substitutions:

$$\begin{aligned} v &:= \sqrt{r} \\ \chi &:= r^{3/4}\, R(r) = v^{3/2}\, R(v^2) \end{aligned} \quad (2.11)$$

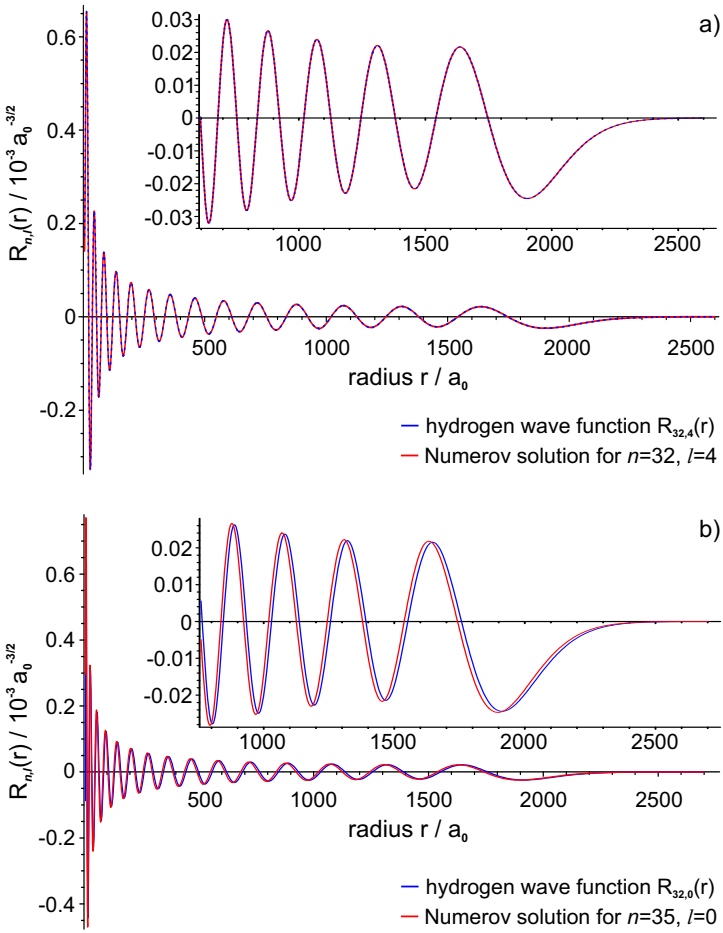

Fig. 2.2: Comparison of the radial wavefunctions $R_{n,l}(r)$ of the hydrogen atom (blue) and numerical calculations for rubidium (red). a) Solutions for the high-l state $n = 32, l = 4$. b) Wavefunction for the 35s state of rubidium (Numerov) and the corresponding $n^* = n - 3$, $l = 0$ hydrogen solution. The insets show the wavefunctions at higher resolution.

The normalization condition for the scaled wavefunction $\chi(v)$ then reads:

$$\begin{aligned} 1 &= \int_0^\infty R^2(r) r^2 dr = \int_0^\infty (\chi(v)\, v^{-3/2})^2\, v^4\, 2v\, dv \\ &= 2\int_0^\infty \chi^2(v) v^2 dv\,. \end{aligned} \tag{2.12}$$

Now the Schrödinger equation of the scaled wavefunction

$$\begin{aligned} -\frac{1}{(2v)^2}\frac{\partial^2\chi}{\partial v^2} + \left[\frac{3}{(4v)^2} + \frac{l(l+1)}{v^4} - \frac{2}{v^2} - \frac{1}{2}\frac{\alpha_c}{v^8}\right]\cdot\chi(v) \\ = -\frac{1}{(n-\delta_l)^2}\cdot\chi(v) \end{aligned} \tag{2.13}$$

which can also be written in the form

$$\begin{aligned} -\frac{\partial^2\chi}{\partial v^2} + \left[\frac{(2l+\frac{1}{2})(2l+\frac{3}{2})}{v^2} - 8 - \frac{2\alpha_c}{v^6}\right]\cdot\chi(v) \\ = -\frac{4v^2}{(n-\delta_l)^2}\cdot\chi(v) \end{aligned} \tag{2.14}$$

can be solved numerically by Numerov's method. As an example Fig. 2.2 shows the wavefunctions for Rb(35, $l = 0$) and Rb(35, $l > 3$) together with the analytic results for hydrogen and illustrates the influence of the quantum defects upon the solutions. For the high-l state both solutions are in perfect agreement. For low-l states, here the 35s state, the quantum defect has to be taken into account which is $\delta_0 = 3.131$ for rubidium (see Tab. 2.1). The hydrogen state closest to the 35s state is the n=32 manifold, corresponding to an effective quantum defect of $\delta_{\text{eff}} = 3$. Although the deviation between the quantum defect for s states δ_0 and δ_{eff} is only 4% the nodes of the Rb(35s) wavefunction are shifted significantly to smaller radii r compared to the hydrogen solution $R_{32,0}(r)$.

2.1.2 Lifetimes

In a two-level system, the probability for spontaneous decay $|nl\rangle \rightarrow |n'l'\rangle$ is given by the Einstein coefficient

$$A_{nl\rightarrow n'l'} = \frac{\omega^3_{nl\rightarrow n'l'}}{3\pi\epsilon_0\hbar c^3} \left|\langle n'l'| \, e\hat{r} \, |nl\rangle\right|^2 \tag{2.15}$$

with the transition frequency $\omega_{nl\rightarrow n'l'} = (E_{n'l'} - E_{nl})/\hbar$ and the transition dipole moment $d = \langle n'l'| \, e\hat{r} \, |nl\rangle$. The radiative lifetime of the state is given by the inverse of the Einstein coefficient

$$\tau_{rad}(nl) = \frac{1}{A_{nl\rightarrow n'l'}} \, . \tag{2.16}$$

For a Rydberg atom there is not only one but a variety of lower lying levels in which the Rydberg state can decay. Thus in eq. (2.16) the inverse of the sum over all coefficients has to be taken:

$$\tau_{rad}(nl) = \left[\sum_{n'l'} A_{nl\rightarrow n'l'}\right]^{-1} \tag{2.17}$$

As the Einstein coefficient contains a factor $\omega^3_{nl\rightarrow n'l'}$, which means aside from the influence of the dipole moment the transition with the highest energy contributes the most, the dominant decay channel is the decay to the ground state or the lowest lying allowed state. The ns states studied in this work will thus decay mainly to the deepestly bound p state, the $5p_{3/2}$ and $5p_{1/2}$.

The radiative lifetimes of rubidium have already been measured in the 1970ies for ns [21], np [22], nd [21] and nf states [23]. But as these measurements were performed with thermal gases, the accuracy was limited by collisions or superradiance [24]. More recently, the radiative lifetimes of Rb(ns), Rb(np) and Rb(nd) states and their n-dependence have been studied in a cold sample for $31 \leq n \leq 45$ [25] and those of Rb(ns) and Rb(nd) states also for $26 \leq n \leq 30$ [26, 27]. Their results confirm the measurements of ref. [22] and they found the following relation for the n dependence:

$$\tau_{rad}(nl) = \tau'(n - \delta_{nlj})^\gamma \, . \tag{2.18}$$

state	τ'_{th}/ns	γ_{th}	τ'_{ex}/ns	γ_{ex}
s	1.43	2.94	1.45 ± 0.03	3.02 ± 0.02
p	2.76	3.02	2.80 ± 0.03	3.01 ± 0.03
d	2.09	2.85	2.10 ± 0.02	2.89 ± 0.02

Tab. 2.3: Theoretical [28] and experimental [25] parameters for the n dependence of the radiative lifetime of ^{85}Rb as defined in eq. (2.18).

The experimental parameters $\tau'$and γ are given in Tab. 2.3 together with theoretical predictions. For all states, the exponent γ is close to 3. The n-dependence of the radiative lifetime for s, p, and d states given by eq. (2.18) is shown at the end of the paragraph in Fig. 2.5 for a larger range of principal quantum numbers. But first, the influence of the thermal radiation field on the lifetime of Rydberg states is discussed. It can cause transitions from the initial Rydberg state to neighbouring states by stimulated emission or absorption and can thus lead to a population transfer to other Rydberg states.

Blackbody radiation

Aside from spontaneous transitions in the optical range Rydberg states can also decay via microwave transitions to the neighbouring levels. But as discussed above, the Einstein A-coefficients (2.15) of these transitions are much weaker as their transition frequencies $\omega_{nl\rightarrow n'l'}$ are very small. Nevertheless these transitions can shorten the lifetime considerably as soon as the temperature of the environment T becomes comparable to or larger than the Rydberg level separation $k_BT \approx E_{nl} - E_{n'l'}$ [29]. In this case, the blackbody radiation field is no longer a quasi-static field with thermal frequencies much lower than any atomic transition frequency but it contains modes that are both resonant with an atomic transition and highly occupied with photon numbers $N >> 1$. Therefore stimulated processes cannot be neglected any more, where the population of the initial Rydberg state $|nl\rangle$ is transferred to neighbouring states $|n'l'\rangle$ by stimulated emission to or absorption from the thermal radiation field. The most likely

transitions from $|nl\rangle$ states occur to $|(n \pm 1)(l \pm 1)\rangle$ states which is due to the large spatial overlap of their wavefunctions [29].

The spectral energy density $u(\nu, T)$ of the thermal field is described by Planck's law of radiation

$$u(\nu) = \frac{8\pi h\nu^3}{c^3} \cdot \frac{1}{\exp\{h\nu/k_B T\} - 1} = \frac{A}{B} \cdot N(\nu, T)\,. \tag{2.19}$$

It consists of two terms: the ratio of the Einstein coefficients of a blackbody $A/B = 8\pi h\nu^3/c^3$ and the number of photons of energy $h\nu$, $N(\nu, T)$, which obey the Bose-Einstein statistic.
The distribution of $u(\nu, T)$ at room temperature $T = 300\ K$ is depicted in Fig. 2.3. It has its maximum at $\nu_0 = 18$ THz which is much smaller than the transition frequencies of the radiative decay, e. g. $|ns\rangle \rightarrow |5p\rangle$ corresponding to $\nu_{ns\rightarrow 5p} \cong 622$ THz. Therefore, the optical transitions responsible for the radiative decay are not affected by the thermal field. Although the transition frequencies relevant for the Rydberg states Rb($34s$) to Rb($40s$) studied in this work are in the range of several 10 GHz and thus far below the frequency at the maximum of the distribution $\nu_0 =$18 THz blackbody induced transitions shorten the lifetimes of these states considerably.
A simple model for calculating the contribution of blackbody induced transitions to the effective lifetime of a Rydberg state was introduced by Gallagher [30]. He used the fact that the Einstein coefficient $B_{nl\rightarrow n'l'}$ for stimulated emission or absorption $|nl\rangle \rightarrow |n'l'\rangle$ is given by the Einstein coefficient for spontaneous emission to the same state $A_{nl\rightarrow n'l'}$ times the number of photons in the thermal field at the transition frequency $\nu_{nl\rightarrow n'l'}$

$$\begin{aligned} B_{nl\rightarrow n'l'} &= N(\nu_{nl\rightarrow n'l'}, T) \cdot A_{nl\rightarrow n'l'} \\ &= \frac{A_{nl\rightarrow n'l'}}{\exp\{h\nu_{nl\rightarrow n'l'}/k_B T\} - 1}\,. \end{aligned} \tag{2.20}$$

For a microwave transition $ns \rightarrow np$ which has anyway a large dipole matrix element, eq. (2.20) shows that a sufficiently large number of photons N can increase the transition probability and partly compensate for the low transition frequency which is dominating the probability for spontaneous emission (2.15): At room temperature, the

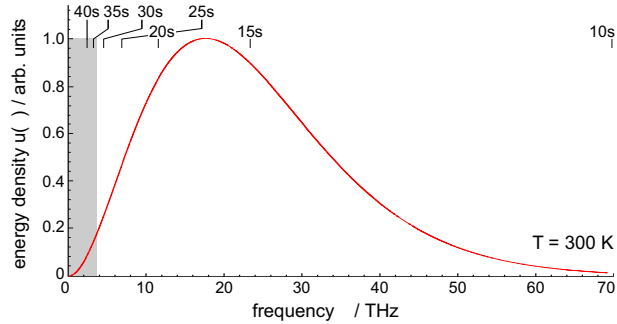

Fig. 2.3: Spectral distribution of the energy density of a blackbody at room temperature. The lines indicate the binding energies of rubidium Rydberg states Rb(ns) in frequencies E_{ns}/h and the shaded area the span in frequency relevant for the states $34s$ to $40s$ studied in this work.

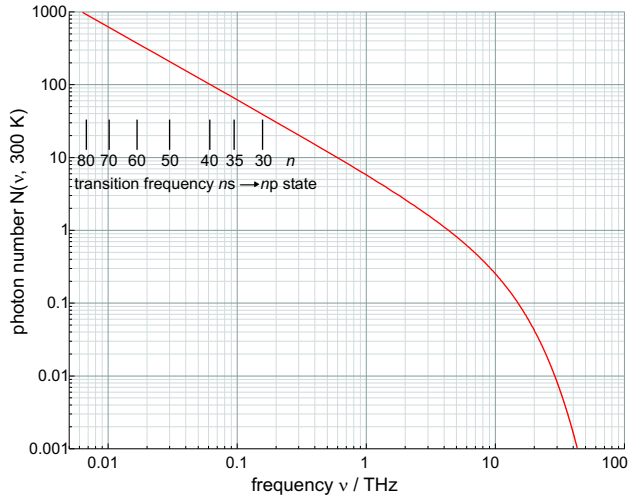

Fig. 2.4: Number of photons $N(\nu, T)$ in a thermal mode at room temperature. The transition frequencies to the nearest Rydberg level for $ns \rightarrow np$ transitions are given by vertical lines.

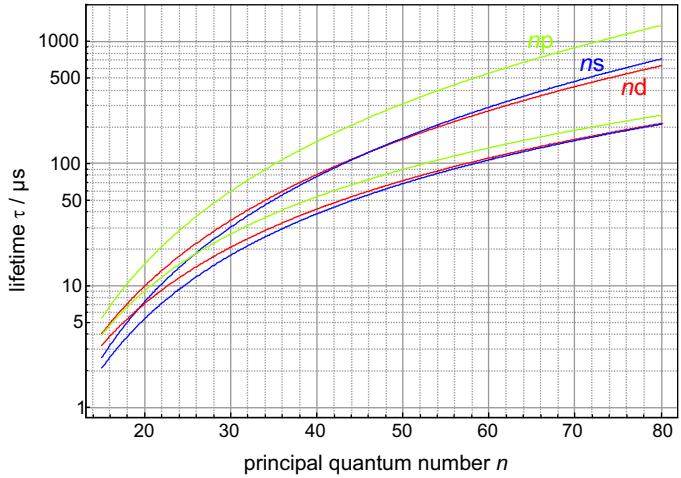

Fig. 2.5: Lifetimes of atomic Rydberg states. The upper curves show the radiative lifetimes $\tau_{rad}(nl)$ for $l = 0, 1, 2$ Rydberg states [25] and the lower ones the effective lifetimes τ_{eff} including blackbody induced transitions at T=300 K [31].

transition to the closest p state is enhanced by the number of photons in the thermal field by $N = 70$ for Rb($35s$) to $N = 1000$ for Rb($80s$) states (see Fig. 2.4).
Similar to eq. (2.17) the blackbody limited lifetime τ_{bb} can be written as sum over all possible transitions

$$\tau_{bb}(nl) = \left[\sum_{n'l'} \frac{A_{nl \to n'l'}}{\exp\{h\nu_{nl \to n'l'}/k_B T\} - 1} \right]^{-1} \tag{2.21}$$

and the effective lifetime is given by the sum of the depopulation rates due to spontaneous and stimulated decay

$$\tau_{\text{eff}}(nl) = \left[\frac{1}{\tau_{rad}(nl)} + \frac{1}{\tau_{bb}(nl)} \right]^{-1} . \tag{2.22}$$

As the photon number in a specific thermal mode is determined only by the temperature the problem of calculating the blackbody induced

lifetime is reduced to the calculation of the transition matrix elements of neighbouring Rydberg states $\langle n'l'|\, e\hat{r}\,|nl\rangle$. Beterov and coworkers determined the blackbody induced decay rates of rubidium [31] and compared them with the experimental data [25, 26, 27]. Their results for the effective lifetime τ_{eff} for s, p and d states as well as the radiative lifetimes τ_{rad} of ref. [25] are shown in Fig. 2.5.

2.1.3 Stark effect

The influence of a static electric field $\vec{F}$ upon atomic levels can be described by perturbation theory as long as the change in potential energy caused by the electric field is small compared to the atomic level separations $E_{nl} - E_{n'l'}$ [32]. The potential of an atom in an electric field is

$$V_{\text{Stark}} = -\hat{\mu}\vec{F}\,, \tag{2.23}$$

where $\hat{\mu}$ is the dipole moment of the atom. An electric field gradient $\nabla F \neq 0$ creates a force $-\nabla V_{\text{Stark}}$ upon the atom which can be used for decelerating and trapping of Rydberg atoms [33, 34, 35]. In the following, the electric field is considered to be static and homogeneous and $\vec{F}$ is replaced by $F = F_z$.

The Stark potential (2.23) can be expressed as expansion in F by perturbation theory

$$\hat{\mu} = \hat{\mu}_0 + \frac{1}{2}\,\alpha\, F + O(F^2)\,. \tag{2.24}$$

Here, $\hat{\mu}_0$ is the diagonal matrix element of the unperturbed Rydberg state $|nl\rangle$

$$\hat{\mu}_0 = \langle nl|e\hat{r}|nl\rangle \tag{2.25}$$

and α is the scalar polarizability

$$\alpha = 2 \sum_{\substack{n'l' \\ n'\neq n}} \frac{|\langle nl|e\hat{r}|n'l'\rangle|^2}{E_{nl} - E_{n'l'}}\,. \tag{2.26}$$

The dipole operator $\hat{\mu}$ connects only states of opposite parity and thus $\hat{\mu}_0 = 0$. An exception are degenerate states with different parity, e. g. the hydrogen-like states of the same principal quantum

number, n, but different angular momentum l. The matrix elements (2.25) of these states are not zero and therefore they show a linear Stark effect.
For non-degenerate states the first term of the expansion (2.24) vanishes and only the second order contributes to the energy in an electric field. Thus these states show a quadratic Stark effect. In a Rydberg atom this is the case for all states with a quantum defect $\delta_{nlj} \neq 0$; in rubidium the states with $l = 0, 1, 2, 3$ (see Chap. 2.1).
In contrast to the dipole moment which can be either positive or negative, the polarizability is a positive scalar and thus the second order Stark shift is always negative. Fig. 2.6 shows the n dependence of the polarizability of ^{85}Rb measured for ns states [36].

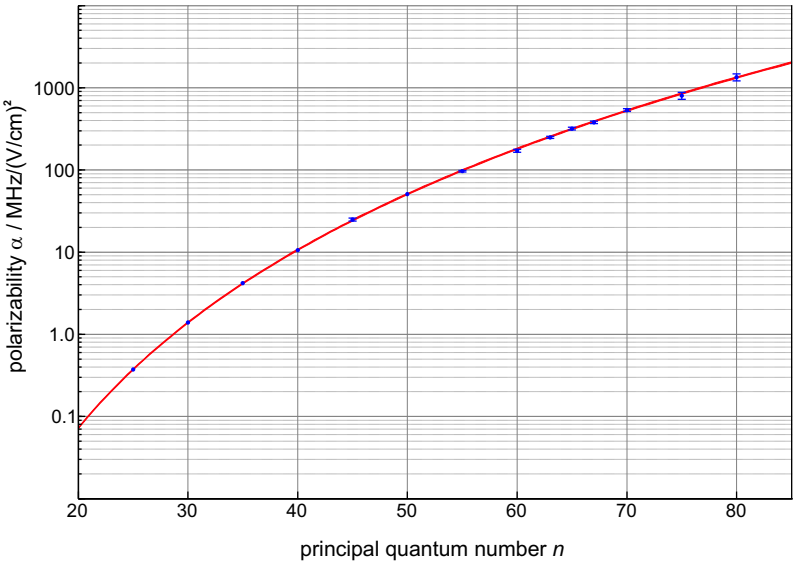

Fig. 2.6: Polarizabilities of the rubidium ns Rydberg states. O' Sullivan and coworkers [36] measured the polarizability of ^{85}Rb for ns Rydberg states, $15 \leq n \leq 80$, (blue) and interpolated the n-dependence (red).

2.1.4 Interacting Rydberg atoms

The huge electron orbits $r_n \propto a_0 n^2$ and the resulting large dipole moments and polarizabilities of Rydberg states (Tab. 2.2) lead to multipole forces between Rydberg atoms which are several orders of magnitude stronger than for ground state atoms. These interactions can be either repulsive or attractive depending on the angular momentum l of the Rydberg state and the relative orientation of the Rydberg atoms with respect to an external electric field.
The Rb(ns) Rydberg states show an isotropic and repulsive van der Waals interaction which leads to a blockade of the Rydberg excitation [37, 38, 39]. This blockade affects the Rydberg molecules in the same way as the Rydberg atoms and limits the number of excitations. Therefore the properties of the van der Waals blockade are summarized briefly.

The van der Waals interaction between two Rydberg atoms in the same ns state and with separation r reads

$$V_{vdW} = -\frac{C_6}{r^6}\,. \tag{2.27}$$

where the C_6 coefficient is a measure for the interaction strength and can be calculated by perturbation theory [40, 41]. Tab. 2.4 lists the C_6 coefficients for the Rydberg states addressed in this work. A consequence of the van der Waals interaction is a limitation of the Rydberg population. The minimum distance r_B between two Rydberg atoms is determined by the *blockade condition*

$$\hbar\Omega \geq -\frac{C_6}{r_B^6}\,, \tag{2.28}$$

i. e. the width of the driving laser $\hbar\Omega$ has to be larger or equal to the van der Waals interaction. For smaller distances $r < r_B$ the excitation laser is not resonant to the Rydberg state any more and thus the excitation of the second Rydberg atom is suppressed.

Tab. 2.4 gives also the blockade radii r_B for a laser linewidth of 1 MHz. As the van der Waals interaction depends on the sixth power of the radius, r_B changes only slightly with principal quantum number n. For all Rydberg states the blockade radius is much larger than

Ryd. states	34s-34s	35s-35s	36s-36s	37s-37s	40s-40s
$C_6/10^{18}$a.u.	-0.908	-1.310	-1.868	-2.636	-6.972
r_B/μm	2.254	2.396	2.542	2.692	3.166

Tab. 2.4: Van der Waals coefficients C_6 and blockade radii r_B for $ns - ns$ rubidium pairs. The C_6 coefficients are taken from [41]; the blockade radii r_B assume a laser linewidth of $h \cdot 1$MHz.

the mean particle separation in an ultracold cloud, $n_g^{-1/3}$, which is of the order of 400 nm. Thus a *blockade sphere* of volume $4/3\pi r_B^3$ contains a large number N of ground state atoms where each of them can be excited to the Rydberg state. This fact leads to a collective excitation of the Rydberg state [38, 42, 43] and an enhanced Rabi frequency

$$\Omega_c = \sqrt{N}\Omega_0 \,. \tag{2.29}$$

Here, Ω_0 is the single-atom Rabi frequency and N the number of atoms inside a blockade sphere. Depending on the density of ground state atoms n_g the enhancement ranges from $\sqrt{N} \approx 1$ for magneto-optically trapped atoms up to $\sqrt{N} \approx 30$ for a Bose-Einstein condensate [44, 45].

2.2 Electron–atom scattering

Scattering experiments are an important tool to gain insight in the structure of matter - from elementary particles to solids. Therefore scattering experiments with electrons, photons, neutrons or α-particles have a long tradition. In the early days of the last century, scientists started systematic studies and the probably most famous work are the experiments of Ernest Rutherford on the structure of the atom which were performed with α and β particles in 1911 [13]. Others investigated the scattering of electron beams by atomic gases and measured the scattering cross section of atomic species as function of electron velocity. Ramsauer discovered in 1923 that the cross section of some species like Ar, Kr and Xe strongly depends on the electron energy and vanishes for energies close to zero [46, 47]. A few years later, Amaldi and Segrè took absorption spectra of highly excited alkali metals in the presence of a foreign gas under pressure [1]. They found that, in contrast to their expectation, the atomic lines were shifted without broadening the lines excessively. Thus the spectra could not be explained simply by pressure broadening. Furthermore, even the sign of the observed line shifts seemed to depend on the foreign gas. In intense discussions with Fermi it turned out that these shifts were caused by the scattering of the valence electron of the alkali atoms – the Rydberg electrons – from the foreign gas atoms. Actually these early measurements were the first hint for the existence of the ultralong-range Rydberg molecules.
These and other experiments led to the development of theoretical models for describing scattering phenomena: Faxén and Holtsmark developed the *method of partial waves* to describe the electron–atom scattering quantum mechanically [4] and applied their theory to the results of Ramsauer. Their method can be used for all scattering processes which have a spherically symmetric scattering potential, like the $\propto 1/r^4$ potential for the electron–atom interaction, and will be discussed in the following paragraph 2.2.1.
Based on the experiments by Amaldi and Segrè, E. Fermi introduced his concept of *scattering length* for low-energy electron scattering which results in a surprisingly simple *pseudopotential*. Effectively, it describes the complex structure of the foreign atom by just one

scalar, the scattering length, and treats the interaction of the atom with the valence electron of the excited alkali as contact interaction. The following chapter introduces the concepts of partial waves (2.2.1) and scattering length and applies them to the ultralong-range Rydberg molecules. Their binding mechanism can be described by the continuous scattering of the ground state atom with the Rydberg electron which leads to bound states between the Rydberg and the ground state atom. As the kinetic energy of the electron is very low only the lowest partial waves contribute to the molecular potential and the electron-atom interaction can be described by a pseudopotential. The model for the potential of the ultralong-range Rydberg molecules and the calculation of their vibrational spectrum are discussed in the second part 2.2.2.

2.2.1 Partial waves

In a typical scattering experiment a beam of free particles, e. g. electrons, is scattered from a target. For a quantitative analysis the scattering process has to be described by quantum mechanics. The incoming and scattered particle are represented by a plane wave and a spherical wave, respectively, and the target by the scattering potential $V_{sc}(\vec{r})$.
For the electron–atom scattering this potential arises from the polarization of the atom in the Coulomb field $\vec{F}$ of the electron:

$$V_{sc}(\vec{r}) = -\frac{1}{2}\alpha\vec{F}^2(\vec{r})\,, \tag{2.30}$$

where α is the polarizability of the atom, here the rubidium 5s atom. The Coulomb field of an electron reads

$$\vec{F}(\vec{r}) = \frac{-e}{4\pi\epsilon_0}\cdot\frac{1}{|\vec{r}|^3}\,\vec{r}$$

and thus

$$V_{sc}(\vec{r}) = -\frac{e^2}{(4\pi\epsilon_0)^2}\cdot\frac{\alpha}{2\vec{r}^4}\,. \tag{2.31}$$

In analogy to the hydrogen atom the motion is described in the center of mass frame and thus relative coordinates $\vec{r}$ and an effective mass

μ are defined as:

$$\vec{r} = \vec{R}_{Rb} - \vec{R}_e, \qquad \mu = \frac{m_{Rb} \cdot m_e}{m_{Rb} + m_e}\,, \tag{2.32}$$

which reduces the two-body problem to the scattering of a single particle with mass μ from a fixed center of force $V_{sc}(\vec{r})$. In spherical coordinates (r, θ, ϕ) the time-independent Schrödinger equation then reads [32]

$$\frac{\hbar^2}{2\mu}\frac{1}{r^2}\frac{d}{dr}\left(r^2\frac{dR_{k\ell}}{dr}\right) + \left[\frac{\hbar^2 k^2}{2\mu} - \frac{\hbar^2\ell(\ell+1)}{2\mu r^2} - V_{sc}(r)\right] R_{k\ell} = 0\,. \tag{2.33}$$

The solutions have to be symmetric with respect to the z-axis, the propagation direction of the incoming particles. Each of them represents the motion of a particle with energy $\hbar^2k^2/2\mu$, angular momentum ℓ and vanishing projection upon the z-axis $m_\ell = 0$. The wavefunctions are thus of the form

$$\psi(r,\theta) \propto \sum_{\ell=0}^{\infty} P_\ell(\cos\theta) R_{k\ell}(r)\,. \tag{2.34}$$

P_ℓ are the associated Legendre polynomials. The asymptotic form of $R_{k\ell}$ is a spherical wave

$$R_{k\ell}(r) \approx \frac{2}{r}\sin\left(kr - \ell\frac{\pi}{2} + \delta_\ell\right)\,. \tag{2.35}$$

which has a phaseshift of δ_ℓ with respect to the incoming wave. It can be shown that the amplitude of the scattered wave $f(\theta)$ and the total scattering cross section σ_{tot} are [32]

$$f(\theta) = \sum_\ell (2\ell+1) f_\ell P_\ell(\cos\theta) \tag{2.36}$$

$$\sigma_{tot} = \frac{4\pi}{k^2}\sum_\ell (2\ell+1)\sin^2\delta_\ell\,. \tag{2.37}$$

The partial amplitudes and scattering cross sections are given by

$$f_\ell = \frac{1}{2ik}(e^{2i\delta_\ell} - 1) \tag{2.38}$$

$$\sigma_\ell = 4\pi(2\ell+1)\left|f_\ell\right|^2 = 4\pi(2\ell+1)\frac{\sin^2\delta_\ell}{k^2}\,. \tag{2.39}$$

In practice one has to ask which of the partial waves have to be considered for a specific scattering problem. This question is answered by the effective potential in the Schrödinger equation (2.33)

$$V_\ell^{\text{eff}}(r) = \frac{\hbar^2 \ell(\ell+1)}{2\mu r^2} + V_{sc}(r) \tag{2.40}$$

which is plotted for the polarization potential (2.30) of rubidium in Fig. 2.7. The potential for s-wave scattering ($\ell = 0$) is identical to the polarization potential (2.30) and always attractive. But for higher $\ell > 0$ a barrier occurs due to the first term in V_ℓ^{eff} which increases quadratically with ℓ. This barrier limits the partial waves that have to be considered in practice. If the energy of the incoming particles $\hbar^2 k^2/2\mu$ is too small to tunnel through the barrier of a certain ℓ the corresponding partial wave is suppressed and can be neglected. Thus in low energy scattering only the lowest partial waves contribute. In the simplest case, the process can be described by pure s-wave scattering.

2.2.2 Molecular potential curves

The interaction of a Rydberg atom and a ground state atom can be separated in three parts

$$H_{\text{mol}} = H_{\text{ion-e}^-} + H_{\text{atom-e}^-} + H_{\text{ion-atom}}\,, \tag{2.41}$$

where

$$H_{\text{ion-e}^-} = -\frac{\hbar^2}{2\mu}\left[\Delta - \frac{e}{4\pi\epsilon_0 R_e}\right], \tag{2.42}$$

$$H_{\text{atom-e}^-} = -\frac{\hbar^2}{2\mu}\left[\Delta - \frac{e^2}{(4\pi\epsilon_0)^2}\frac{\alpha_{\text{atom}}}{2r^4}\right], \tag{2.43}$$

$$H_{\text{ion-atom}} = -\frac{\hbar^2}{2\tilde{\mu}}\left[\Delta - \frac{e^2}{(4\pi\epsilon_0)^2}\frac{\alpha_{\text{atom}}}{2R_{Rb}^4}\right], \quad \tilde{\mu} = \frac{m_{Rb}}{2}\,. \tag{2.44}$$

The first term $H_{\text{ion-e}^-}$ describes the Rydberg atom whose eigenenergies and states are already known (see Chap. 2.1). The second term $H_{\text{atom-e}^-}$ includes the interaction between the ground state

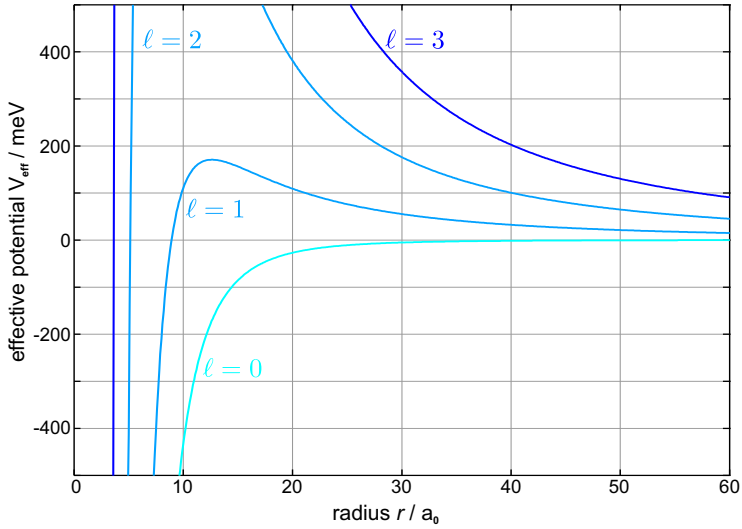

Fig. 2.7: Effective potentials $V_\ell^{\text{eff}}(r)$ for the electron-atom scattering of rubidium ($\alpha_{5s} = 319$ a.u.) for the first partial waves $\ell = 0 - 3$. For $\ell = 0$ the potential $V^{\text{eff}} = V_{sc}$; for $\ell \geq 1$ the potentials show a barrier of height 171 meV ($\ell = 1$), 1.54 eV ($\ell = 2$) and 6.14 eV for $\ell = 3$.

atom and the Rydberg electron. The Rydberg electron can be considered as quasi-free particle and the interaction with the ground state atom is treated as scattering problem which yields the molecular potential curves. The interaction between the ionic core of the Rydberg atom with the ground state atom is represented by the last term. This interaction is very weak for rubidium, as the polarization of the ground state atom Rb(5s) by the ionic core is less than 1 MHz for separations of $r \geq 1000\ a_0$. Thus for the start this term will be neglected; its influence on the molecular states will be discussed at the end of this chapter.

The separation of the Hamilton operator (2.41) is completely analog to the Born-Oppenheimer approximation in molecular physics where the Hamilton operator is divided in an electronic part and a vibrational/rotational part which takes the motion of the nuclei into account (Chap. 2.3). For the Rydberg molecules the term $H_{\text{ion-e}^-}$ thus

describes the electronic states and determines the dissociation limit of a certain molecular state. The vibrational and rotational spectrum of the molecules is determined by the electron-atom interaction which is the focus of this paragraph.

Scattering of low-energy electrons

For short-range potentials and low scattering energy k there exists the expansion[1]

$$-k^{-2\ell-1}\tan\delta_\ell = -A_\ell + \frac{1}{2}\,r_\ell^0 {A_\ell}^2 \cdot k^2 + O(k^4) \tag{2.45}$$

from effective-range theory (ERT) [48, 49] which connects the phase shift of a partial wave δ_ℓ with a scattering length A_ℓ and an effective range[2] r_ℓ^0. Here, potentials are of short-range if they fall off faster than any power of $1/r$. ERT is based on the fact that the Schrödinger equation (2.33) can be simplified for $r \leq r_\ell^0$ and $r > r_\ell^0$, respectively: In the first case the kinetic energy is much smaller than the scattering potential and can be neglected; in the second case the scattering potential is approximately zero and there remains the Schrödinger equation of a free particle. The solutions $R_{k\ell}$ are thus constructed from the solutions in the inner and outer part of the short-range potential [32]. Effective-range theory is widely used for low-energy nucleon-nucleon scattering but cannot be applied to atom scattering as the potentials there are of long-range. O'Malley and coworkers showed that there exists no energy-independent effective range r_ℓ^0 in the case of $1/r^4$ potentials [49], i. e. for electron-atom scattering. They developed a modified effective-range theory (MERT) for polarization potentials (2.30) which yields the following expansions in k for the s-wave ($\ell = 0$)

$$-\frac{\tan\delta_0}{k} \quad = \quad A_0 + \frac{\pi\alpha}{3}k + \frac{4\alpha A_0}{3}\ln\left(\frac{\sqrt{\alpha}k}{4}\right)\cdot k^2 + O(k^3) \tag{2.46}$$

and for higher partial waves $\ell \geq 1$

[1] Throughout the following paragraphs atomic units (a.u.) are used.

[2] Note that r_ℓ^0 depends not only on the range but also on the depth of the potential.

$$-\frac{\tan\delta_\ell}{k} = \frac{-\pi\alpha}{(2\ell+3)(2\ell+1)(2\ell-1)}\cdot k + O(k^2)\,. \tag{2.47}$$

These expressions are connected to the partial scattering cross sections σ_ℓ as for small energies k and thus small phase shifts δ_ℓ

$$\frac{\tan\delta_\ell}{k} \approx \frac{\sin\delta_\ell}{k} \tag{2.48}$$

$$(2.39) \quad \Rightarrow \quad \sigma_\ell \approx 4\pi(2\ell+1)\frac{\tan^2\delta_\ell}{k^2}\,.$$

Particularly for s-waves

$$\sigma_0 \approx 4\pi\left(A_0 + \frac{\pi\alpha}{3}\cdot k\right)^2$$

$$\lim_{k\to 0}\sigma_0 \approx 4\pi A_0^2\,. \tag{2.49}$$

In the limit of low energies $k \to 0$ the scattering is isotropic and the scattering cross section becomes independent of the electron energy. For finite energies k the expansions (2.46) and (2.47) can be regarded as energy-dependent scattering length $A_0\,[k]$ and $A_\ell\,[k]$, respectively.

Omont first applied the results from MERT to the scattering of a Rydberg electron and a ground state atom [5]. He expanded the Rydberg wavefunctions $\psi_{nlm}(r)$ in terms of plane waves by mean of a Fourier transformation. His result for the pseudopotential

$$V_{\text{pseudo}}(r) = 4\pi\sum_\ell (2\ell+1)A_\ell\,[k]\left\{P_\ell\left(\frac{\nabla'\cdot\nabla}{k^2}\right)\psi^*(r')\psi(r)\right\}_{r'=r} \tag{2.50}$$

uses the expressions of [49] for the energy-dependent scattering lengths. The energy of the Rydberg electron is given by the quasiclassical expression

$$k(r) = \sqrt{2E_{kin}} = \sqrt{2(E_{nl}+1/r)}\,. \tag{2.51}$$

The first term of the series (2.50)

$$V_{\ell=0}(r) = 2\pi A_0\,[k]\cdot|\psi_{nlm}(r)|^2 \tag{2.52}$$

is equivalent to the famous pseudopotential by Fermi for the s-wave scattering of a low-energy electron from an atom, but Fermi considered the scattering length as energy-independent: $A\,[k] = A_0$ [2].

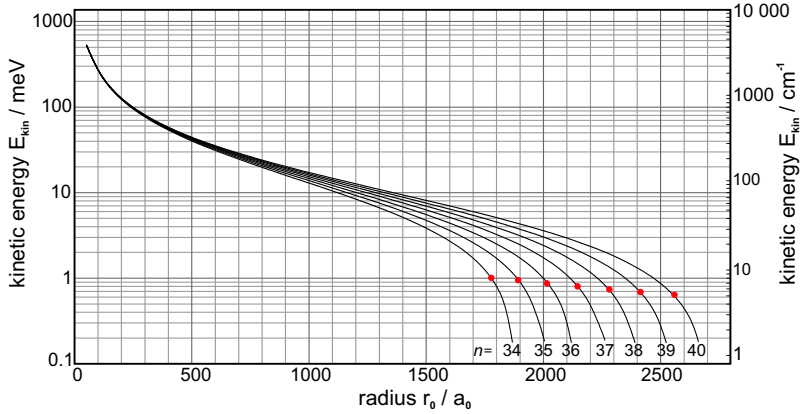

Fig. 2.8: Quasiclassical kinetic energy of the Rydberg electron for different Rb(ns) states. The position of the last lobe of the wavefunction $R_{ns}(r)$ is marked in red.

Details about Fermis approach can be found in Ref. [50]. The second term in (2.50) reads

$$V_{\ell=1}(r) = \frac{6\pi}{k^2} A_1\,[k]\,|\nabla\psi_{nlm}(r)|^2 \tag{2.53}$$

and describes the p-wave contribution to the scattering potential. But the aim of this paragraph was a simple description of the atom-electron scattering for low energies by replacing the interaction potential by a pseudopotential. This will be discussed in the following.

Potentials of ultralong-range Rydberg molecules

The question that has to be answered before applying the pseudopotential (2.50) to the electron-atom scattering for a specific Rydberg state is: How low are the kinetic energies of the Rydberg electron and which partial waves have to be considered? The quasiclassical expression for the kinetic energy of the Rydberg electron (2.51) is plotted in Fig. 2.8 for several Rb(ns) states. The energies at the position of the last lobe of the wavefunctions R_{ns} are all smaller or

equal to 1 meV for n between 34 and 40. For smaller radii r the kinetic energy increases and reaches $\approx$ 15 meV for $R = 1000\ a_0$. These energies are still small compared to the barrier heights of the effective potential (Fig. 2.7). Even for the p-wave ($\ell = 1$) the kinetic energies do not exceed 10% of the barrier height. Therefore the dominating term in the pseudopotential will be the s-wave scattering. P-wave contributions are not completely supressed but will be neglected for the first modelling of the molecular potential curves. Higher waves ($\ell \geq 2$) can safely be neglected.

Following the proposal by Greene [6] and assuming only s-wave scattering, the Hamilton operator for the electron-atom interaction in eq. (2.41) $H_{\text{atom-e}^-}$ is thus replaced by

$$\begin{aligned} V_{\ell=0}(n,l,r) &= 2\pi \cdot A\left[k(r)\right] \left|\psi_{nlm}(r)\right|^2 \\ \Rightarrow \qquad &= 2\pi \cdot A\left[k(r)\right] \frac{(2l+1)}{4\pi} \left|R_{nl}(r)\right|^2 , \end{aligned} \tag{2.54}$$

where the term $(2l + 1)/4\pi$ results from the normalization of the spherical harmonics. With $|Y_{00}|^2 = 1/4\pi$ for ns Rydberg states this yields

$$V_s(n,l,r) = \frac{1}{2} \cdot A\left[k(r)\right] \cdot \left|R_{nl}(r)\right|^2 . \tag{2.55}$$

The scattering length is given by

$$A\left[k(r)\right] = A_0 + \frac{\pi \alpha_{5s}}{3} k(r) + O(k^2) . \tag{2.56}$$

It depends on the ground state polarizability of rubidium which is measured with high accuracy to be $\alpha_{5s} = 319 \pm 6$ a.u. [51]. The scattering length A_0 depends on the relative spins of atom and electron. The ground state of rubidium has spin $s = 1/2$ and thus the multiplicity $(2S + 1)$ is either 1 or 3. Hence A_0 is labeled as singlet A_0^S and triplet scattering length A_0^T, respectively. Theoretical predictions for the zero-energy scattering length range from -16.9 a.u. [52] to -13 a.u. [53] for A_0^T and 0.627 a.u. [54] to 2.03 a.u. [52] for A_0^S. Thus only in the triplet case the potential (2.54) is attractive.

Fig. 2.9 shows the $r-$dependence of the factors $|R_{nl}(r)|^2$ and $a_T\,[k(r)]$ in (2.54) as well as the resulting potential for Rb(35s): The oscillatory character of the electron probability density is reflected in the molecular potential and the last lobe of the wavefunction at $r = 1900\ a_0$ creates the outermost and deepest potential minimum.
The depth of this minimum is determined by the zero-energy scattering length as the quasiclassical kinetic energy of the Rydberg electron becomes zero at the last lobe. $A^T\,[k(r)]$ is calculated for $A_0^T = -18.0\ a_0$ which gives the best agreement with the experimental results (Chap. 4.1.1) and is close to theoretical predictions [52, 53]. Thus the scattering length is negative for radii $r > 500\ a_0$; the zero-crossing occurs when the energy-dependent term reaches the value of $18.0\ a_0$ and for smaller radii, it gets positive and leads to a repulsive potential.
With that the molecular potential $V_s(35, 0, r)$ is repulsive for small radii and becomes attractive for $r > 500\ a_0$. The outermost minimum is -30.5 MHz deep and supports two bound states: the vibrational ground state $\nu = 0$ with a binding energy of -22.5 MHz and a Gaussian shaped wavefunction and a first excited state $\nu = 1$ with a binding energy of -10.1 MHz and a wavefunction of larger spread in r. The energy levels and wavefunctions of the molecular potential are computed using a numerical solver [55].

Now that the bond lengths of the molecules are known, the influence of the atom-ion interaction between the ionic core of the Rydberg atom and the ground state atom can be discussed. As already mentioned the polarizability of the ground state atom is very small: $\alpha_{5s} = 319 \pm 6$ a.u. $= 0.0794 \pm 0.0015$ Hz/(V/cm)^2 [51]. The energy shift due to the Coulomb field of the ionic core is therefore still small for distances equal to the bond length of the molecule. In Fig. 2.10 the polarization potential

$$V_{\text{ion}}(r) = -\frac{e^2}{(4\pi\epsilon_0)^2}\frac{\alpha_{5\text{s}}}{2r^4} \tag{2.57}$$

for rubidium is shown for radii $r = 200 - 4000\ a_0$, corresponding to the bond length of the vibrational ground states $\nu = 0$ in Rb(ns)-Rb(5s), $n = 15 - 50$. For all principal quantum numbers studied

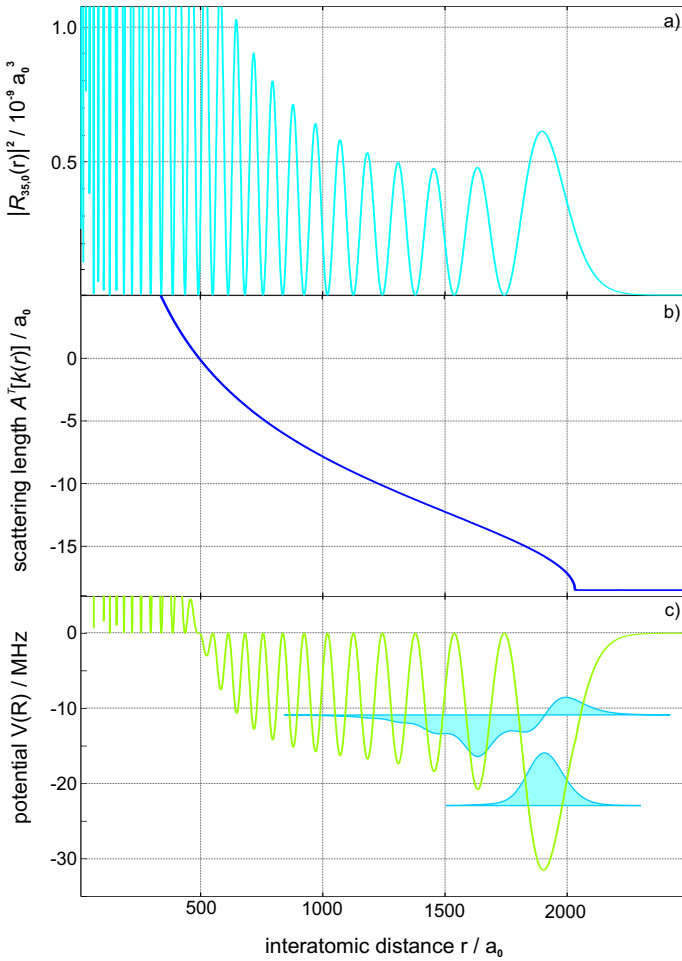

Fig. 2.9: Modelling of the molecular potential curve for the Rb(35s) state. a) Radial Rydberg electron probability density $|R_{35,0}(r)|^2$. b) Energy-dependent scattering length $A^T\,[k(r)]$ with A_0^T=-18 a_0. c) Molecular potential and vibrational states $\nu = 0$ and $\nu = 1$ with binding energies of -22.5 MHz and -10.1 MHz.

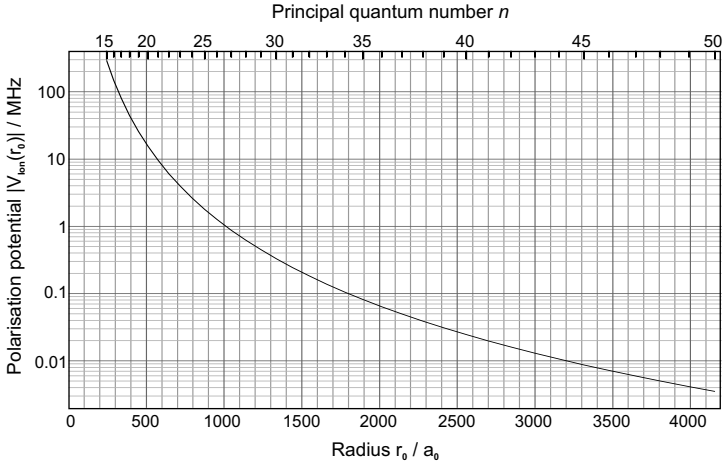

Fig. 2.10: Polarization potential (2.57) for Rb(5s). The energy shift of the molecular states due to the ionic rubidium nucleus Rb^+ is given in MHz. The bond lengths of the vibrational ground states Rb(ns)-Rb(5s)($\nu = 0$) are indicated on the upper axis.

here ($n = 34 - 40$), the shift for the molecular ground state $\nu = 0$ is well below $h \cdot 100$ kHz. For the excited states having a larger spread in r, the energy shift reaches $h \cdot 1$ MHz for $r = 1000\ a_0$ which is equal to the laser linewidth in the experiment. For these states the ionic core might at most cause a slight shift of the lines because the center of mass of the molecular wavefunction lies still at larger values of r where the influence of the ion is weaker. Therefore the ionic core would only affect those bound states significantly that are are confined at bond lengths of $r \approx 1000\ a_0$.

2.3 Diatomic molecules

The energetic structure of molecules is more complex than the one of atoms: First, a molecule has additional motional degrees of freedom connected to the vibration or rotation of the nuclei. Second, the energy levels of a molecule are no constants but functions of the interatomic distances. Their description is simplified by the fact that the mass of the electrons is much smaller than the mass of the nuclei. This allows to separate the motions of the nuclei - rotation and vibration - from the electronic structure [32, 56]. The electrons move so fast that they experience the nuclei as quasi-static and follow the motion of the nuclei adiabatically (Born-Oppenheimer approximation). In this chapter only the simplest molecule, the diatomic homonuclear molecule, is discussed. In this case the energies are a function of the internuclear distance R of the two atoms and there exists only one rotational degree of freedom, the end-over end rotation (Fig. 2.11a)). To avoid a mix-up of symbols for atomic and molecular states all molecular quantum numbers are named in capital letters.

The electronic states of an atom are classified by the angular momentum l. But a diatomic molecule has cylindrical symmetry: the electrostatic potential of the nuclei is only invariant under rotation around the molecular axis. The angular momentum L is therefore not a conserved quantity, but its projection on the molecular axis called Λ. For $\Lambda = 0, 1, 2, ...$ the electronic states are labeled as $\Sigma, \Pi, \Delta, ...$ The state is further characterized by the total spin S of all electrons which is given as multiplicity just like in the atomic notation: ${}^{2S+1}\Lambda$. Lastly the symmetry of the wavefunction with respect to reflection

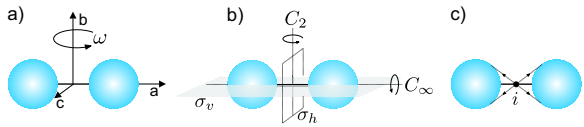

Fig. 2.11: Symmetries in a homonuclear diatomic molecule. a) Rotational axis of a diatomic molecule. b) ∞-fold and 2-fold symmetry axis and planes of symmetry σ_v and σ_h. c) Point of symmetry defining the parity.

at a plane or a point is used to classify a molecular state [57].
A diatomic molecule has one ∞-fold rotation axis (C_∞) along the molecular axis and a infinite number of 2-fold rotation axis (C_2) perpendicular to the molecular axis (Fig. 2.11b)). Due to the (C_∞) symmetry there are also infinite vertical reflection planes σ_v. Finally, homonuclear diatomic molecules have one horizontal reflection plane σ_h and an inversion center i, the center of mass of the molecule (Fig. 2.11c)). These two symmetry operations only occur combined. While the σ_h symmetry is used to label the symmetry group (here $D_{\infty h} = C_\infty + \text{perpendicular } C_2 + \sigma_h$), the inversion symmetry gives the parity of a specific molecular state and is thus characteristic for the molecular wavefunction. The parity of the wavefunction is given as subscript to the electronic state: "g" for symmetric or "u" for antisymmetric.
The reflection T at the plane σ_v does not change the energy of the molecule but the sign of the angular momentum L. Thus all energy levels with non-zero angular momentum have a degeneracy of two. In the case of Σ states there is no degeneracy but the wavefunction can still change its sign: $\psi \xrightarrow{T} (\pm 1) \cdot \psi \xrightarrow{T} \psi$. This property is indicated by the superscript $\pm$.
In total the state of a diatomic molecule is labeled as: ${}^{2S+1}\Lambda^{+/-}_{g/u}$. The electronic ground state of a homonuclear molecule has an even parity and aside from a few exceptions, like e. g. O_2, it is a singlet (S=0) and symmetric under reflection at σ_v.

2.3.1 Vibration and Rotation

In general, the Hamilton operator H of a molecule can be simplified by a separation of the motion of the electrons (e) and the nuclei (n). The motion of the nuclei can furthermore be divided in a vibrational and a rotational part as they take place on different time scales. Interactions between electronic, vibrational and rotational states can be treated subsequently as perturbation. The complete Hamilton operator then reads

$$H = T_n + T_e + V_{nn} + V_{ne} + V_{ee} \tag{2.58}$$

$$= -\frac{1}{2m_n}\sum_n p_n^2 - \frac{1}{2m_e}\sum_e p_e^2 + V_{nn} + V_{ne} + V_{ee}\,,$$

where T and V are the kinetic and potential energies, respectively.

The separation of the wavefunction $\Psi = \xi_{el}\phi_{rot}\varphi_{vib}$ yields

$$H = H_{el} + H_{vib} + H_{rot}\ , \tag{2.59}$$

This ansatz includes the following approximations:

- Decoupling of the motions of the electrons and nuclei (Born-Oppenheimer approximation). The coordinates of the nuclei appear in the electronic wavefunctions ξ_{el} only as parameter and no longer as time-dependent variables.

- Separation of vibration and rotation. In the Hamilton operator of the rotation H_{rot} the instantaneous distances of the nuclei are replaced by the equilibrium distances, i. e. a rigid rotor with fixed bond length is assumed.

For the molecules studied in this work the electronic term H_{el} is represented by the Hamiltonian of the Rydberg atom $H_{\text{ion-e}^-}$ in eq. (2.41) with the solutions $Y_{lm}R_{nl}$ already described in Chap. 2.1. The molecular potential $V_s(n,l,r)$ in eq. (2.55) which arises from the low-energy scattering of the Rydberg electron with a ground state atom determines the vibrational and rotational states of the molecule. This model treats the electron–atom interaction by perturbation theory and thus assumes the Rydberg wavefunction to be not affected by the presence of the ground state atom. This assumption is equivalent to the Born-Oppenheimer approximation (2.59).
The following comparison of the level spacings between adjacent vibrational and rotational states will show that also the separation of vibration and rotation is a good assumption.

Vibration

The vibrational states φ_{vib} are the stationary solutions of the Hamilton operator

$$H_{vib} = -\frac{\hbar^2}{2\mu}\frac{d^2}{dr^2} + V_{vib}(r)\,, \tag{2.60}$$

where μ is the effective mass of the nuclei. For a diatomic molecule, there exists only one vibrational mode, the stretch mode along the molecular bond. Classically, the solutions of (2.60) can be connected with the oscillatory motion of the atomic nuclei, where the interatomic distance r changes as function of time. The turning points of the oscillation are determined by the spread in r of the vibrational wavefunctions φ_{vib}.
Although they are very different in depth, equilibrium distance and width, many molecular potentials $V_{vib}(r)$ can be approximated by potentials with analytic solutions, e. g. a harmonic, Morse or a quartic potential [56]. Now, the s-wave potential of the ultralong-range Rydberg molecules (2.55) will be compared to two of them briefly. The Morse potential reads

$$V_{\mathrm{Morse}}(r) = V_D\left(1 - e^{-\frac{(r-r_e)}{\sigma}}\right)^2 \tag{2.61}$$

and allows for an exact solution of the eigenstates of H_{vib} in (2.60). It is an asymmetric potential with a minimum at $r = r_e$. The parameter σ determines the width of the potential. For large radii $r \to \infty$ it gets flat and finally reaches the dissociation limit V_D where the atoms are no longer bound. For radii $r < r_e, r \to 0$, the potential increases steeply and becomes repulsive modelling the exchange interaction of the electrons. For small vibrational amplitudes, i. e. low vibrational quantum numbers ν, the potential can also be approximated by a harmonic potential

$$V_{\mathrm{harm}}(r) = \frac{\mu\omega^2}{2}r^2 \tag{2.62}$$

with the eigenenergies

$$E_\nu = \hbar\omega\left(\nu + \frac{1}{2}\right)\,. \tag{2.63}$$

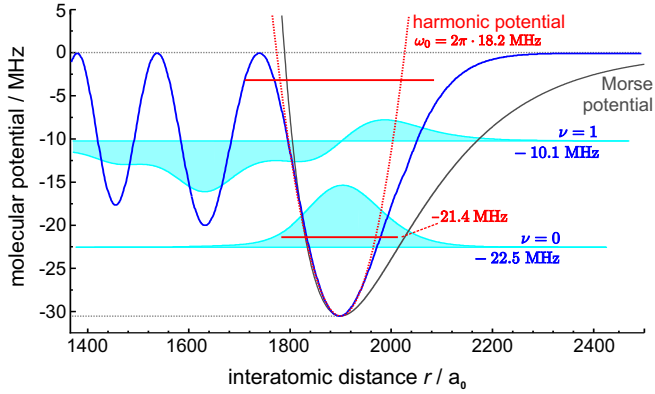

Fig. 2.12: Comparison of the pure s-wave potential $^3\Sigma(35s - 5s)$ (blue) to a harmonic (red) and a Morse potential (gray). Also shown are the solutions of the s-wave potential and the harmonic potential.

Fig. 2.12 shows the molecular potential of the electronic state $^3\Sigma(35s-5s)$ calculated from s-wave scattering (Chap. 2.2.2) as well as a harmonic potential and a Morse potential fitted to the s-wave potential. The agreement between the s-wave potential and the harmonic one is even better than for the Morse potential and the solutions for the eigenenergy of the ground state $\nu = 0$ are quite close. Thus for a first estimate of the ground state binding energy the harmonic approximation is an alternative to a numerical solver.

Rotation

In general, the Hamilton operator for the rotation of a molecule H_{rot} reads

$$H_{rot} = A\hat{J}_a^2 + B\hat{J}_b^2 + C\hat{J}_c^2 \quad , \tag{2.64}$$

where $\hat{J}_a, \hat{J}_b, \hat{J}_c$ are the projections of the angular momentum $\hat{J}$ on the principal axis of the molecule $(\vec{a}, \vec{b}, \vec{c})$ (see Fig. 2.11a) and

$$A = \frac{1}{2I_a} \qquad B = \frac{1}{2I_b} \qquad C = \frac{1}{2I_c} \tag{2.65}$$

are the rotational constants which are defined by the principal moments of inertia I_a, I_b and I_c. For a diatomic molecule $I_a = 0$, $I_b = I_c$ and eq. (2.64) simplifies to

$$H_{rot} = B\hat{J}^2 \quad . \tag{2.66}$$

The rotational constant B is determined by the equilibrium distance r_e of the nuclei and their effective mass μ:

$$B = \frac{1}{2I_b} = \frac{1}{2\mu r_e^2} \, . \tag{2.67}$$

For the rubidium molecule Rb_2 the effective mass is $\mu = 1/2m_{Rb} = 43.5$ amu. The ultralong-range Rydberg molecules studied here have bond lengths of 1800 a_0 (Rb(34s)-Rb(5s)) to 2550 a_0 (Rb(40s)-Rb(5s)) and thus rotational constants ranging from $B_{40s-5s} = 6.3$ kHz to $B_{34s-5s} = 13.2$ kHz which are more than two orders of magnitude smaller than the vibrational level spacings.

For linear molecules having only one molecular axis the rotation is characterized by the angular momentum of the rotation $\hat{J}^2$, where in general

$$\hat{J}^2|\phi_{rot}\rangle = \hbar^2 J(J+1)|\phi_{rot}\rangle \, , \quad J = 0, 1, 2, ... \tag{2.68}$$

$$\hat{J}_b|\phi_{rot}\rangle = \hbar K|\phi_{rot}\rangle \, , \qquad K = -J, ..., J \, . \tag{2.69}$$

But as the rotational axis is perpendicular to the molecular axis $\vec{b}$ the projection $K = 0$ (see Fig. 2.11). In the presence of an external field (in z direction), e. g. an electric field, the quantum number M describes the orientation of the rotational axis with respect to this field:

$$\hat{J}_z|\phi_{rot}\rangle = \hbar M|\phi_{rot}\rangle \, , \quad M = -J, ..., J \, . \tag{2.70}$$

The eigenfunctions ϕ_{rot} of $\hat{J}$ and $\hat{J}^2$ are the Legendre polynoms. The corresponding eigenvalues of the Hamilton operator (2.66) thus read:

$$E_{rot} = \hbar^2 BJ(J+1) \quad . \tag{2.71}$$

The rotational energy E_{rot} increases quadratically with angular momentum J. The distribution of the molecules over the different rotational states $E_{rot}(J)$ in a thermal sample is discussed in Chap. 2.3.3.

2.3.2 Stark effect

Similar to the atomic case (Chap. 2.1.3) the Stark effect of a molecule can be treated by perturbation theory if the level separation of the electronic states is large compared to the energy shift caused by the electric field. For the ultralong-range molecules studied here the electronic states and the dissociation limits are represented by the atomic Rydberg states. Thus the limits of validity for a perturbative approach are the same as for the atomic Rydberg states. As the dissociation limit is determined by the atomic Rydberg level, even the Stark shift of the molecules is approximately equal to the atomic shift ΔE_{Stark}^{atom}.
A complication of the molecular Stark pattern arises from their rotational structure. Each rotational level $E_{rot}(J)$ (2.71) consists of $2J+1$ components which are degenerate in zero field. But in the presence of an electric field, this degeneracy is lifted and the lines split up in their M components. Therefore, the total Stark shift of a molecular state $|JKM\rangle$ has two contributions: the shift of the atomic Rydberg state and the splitting of the rotational states

$$\Delta E_{Stark}^{mol} = \Delta E_{Stark}^{atom} + \Delta E_{Stark}^{rot}\,, \tag{2.72}$$

which yields for ns Rydberg states

$$= -\frac{1}{2}\,\alpha_{ns}\cdot F^2 + \Delta E_{Stark}^{rot}\,. \tag{2.73}$$

This paragraph summarizes the results of first- and second-order Stark effect for symmetric molecules. For a derivation of the equations the reader is referred to Ref. [58, 59, 60, 50].

The first-order energy shift of a molecular state in an electric field F is

$$\Delta E_{Stark}^{(1)} = -\mu_p F\cdot\frac{MK}{J(J+1)}\,, \tag{2.74}$$

where K and M are the projections of the total angular momentum J on the molecular and electric field axis, respectively. μ_p is the permanent dipole moment of the molecule. For linear molecules $\hat{J}\perp\vec{a}$, i. e. $K=0$ and thus the first-order correction vanishes. From a classical point of view this means the time-average of the dipole moment,

pointing along the molecular axis $\vec{a}$ in a linear molecule, is zero as there exists only one rotational degree of freedom, the end-over-end rotation perpendicular to $\vec{a}$.
The second-order perturbation is composed of two terms: the first term arises from the permanent dipole μ_p and the second from the induced dipoles, quantified by the components of the polarizability tensor α_{aa}, α_{bb} and α_{cc}:

$$\begin{aligned}\Delta E^{(2)}_{Stark} &= \frac{\mu_p^2 F^2}{2\underbrace{\hbar^2 B J(J+1)}_{E_{rot}}} \cdot \frac{J(J+1)-3M^2}{(2J-1)(2J+3)} \\ &\quad - \frac{1}{2}F^2 \sum_{i=a,b,c} \alpha_{ii}\left[A_{JK}(i) + B_{JK}(i)M^2\right] . \quad (2.75)\end{aligned}$$

The coefficients A_{JK} and B_{JK} depend on the molecular symmetry and have to be calculated from the matrix elements of the direction cosine [58, 60, 50]. For a linear molecule there are only two independent components of the polarizability: The component along the molecular axis α_{aa} and the components $\alpha_{bb} = \alpha_{cc}$ of the axis perpendicular to the molecular axis (see Fig. 2.11a). Furthermore, homonuclear molecules have no permanent dipole moment $\mu_p = 0$ and also the first term in $\Delta E^{(2)}_{Stark}$ vanishes. Thus the Stark shift of a homonuclear diatomic molecule finally reads

$$\Delta E^{(2)}_{Stark} = -\frac{1}{2}\alpha_{bb}F^2 - \frac{1}{2}(\alpha_{aa}-\alpha_{bb})(A_{JK} + B_{JK}M^2)F^2 , \quad (2.76)$$

where

$$\begin{aligned}A_{JK} &= \frac{J^2-K^2}{4J^2-1} + \frac{(J+1)^2-K^2}{(2J+1)(2J+3)} \\ B_{JK} &= \frac{K^2-J^2}{J^2(4J^2-1)} + \frac{K^2}{J^2(J+1)^2} + \frac{K^2-(J+1)^2}{(J+1)^2(2J+1)(2J+3)} ,\end{aligned}$$

and which simplify for $K = 0$ to

$$\begin{aligned}A_{J0} &= \frac{J^2}{4J^2-1} + \frac{(J+1)^2}{(2J+1)(2J+3)} \\ B_{J0} &= -\frac{1}{(4J^2-1)} - \frac{1}{(2J+1)(2J+3)} . \quad (2.77)\end{aligned}$$

For the ultralong-range Rydberg molecules studied here, the polarizability α_{bb} will be very close to the atomic Rydberg state: $\alpha_{bb} \cong \alpha_{ns}$ (see eq. (2.73)). Under the assumption that the presence of the ground state atom does not perturb the Rydberg wavefunction, the relation $\alpha_{bb} = \alpha_{aa} = \alpha_{ns}$ holds and the molecular Stark shift is equal to the Stark shift of the Rydberg state. In contrast, any back effect of the ground state atom on the Rydberg wavefunction will lead to an anisotropy $\delta\alpha := \alpha_{aa} - \alpha_{bb}$ and cause a splitting of the rotational states $|JKM\rangle$ in their M components which is described by the second term in (2.76). But a back effect of the ground state atom would probably already change the Rydberg wavefunction in zero electric field and increase the probability density of the Rydberg electron at the position of the ground state atom. In this case the Rydberg molecules would have a small dipole moment μ_p and also the first term in (2.75) would contribute to the second-order Stark shift $\Delta E^{(2)}_{Stark}$.

2.3.3 Photoassociation

When a gas of atoms is illuminated with a laser of the right frequency, two atoms can be photoassociated to a molecule. This free–bound process is a resonant transition and the photon energy of the laser $h\nu$ has to match the separation of the energy levels of the initial pair state and the bound state (Fig. 2.13). For chemically bound molecules, photoassociation (PA) creates molecules in a highly excited vibrational state [61]: The internuclear separation r of the atoms does not change during the absorption and excitation to the bound state. Therefore, photoassociation can only address vibrational states which have a non-vanishing probability density for the separation, r, of the free atoms in the gas (Franck-Condon principle). The typical bond length of a vibrational ground state is on the same order of magnitude as the bond length in a solid ($\propto 10\ a_0$) and much smaller than the separations in any gas, even in a BEC. Thus the vibrational ground state of any chemically bound molecule is not accessible directly via PA.
The ultralong-range molecules studied here belong to the *purely long-range molecules*, i.e. both inner and outer turning point of the vibra-

tional motion lie at large internuclear separation. In contrast to the chemically bound ones, their vibrational ground state requires only atomic separations of $r \approx 2000a_0$ which can be obtained in ultracold and dense gases.
One big advantage of photoassociation spectroscopy is the ability to measure absolute binding energies. Each vibrational state appears red-detuned from the atomic resonance, i. e. the dissociation limit, and by scanning the laser from the atomic resonance to the red, the molecular states are addressed one after another, starting from the highest excited state down to the ground state $\nu = 0$. Accordingly, the binding energies are obtained directly from the spectrum as separations of the vibrational lines from the atomic resonance. The PA scheme of the Rydberg molecule $^3\Sigma(35s - 5s)$ is illustrated in Fig. 2.13. Special about this type of molecule are the shallow potential and the small spacings of the vibrational states of only several Mega-Hertz.

The resolution in PA spectroscopy is influenced by several factors: the spread in thermal energy of the atomic sample, the Doppler broadening of the PA transition or the laser linewidth [61]. For the transition $5s_{1/2} \rightarrow 35s_{1/2}$ in rubidium, the Doppler broadening is $\Delta\nu_D = 145$ kHz (FWHM) at a temperature of $T = 3.5$ μK. In the current experiment, the thermal energy is $k_B \cdot 3.5$ $\mu\text{K} \approx h \cdot 73$ kHz and thus very small. But aside from the width of the ground state $5s$–$5s$ the thermal energy k_BT is also a measure for the relative velocities of the atoms. In the moment of photoassociation, this velocity is transferred to the rotational angular momentum of the molecule, J. Thus the thermal energy determines also the population of the rotational states. For a thermal distribution the population factor f_{rot} of the rotational state J reads [58]

$$f_{rot}(J) \quad \propto \quad (2J+1) \cdot \exp\left[-\frac{E_{rot}}{k_BT}\right]$$

and with eq. (2.71)

$$\Rightarrow \quad \propto \quad (2J+1) \cdot \exp\left[-\frac{\hbar^2 BJ(J+1)}{k_BT}\right]. \qquad (2.78)$$

The factor $(2J + 1)$ arises because of the M spatial degeneracy of the orientation of J. Fig. 2.13 shows the rotational levels and their

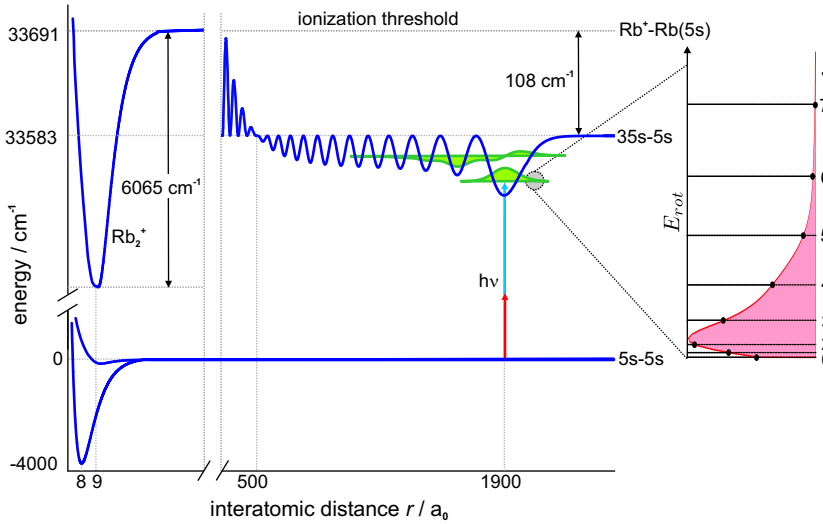

Fig. 2.13: Molecular potential curves of the electronic ground states of Rb_2 and Rb_2^+ [62] and of the ultralong-range molecule $^3\Sigma(35s-5s)$. The inset illustrates the population of the rotational levels $E_{rot}(J)$ at a temperature of $T = 3.5$ μK.

population f_{rot} for $T = 3.5$ μK, a typical temperature in the experiment. Only the lowest rotational states up to $J = 6$ are populated; the maximum of the distribution is close to the $J = 2$ state. For all rotational states the separation to the neighbouring state is smaller than the Doppler width $\Delta\nu_D/2$ and cannot be resolved as single lines in the PA spectrum. Assuming a Doppler width of 145 kHz for each of these rotational levels and a population given by (2.78) results in an asymmetric line of width $\Delta\nu \cong 200$ kHz (FWHM). This value is still below the laser linewidth of 1 MHz of the current experiment (Chap. 3.2.1).

3. Experimental methods

All experiments presented in this thesis are performed in an ultracold sample of trapped rubidium atoms and in basically the same experimental sequence (Fig. 3.1):
After cooling and trapping, a short laser pulse is applied and the ground state atoms are partly excited to the ns Rydberg state in a two-photon process. Subsequently, the Rydberg atoms are field ionized and the created ions accelerated towards a microchannel plate detector (MCP). Finally, absorption imaging is used to measure density and temperature of the remaining sample of ground state atoms.

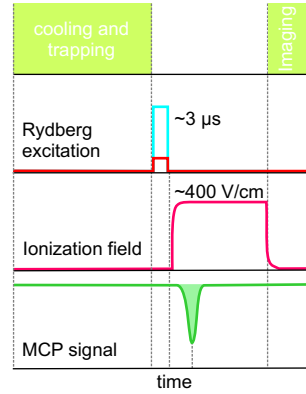

Fig. 3.1: Sequence.

Therefore, the experimental sequence as well as the setup can be divided in two parts: the preparation of a dense sample of ^{87}Rb and the Rydberg excitation and detection. The setup for preparing cold atoms is already well documented in the theses of U. Raitzsch [63] and R. Löw [64] and thus this part of the experimental procedure is only summarized briefly in Chap. 3.1. Instead, the focus of this chapter is on the Rydberg excitation and detection: In Chap. 3.2 the level scheme of ^{87}Rb and the excitation path to the Rydberg states are discussed, followed by the description of the laser system (3.2.1) and the ionization and detection of Rydberg atoms (3.2.2).

3.1 Ultracold ^{87}Rb samples

The photoassociation of the ultralong range Rydberg molecules requires on the one hand dense samples of ground state atoms as the pairs that can be bound to a molecule must have distances of only 94 nm (Rb(5s)-Rb(34s)) to 135 nm (Rb(5s)-Rb(40s)) and on the other hand large samples as the blockade due to the van der Waals interaction limits the number of Rydberg molecules per volume in the same way as the number of Rydberg atoms (Chap. 2.1.4).
To fulfill both of these requirements and to ensure a sufficiently large number of molecules for detection, the experiments are performed in a very cold and thus dense sample, but still above the critical temperature T_c where Bose-Einstein condensation occurs. Working in a BEC would have the advantage of a triply higher density, but also

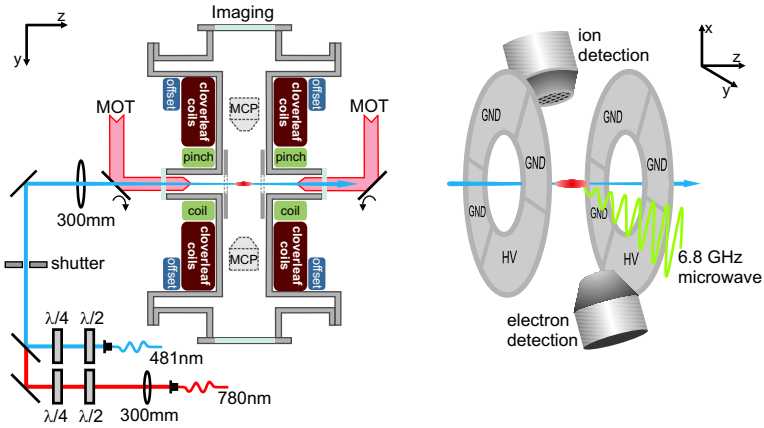

Fig. 3.2: Experimental setup. Left: Topview on the vacuum chamber with parts of the optics for magneto-optical trapping (MOT) and Rydberg excitation. The cigar shaped cloud of ground state atoms is trapped in the center of the chamber by the magnetic field of the cloverleaf, pinch, and offset coils. The atomic sample is illuminated by the two Rydberg lasers (780 nm and 481 nm) along its long axis. Right: 3D view on the electric field plates and the microchannel plates for electron and ion detection mounted inside the vacuum.

the volume of the atomic cloud would shrink by a factor of more than 500 when crossing T_c, leading to populations of Rydberg atoms and molecules that are limited by the van der Waals blockade [44].

The experimental sequence of cooling and trapping starts with loading a magneto-optical trap from an effusive beam precooled in a Zeeman slower: ^{87}Rb is heated to 160° C in an oven and enters the Zeeman slower through a differential pumping. As first cooling step, the resulting effusive beam is Doppler-cooled by a counterpropagating laser beam. The increasing magnetic field of the Zeeman slower compensates the decreasing Doppler shift due to the cooling and keeps the atoms resonant to the cooling laser. At the end of the Zeeman slower, the atoms are cold enough to be trapped magneto-optically in the center of the vacuum chamber (Fig. 3.2). Three pairs of counterpropagating beams - one pair shown in Fig. 3.2 - and a magnetic quadrupole field constitute the magneto-optical trap (MOT), which is loaded continuously by the Zeeman slower for several seconds. Both cooling processes, the Zeeman cooling as well as the cooling in the MOT work on the transition $5s_{1/2}, f = 2, m_f = 2 \rightarrow 5p_{3/2}, f = 3, m_f = 3$. Before loading the atoms to the magnetic trap a short molasses cooling and a compression of the sample is applied to further reduce the temperature below the Doppler limit. As last step, the cloud is cooled evaporatively in the magnetic trap produced by copper coils in a cloverleaf configuration. In this process a radio-frequency field is switched on and transfers atoms from the trapped state $5s_{1/2}, f = 2, m_f = 2$ by $\Delta m = -1$ transitions successively to the untrapped state $5s_{1/2}, f = 2, m_f = -2$. Initially, the rf-frequency is high (45 MHz) and only hot atoms which reach the outer part of the magnetic trap become resonant to the rf-field. Therefore the hottest atoms are removed from the trap and after thermalization, the temperature of the sample is slightly decreased. By ramping down the

atom number	$4.0 \cdot 10^6$	$1/e-$radius σ_r	10.7 μm
peak density	$1.6 \cdot 10^{13} \frac{\text{atoms}}{\text{cm}^3}$	$1/e-$radius σ_z	135 μm

Tab. 3.1: Parameters of an atomic sample at T=3.5 μK.

rf-frequency slowly this cooling process is continued until only ultracold atoms remain in the trap. Typical values for the atom number, peak density and sizes of the samples are given in Tab. **??**.
These values are measured at the end of each sequence by absorption imaging after a certain time of flight. The magnetic trapping potential is switched off and after a free expansion of typically 20 ms duration the atoms are imaged on a CCD-camera by resonant laser light. By comparing the intensity transmitted through the cloud to a dark picture and a picture of the imaging laser without any atoms the optical density can be determined from the resulting 2D-Gaussian distribution. Details on the evaluation of absorption images are given in [44].

3.1.1 Magnetic fields

For trapping the atoms in a low-field seeking state, the cloverleaf coils create a magnetic quadrupole field, increasing linearly from the center of the trap. As a quadrupole field has always a zero-crossing which would allow the atoms to leave the trap by Majorana spin-flip transitions, an additional offset field B_0 has to be added by the offset coils. The resulting field geometry is parabolic in the center of the trap and changes to a linear field in the outer part.
The magnetic field of the trap leads to a Zeeman shift of the atomic levels in the ground state as well as in the Rydberg states. Although the experiments are done at ultralow temperatures of a few micro-Kelvin, which means all atoms are located in the center of the trap and exposed only to the offset field $B_0 < 1$ G, the Zeeman shift of the ground state $5s_{1/2}, f = 2, m_f = 2$ and the Rydberg state $ns_{1/2}, s = 1/2, m_s = 1/2$ is in both cases 1.4 MHz/Gauss. As a consequence, also the molecular Rydberg states are Zeeman shifted. But the relative line positions of the free and bound Rydberg states, and thus the measurement of the binding energy of the molecules, are not affected by the magnetic field [50].
The magnetic offset field B_0 can be measured by using microwave radiation which is tunable around the transition frequency of the hyperfine states $5s_{1/2}, f = 1 \rightarrow f = 2$ of 6.8 GHz (Fig. 3.3, [65]). By applying resonant microwave radiation to an atomic sam-

ple trapped in the $5s_{1/2}, f = 2, m_f = 2$ state the atoms can be transferred to the state $f = 1$ which is not trapped magnetically. Thus the transition frequency of the Zeeman shifted hyperfine levels $5s_{1/2}, f = 2, m_f = 2 \rightarrow 5s_{1/2}, f = 1, m_f = 1$ in the magnetic field ν_B can be determined by measuring the losses from the trap versus microwave frequency. The magnetic field is given by the deviation of the transition frequency ν_B from the one in zero-field $\nu_0 = 6.834\,683$ GHz [66]

$$B_0 = \frac{2h(\nu_B - \nu_0)}{\mu_B}\,. \tag{3.1}$$

3.2 Rydberg excitation

The ionization energy of the rubidium ground state is $33\,690.8$ cm^{-1} [14], corresponding to a wavelength for excitation of 297 nm. As this wavelength is only achievable by frequency-doubling of a dye laser with a rather small power in continuous wave mode, the Rydberg states are instead addressed in a two-photon excitation (Fig. 3.3). This has several advantages:

- Both wavelengths of 780 nm and 481 nm are available as diode laser systems needing less maintenance than a dye laser and supplying effectively more power than a single-photon excitation.

- In a two-photon excitation it is possible to address ns and nd states instead of only np states. Their Rydberg-Rydberg interactions are of different types: While the Rydberg-Rydberg interaction between ns states has always a repulsive and isotropic van der Waals character, nd states exhibit dipole-dipole interactions which are anisotropic and can either be repulsive or attractive.

- The dipole matrix element of the lower transition $5s_{1/2} \rightarrow 5p_{3/2}$ is very strong. Thus the detuning and the power of the 780 nm laser is a sensitive tool for tuning the effective Rabi frequency.

- The two-photon excitation allows for pump-probe experiments like Autler-Townes spectroscopy [67, 68] and electromagnetically induced transparency [69].

In the context of this research it was important to choose states having molecular bound states within reach of the atomic transition and being therefore observable in a spectrum together with the atomic line in high resolution. Furthermore addressing states with a repul-

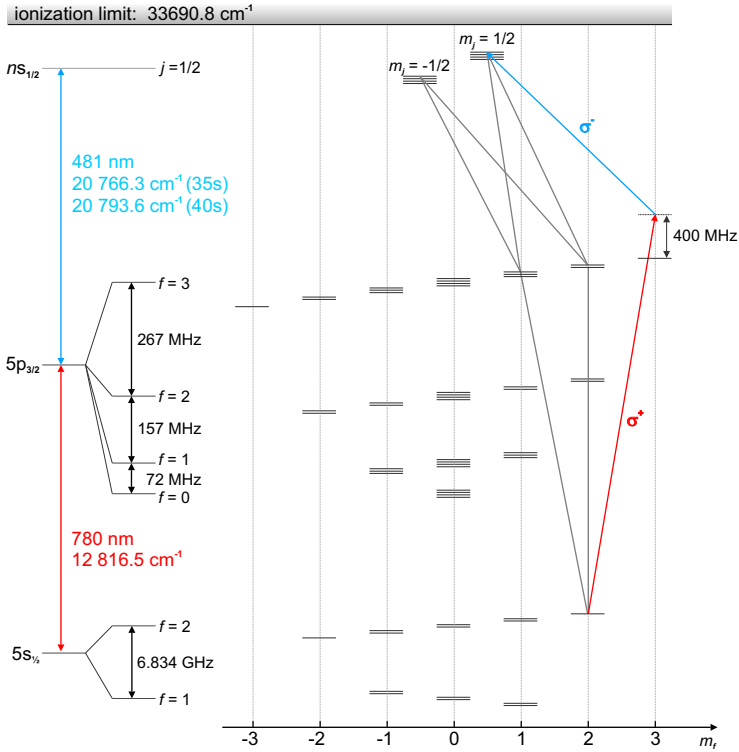

Fig. 3.3: Level scheme of the isotope ^{87}Rb (nuclear spin $i = 3/2$): ground state $5s_{1/2}$, the first excited state $5p_{3/2}$ and the addressed Rydberg level $ns_{1/2}$. The values for the ground and first excited state are taken from [70].

sive Rydberg-Rydberg interaction is favourable for avoiding losses due to collisions. For these reasons the experiments are performed with ns Rydberg states with principal quantum numbers n between 34 and 40.

The essential parts of the rubidium level scheme and the excitation path are depicted in Fig. 3.3. The ground state atoms trapped in the $f = 2$, $m_f = 2$ are excited to the $ns_{1/2}$ Rydberg state via the intermediate $np_{3/2}$ level. To avoid scattering and heating of the cloud, the 780 nm laser is blue detuned from the resonance $5s_{1/2}, f = 2, m_f = 2 \rightarrow 5p_{3/2}, f = 3, m_f = 3$. Polarizations are chosen as σ^+ and σ^- to maximize the transition dipole moment and to conserve the spin. Both states, the $f = 2, m_f = 2$ component of the ground state and the $m_s = +1/2$ component of the Rydberg state have the same Zeeman shift and thus the transition frequency is independent from the magnetic field of the trap.

However, the polarizations of the lasers are only well defined in the center of the trap: Here, the offset field B_0 defining the quantization axis points in $-z$-direction and the polarizations of the lasers are adjusted accordingly (see Fig. 3.2). Further outwards the curvature of the magnetic trapping field tilts the magnetic field vector, i. e. also (π, π), (π, σ^-), and (σ^-, π) transitions are allowed which end up in the $m_s = -1/2$ component of the Rydberg state. The Zeeman shift of this component has opposite sign as the ground state and the other Rydberg component. Consequently, the transition frequency is sensitive to the strength of the magnetic field and the temperature of the cloud [71]. In a spectrum the Rydberg state therefore always appears as two lines (Fig. 3.4): a sharp and intense line corresponding to the addressed $m_s = +1/2$ state and a weaker one of the $m_s = -1/2$ state red shifted by $-2\mu_B B_0$ and broadened depending on the temperature, i. e. the size of the atomic sample.

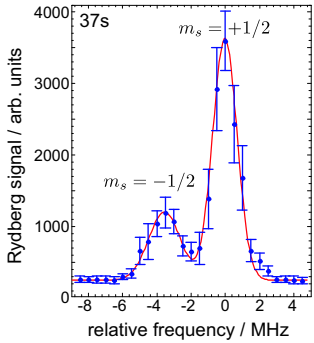

Fig. 3.4: Atomic spectrum.

Consequently, the transition frequency is sensitive to the strength of the magnetic field and the temperature of the cloud [71]. In a spectrum the Rydberg state therefore always appears as two lines (Fig. 3.4): a sharp and intense line corresponding to the addressed $m_s = +1/2$ state and a weaker one of the $m_s = -1/2$ state red shifted by $-2\mu_B B_0$ and broadened depending on the temperature, i. e. the size of the atomic sample.

3.2.1 Laser system

Narrowband excitation lasers are essential for photoassociation spectroscopy as the laser linewidth defines the accuracy of the measured binding energies (Chap. 2.3.3). Thus stabilized continuous wave lasers are used and a combined laser linewidth of $\Delta\nu<1$ MHz is reached. The two lasers are grating-stabilized diode lasers, one operating at 780 nm and the second at 961 nm. They are set up equally (Fig. 3.5), only their locking schemes are different and the light of the 961 nm diode is finally frequency-doubled to generate the excitation light of 481 nm for the upper transition to the Rydberg level (see Fig. 3.3).

Both laser systems consist of a narrowband master diode laser which is stabilized by regulating the grating angle and the laser current. The beam of the master laser is split in beams for generating the stabilization signal, monitoring the laser frequency on a Fabry-Perot interferometer and a wavemeter (not shown in Fig. 3.5) and finally the beam for the experiment. This light passes an accusto-optical modulator (AOM) used for scanning the frequency twice, before it seeds the slave diode laser. This setup of master and slave diode has the advantages of power amplification by the slave laser and it ensures a constant laser power during a scan of the double-pass AOM whose efficiency strongly depends on the frequency.
The short pulses of 500 ns to 150 μs needed in the experiment are generated by AOMs (200 MHz) used in single pass which create rectangular pulses with rise and fall times of 10-12 ns. In the setup of the red laser the beam of the slave diode passes the switching AOM before it enters the fiber bringing the light to the experiment (see Fig. 3.2). The light of the 961 nm slave is injecting a tapered amplifier diode

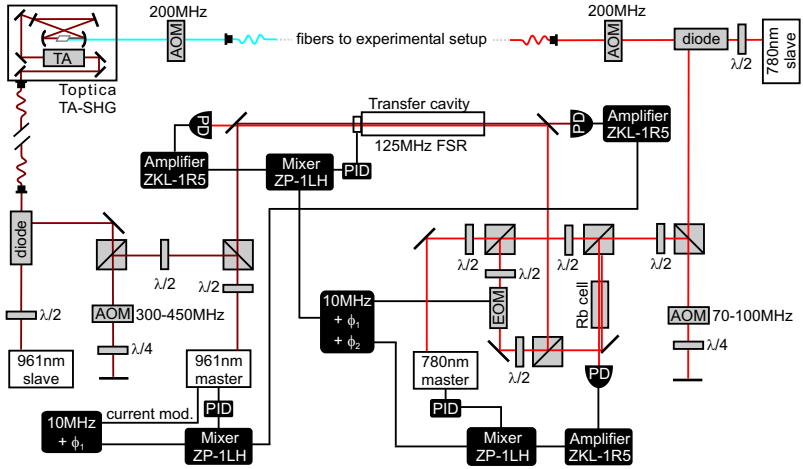

Fig. 3.5: Essential parts of the laser system and the locking scheme. Both excitation wavelengths are generated by diode lasers: The narrowband master lasers are stabilized to a spectroscopy (780nm) or a cavity (961nm) and seed two slave diodes for power amplification and stabilisation. The light of the 961nm diode is frequency-doubled in a commercial doubling cavity to generate the excitation wavelength of 481nm for the Rydberg states.

(TA) delivering 800 mW laser power which is frequency doubled in an external cavity[1]. The $KNbO_3$ crystal generates 250 mW of blue light at 481 nm. Also the blue light passes an AOM for switching the light and is brought by a fiber to the experiment. Although the usage of a fiber reduces the power of the blue light at the experiment to 70 mW it is necessary for purifying the beam profile to a perfectly Gaussian mode and also for pointing stability reasons.

To control the frequencies of the master lasers different locking schemes have to be used: The master laser at 780 nm is locked to the $5s_{1/2}, f = 2 \rightarrow 5p_{3/2}, f = 3$ transition in ^{87}Rb by a modulation transfer spectroscopy in a vapor cell [72]. The setup is similar to a saturation spectroscopy but the pump beam is additionally

[1] Toptica TA-SHG 110

phase-modulated by an EOM. In our experiment, the pump beam is composed of a carrier frequency ν_0 and sidebands $\nu_0 \pm 10$ MHz and aligned collinearly to the counter-propagating probe beam. If the pump beam is intense enough to saturate the addressed atomic transition in the vapor cell, the modulation is transfered to the originally unmodulated probe beam. This transfer can be described as four-wave mixing, where two frequency components of the pump beam ($\nu_0, \nu_0 \pm 10$ MHz) combined with the probe beam (ν_0) create a fourth beam, the sidebands of the probe beam: $\nu_0 \mp 10$ MHz. The beat signal of the probe beam and its sidebands are detected on a fast photodiode (PD) and demodulated by a mixer. The resulting sharp and strong dispersive signal shows a zero-crossing at the position of the atomic resonance which is used as reference for a PID-controller. It regulates the position of the grating as well as the laser current to the zero-crossing.

For the second laser at 961 nm there are no atomic resonances available and thus a tunable transfer cavity with 125 MHz free spectral range (FSR) is used as reference. The tunability is useful for an easy change of the addressed principal quantum number, but makes a third loop necessary for regulating the length of the cavity. Thus both master lasers are coupled into the cavity:

The length of the cavity is stabilized to one mode of the 780 nm master laser which is already locked to the MTS-signal. As shown in Fig. 3.5, a part of the phase-modulated pump beam of the spectroscopy is used. The phase modulation of the 780 nm beam allows to transform the dc signal of the cavity modes to a dispersive one by a mixer. The length of the transfer cavity is stabilized to its zero-crossing and thus to the maximum of the transmission through the cavity.

In the same manner the signal for locking the 961 nm master laser is generated, but here the current of the laser is modulated (10 MHz). This modulation is anyway needed for the Pound-Drever-Hall lock of the Toptica doubling cavity and in the end filtered out during the frequency conversion to 481 nm. The transmission signal of the 961 nm beam through the cavity is detected by a fast photodiode (PD), converted to a dispersive signal by a mixer and fed into a PID-controller. The feedback controls the grating and the laser current of the 961 nm master laser. More details about the electronic setup of the locking

schemes can be found in [71].

An upper limit for the combined laser linewidth $\Delta\nu$ for the $5s_{1/2}, f = 2, m_f = 2 \rightarrow ns_{1/2}, m_s = 1/2$ transition can be estimated by a rotary echo experiment [73]. The atoms are excited on resonance with a laser pulse of fixed duration T and during this pulse the phase of the excitation light is rotated by 180° by flipping the phase of one of the single-pass AOMs. The rotation of the phase leads to an inversion of the excitation if the atoms are excited coherently: flipping the phase is equal to changing the sign of the driving Rabi frequency. Ideally, there is no Rydberg population remaining in the sample if the phase flip τ occurs exactly after half the excitation time. Due to dephasing processes in the atomic sample or decoherence, e. g. due to a drift in the laser frequency during the pulse, the minimum at $\tau = T/2$ is washed out and vanishes for longer excitation times. If one neglects other dephasing and decoherence processes the laser linewidth $\Delta\nu$ can be calculated from the maximum pulse duration for which a minimum at $\tau = T_{max}/2$ is still observable by

$$\Delta\nu \leq \frac{1}{T_{max}} \implies \Delta\nu \leq 800 \text{ kHz} \ .$$

This result is in agreement with the peak-to-peak size of the stabilization signals of the master lasers.

3.2.2 Sequence, field ionization & detection

In the experiment, the Rydberg sequence starts with laser pulses of 500 ns to 150 μs duration, created by fast switching of the driving radio-frequency of two AOMs (Fig. 3.5). As soon as the excitation light is switched off, the electric field to ionize the Rydberg atoms and accelerate the produced ions towards the MCP is applied by two of the eight field plates in the vacuum chamber (Fig. 3.2). Their voltage is switched from 0 V during the Rydberg excitation to up to 2.5 kV directly after the laser pulse. For this purpose two fast high voltage transistor switches [2] are used. The time delay between light pulses and electric field pulse is 150 ns and the rise time of the high voltage

[2] Behlke HTS 61-03-GSM, 6 kV/30 A

is limited to 20 ns due to the capacitance of the field plates. After a time-of-flight of typically $\approx 2\mu$s the Rb^+ ions reach the detector. It consists of a MCP in Chevron configuration with a single anode and a cage to shield the high electric fields. The created ions enter the detector via the front grid of the cage which has a small attractive potential of -15 V and then get accelerated towards the front of the MCP. The front of the MCP is connected to -2 kV and the back is grounded. Thus the electrons detached from the front surface by incoming ions are multiplied in the channels of the MCP. Here, one primary ion leads to typically $G_{\mathrm{MCP}} \approx 10^5$ secondary electrons at the back of the MCP which then hit the anode and are measured as a short current pulse $I(t)$ (inset of Fig. 3.6).
For signal processing the anode is discharged over a resistor R and the voltage drop is amplified in a self-built circuit of gain G_{OP27} [50]. Thereby the current pulses of 100 ns width are converted in voltage pulses of 500 ns which are finally recorded by a PCI-digitizer card[3]. Although the length of the pulses increases due to the large resistance R their shape is not changed and the pulse area is still proportional to the number of detected ions

$$N_{ion} = \frac{1}{e\, G_{\mathrm{MCP}}} \int I(t)dt = \frac{1}{e\, R\, G_{\mathrm{MCP}} G_{\mathrm{OP27}}} \int |U(t)|\, dt\,, \qquad (3.2)$$

where e is the elementary charge and G_{MCP} the amplification of the MCP. For data evaluation, the voltage pulses are fitted by a reference pulse: this reference pulse is defined from several 100 averages of single pulses and the free fit parameter are the position in time t_{exp} and the height of the pulse which is proportional to the pulse area and thus to the number of Rydberg atoms [71]. As the ion pulse appears always at the same time t_{exp} for a given electric field, this method allows to filter noise with a different time-dependence and thereby improves the signal-to-noise ratio. A detailed characterization of the MCP detection scheme can be found in the thesis of J. Balewski [50].

[3] National Instruments NI PCI-5102, 50 ns time resolution

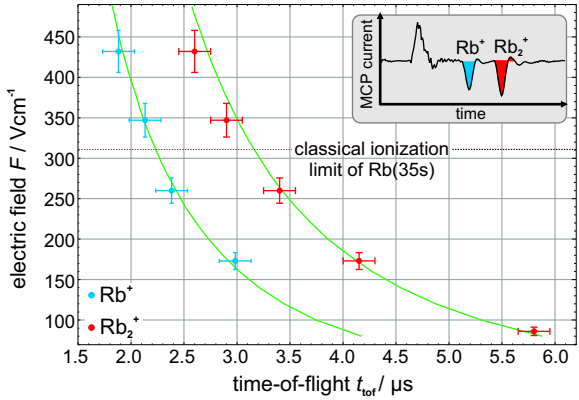

Fig. 3.6: Calculated and measured time of flights for Rb^+ and Rb_2^+. The solid lines are calculations for ions with masses of 87 amu and 174 amu, starting from the center of the trap with zero velocity. The data points represent the measured values which are fitted to the calculation by a constant time offset Δt. A typical current signal of the MCP is shown as inset.

Ion time-of-flights

In the experiment, not only Rb^+ but also Rb_2^+ ions are detected, which can clearly be identified in time-of-flight (Fig. 3.6). The difference in the spectral intensity distribution of the Rb_2^+ in comparison to the Rb^+ spectrum is a clear indication that Rb_2^+ is the product of an additional decay that dominantly occurs for the molecular states. Possible decay channels are discussed in Chap. lifetimes. Here, the observed time-of-flights for different electric fields are compared to an ion optics simulation[4] taking the geometry of the field plates and the chamber into account (Fig. 3.2). It is shown that the time delay between the first and second ion pulse and its dependence on the electric field is well reproduced by the calculation for ion masses of $m_{\mathrm{Rb}} = 87$ amu and $m_{\mathrm{Rb2}} = 174$ amu.

The exact point of ionization of the Rydberg atoms is not known. In the experiment, the time t_{exp} is measured with respect to the trigger

[4]SIMION 8.0, Scientific Instrument Services Inc. 2008

of the high-voltage switches and is longer than the real time-of-flight

$$t_{\mathrm{tof}} = t_{\mathrm{exp}} - t_{\mathrm{HV}} - t_{\mathrm{ion}}\,, \tag{3.3}$$

where t_{HV} is the time between the trigger and the point at which the voltage on the field plates reaches its maximum; a lower limit for t_{HV} is the delay between the light pulses and the field ionization. t_{ion} considers the time the Rydberg atoms are exposed to the electric field before they ionize.
The data shown in Fig. 3.6 are measured for the 35s Rydberg state. The voltage applied to the field plates is varied from 450 V to up to 2.25 kV, corresponding to electric fields between 86 V/cm and 432 V/cm. The errorbars represent the accuracy of the calibration of the electric field of 6% and the measurement of t_{exp} which is given by the resolution of the digitizer card (50 ns) and the jitter of the trigger. The total error is estimated to be $\pm$150 ns.
For each electric field several spectra are measured and evaluated for both ions. The line intensities in the Rb^+ spectrum are constant for 432 V/cm and 324 V/cm and drop by a factor of 10 when crossing the classical ionization limit of 311 V/cm. This means for $F < 311$ V/cm the Rydberg atoms are ionized by tunneling of the Rydberg electron through the barrier (Fig. 2.1). For the lowest field, no more Rb^+ ions are detected. In contrast, the Rb_2^+ ions are already present when the electric field is switched on, i. e. here $t_{\mathrm{ion}} = 0$. The intensities in their spectra are independent of the applied electric field and even for the weakest field a clear ion pulse is detected.
To compare the calculated time-of-flights with the ones in the experiment, the data are fitted to the simulation by subtracting a constant time offset Δt from the values of t_{exp}. The best agreement is achieved for $\Delta t(Rb^+) = 430$ ns and $\Delta t(Rb_2^+) = 300$ ns. These results are conform to the expectations that $\Delta t(Rb_2^+) = t_{\mathrm{HV}} > 150$ ns and $\Delta t(Rb^+) > \Delta t(Rb_2^+)$.

4. Ultralong-range Rydberg molecules

In chemistry, molecular bonds are divided into three primary types: covalent, ionic and van der Waals. In the first case, the atoms share their valence electrons equally which occupy molecular orbitals. A purely covalent bond requires that all atoms have the same electron affinity and can only be found for homonuclear molecules. The bonds in all heteronuclear molecules have also ionic character, where the charge of one or more valence electrons is partly transferred. An extreme example are the salts like NaCl in which the valence electron of the sodium atom is transferred to the chlorine atom. These two ions Na^+ and Cl^- are bound by their strong Coulomb interaction. In all of these molecules the binding occurs due to an overlap of the atomic wavefunctions and thus the bond lengths of these molecules are determined by the size of the atomic wavefunctions which are of the order of 0.5 nm.
The third type, the van der Waals molecules [74], are formed by weaker electrostatic interactions which have long range and leave the atomic wavefunctions nearly unchanged. A prominent example is the helium dimer [75, 76] having a bond length of 5.2 nm and tiny binding energies of only $9.5 \cdot 10^{-8}$eV, compared to 5 eV for the diatomic hydrogen. Even larger van der Waals molecules can be formed if Rydberg atoms are involved: The large size of the Rydberg wavefunction $\propto n^2$ and the tunability of their multipole forces by small electric fields allow to create giant Rydberg-Rydberg molecules of several micrometer size which are bound by dipole-dipole interaction [77].

A different kind of Rydberg molecule is studied in this work. It is composed of a Rydberg atom and a ground state atom and its binding mechanism cannot be described by one of these types. It is based solely on the scattering of the Rydberg electron from the ground state atom which is located dominantly in the last lobe of the Rydberg wavefunction (see Chap. 2.2.2). Classically, the ground state atom gets polarized and is bound to the "orbit" of the Rydberg electron. Thus the size of the molecule is determined by the size of the Rydberg wavefunction which ranges from 1780–2560 Bohr radii or 94–135 nm for the states studied in this work. Quantum-mechanically, the sign and strength of the electron–atom interaction is quantified by the scattering length (Chap. 2.2). In rubidium, only the triplet-scattering length A_0^T is negative and gives rise to a binding [6]. In the singlet case, the scattering length is positive and therefore the electron-atom interaction repulsive [54, 52].
This chapter presents the experimental results on photoassociation of these novel ultralong-range Rydberg molecules and studies of their fundamental properties: binding energies and vibrational level structure, polarizabilities as well as lifetimes.

4.1 Photoassociation spectra

In search of the weak bound molecules composed of a Rydberg atom and a ground state atom photoassociation spectroscopy was the method of choice: Two free atoms in the ground state are excited to a bound state, whereas one atom is excited to the Rydberg state and the other stays in the ground state – a Rydberg molecule is formed. Preconditions are first a distance between the free atoms that matches the molecular bond length and second a detuning of the excitation light from the atomic Rydberg state that matches the molecular binding energy, E_B. Then these molecules can directly be observed in a spectrum and their binding energy is measured as difference between the excitation frequencies of the molecular and the atomic Rydberg state (see Chap. 2.3.3).
This chapter starts with the photoassociation spectra of the diatomic molecules $\mathrm{Rb}(n\mathrm{s}) - \mathrm{Rb}(5\mathrm{s}), 34 \leq n \leq 40$ and compares the observed binding energies to the theory of s-wave scattering introduced in Chap. 2.2.2. Furthermore it is shown that aside from diatomic molecules also triatomic ones can be formed, consisting of one Rydberg atom and two ground state atoms independently bound to the Rydberg wavefunction. Their photoassociation spectra and binding energies are discussed in Chap. 4.1.3.

4.1.1 Binding energies of pure s-wave potentials

All experiments presented here are performed in ultracold atomic samples of $T \approx 3.5$ μK to maximize the density of ground state atoms. After preparation of the cloud the excitation pulse of 3μs length is applied and immediately afterwards an electric field of up to 432 V/cm is switched on and the created Rydberg atoms or molecules are ionized and accelerated towards the detector. A detailed description of the experimental sequence is given in Chap. 3. The spectra are taken by a repetition of the Rydberg sequence of laser excitation and detection of the Rydberg state of up to 61 times in the same atomic sample. Between the single excitations only the laser frequency is changed stepwise and thereby a spectrum is taken. The spectra for principal quantum numbers $n = 35 - 37$ are shown

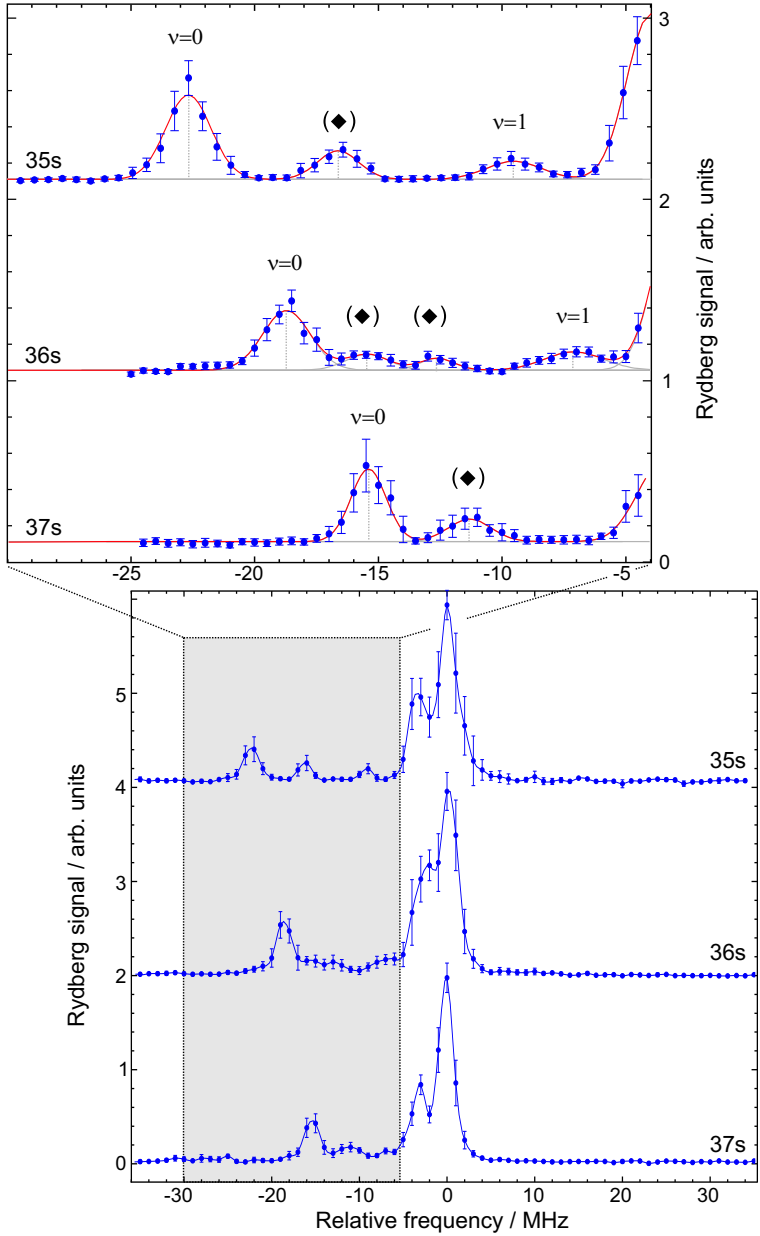

Fig. 4.1: Photoassociation spectra for $n = 35, 36, 37$. Frequencies are measured with respect to the atomic Rydberg state $ns_{1/2}, m_s = 1/2$. Line assignments result from bound states of the calculated s-wave potentials for a scattering length $A_0^T = -18.0\ a_0$.

in Fig. 4.1. They are centered around the atomic resonances and each spectrum is the average of 15 independent spectra, each of them measured in another atomic sample. The errorbars indicate the 2σ errors from the 15 independent measurements. The overview spectra are measured in two different frequency ranges, both including the atomic resonance $ns_{1/2}$. The spectra are evaluated, averaged and finally recomposed to one spectrum by use of the atomic resonance. In addition to the atomic state $m_s = 1/2$ at zero frequency also the $m_s = -1/2$ component of the atomic Rydberg state is excited. This state is Zeeman shifted to lower frequencies by 2-3 MHz (see Chap. 3.2). Further to the red side up to four weaker lines appear in the spectra attributed to the ultralong-range Rydberg molecules Rb(ns) − Rb(5s). This part of the spectra is measured again with higher spectral resolution and the results are shown in the upper graph of Fig. 4.1. Here, the spectra are averages of 30 independent spectra, each taken in a different atomic sample.

In principle one could compare the relative strengths of the resonances to calculate the Franck-Condon factor for the photoassociation. It is noticeable that the signal intensity of the molecular lines in Fig. 4.1 is still quite high compared to the signal on the atomic resonance. From the peak densities of the atomic samples of $n_g = 1.6 \cdot 10^{13}$ atoms/cm^3 and the corresponding distribution of separations between pairs of

Ryd.	Molecular binding energies E_B/ MHz			
state	$\nu = 0$	excited states		
34s	-27.4 ± 0.5	-	-	-
35s	-22.4 ± 0.5	-16.3 ± 0.5	-9.2 ± 0.7	-
36s	-18.7 ± 0.5	-15.4 ± 0.8	-12.6 ± 0.9	-7.1 ± 0.7
37s	-15.4 ± 0.5	-11.3 ± 0.8	-	-
40s	-8.8 ± 0.8	-	-	-

Tab. 4.1: Measured binding energies E_B of the ultralong-range Rydberg molecules $^3\Sigma(n\text{s} - 5\text{s})$.

atoms, the so-called correlation function, a Franck-Condon factor of $P_{FC} \approx 0.01$ is expected for the excitation of a pair of atoms to the molecular state. But due to the strong van der Waals blockade of the Rydberg excitation the atomic lines are highly suppressed (Chap. 2.1.4). Therefore the Franck-Condon factor can not be determined from the signal ratio of the molecular and atomic line.

The binding energies are measured as molecular line positions with respect to the atomic resonance $ns_{1/2}m_s = 1/2$. For this purpose the lines are fitted by Gaussian profiles; their centers are indicated in Fig. 4.1. Similar spectra as those in Fig. 4.1 have been taken for Rb(34s) and Rb(40s) (Appendix Fig. 6.1). The binding energies of all states studied in this work are presented in Tab. 4.1. The accuracy of the values is given either by the laser linewidth (±0.5 MHz) or the 95% confidence bound of the Gaussian fit, depending on which of both errors is larger. For each principal quantum number the deepest bound state shows the strongest signal and is assigned to the vibrational ground state $^3\Sigma(n\mathrm{s} - 5\mathrm{s})(\nu = 0)$.
For a quantitative comparison of measurement and theoretical prediction the binding energies of the vibrational ground states $\nu = 0$ in Tab. 4.1 are fitted by the pure s-wave potential (eq. 2.55 in Chap. 2.2.2)

$$\begin{aligned} V_s(n,l,r) &= \frac{1}{2} \cdot A^T\left[k(r)\right] \cdot \left|R_{nl}(r)\right|^2, \text{ with} \\ A^T\left[k(r)\right] &= A_0^T + \frac{\pi\alpha_{5s}}{3}k(r) + O(k^2)\,. \end{aligned} \tag{4.1}$$

The radial wavefunction of the Rydberg state $R_{nl}(r)$ is defined by the quantum defect which is accurately known (see Chap. 2.1.1) and also the ground state polarizability of rubidium α_{5s} is measured precisely to be $\alpha_{5s} = 319$ *a.u.* [51]. Thus the only free fit parameter is the triplet scattering length for zero energy, A_0^T. Theoretical predictions for A_0^T vary between -13 a_0 and -16.9 a_0 [52, 53].
The best agreement between experiment and theoretical model is found for $A_0^T = -18.0$ $a_0 \pm 0.5$ a_0 (Fig. 4.2). The n-dependence of the molecular binding energy of the vibrational ground state $\nu = 0$ is in excellent agreement with the model 4.1 assuming only s-wave scattering between the Rydberg electron and the ground state atom.

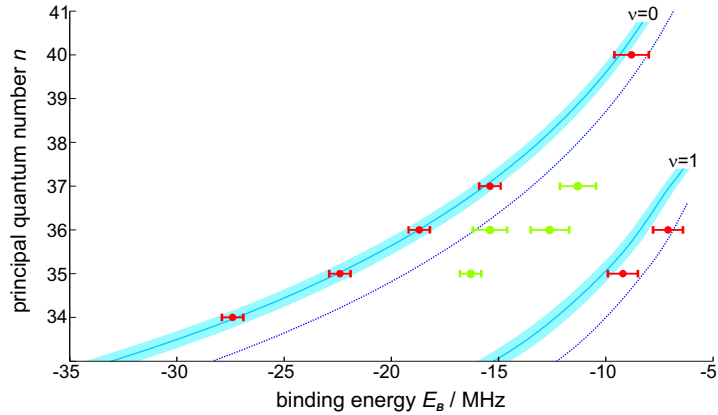

Fig. 4.2: Measured and calculated binding energies, E_B. The solid lines are the calculated binding energies for the $\nu = 0$ and $\nu = 1$ states, assuming a scattering length $A_0^T = -18.0\ a_0$; the shaded areas show the theory for $A_0^T = -18.0\ a_0 \pm 0.5\ a_0$. Theoretical results for $A_0^T = -16.05\ a_0$ [6] are also included (dotted line). The observed excited molecular states which can not be assigned by the s-wave potential (eq. 4.1) are shown in green.

In addition, the model also predicts a first excited state $\nu = 1$. Although there is an excited state in the 35s and 36s spectrum which is in good agreement with the prediction for the first excited state, the additionally observed lines are a clear hint that the assumption of pure s-wave scattering is not strictly valid. The influence of p-wave scattering on the molecular potential and the full solution of the problem of electron–atom scattering is discussed in Chapter 4.4.

4.1.2 Triatomic molecules

In principle, the binding force of the Rydberg electron is not restricted to only one ground state atom. As long as the presence of the ground state atoms does not change the Rydberg wavefunction significantly, also bound states of one Rydberg atom and two or more ground state atoms should exist [78]. Their observation is harder, be-

Rydberg state	vibrational ground state	
	dimer	trimer
35s	-22.8(5) MHz	-45.5(8) MHz
36s	-19.0(5) MHz	-37.9(5) MHz
37s	-16.2(5) MHz	-31.6(8) MHz

Tab. 4.2: Measured binding energies E_B of the vibrational ground states $\nu = 0$ of the dimer and trimer molecules.

cause their Franck-Condon factors are determined by the $i-$th power of the Franck-Condon factor of the corresponding dimer, P_{FC}, where i is the number of ground state atoms in the molecule. Under the assumption that there are no interactions between the ground state atoms, their binding energies should simply sum up to the binding energy of the whole molecule. Thus the deepest bound state of a triatomic molecule would have twice the binding energy of the dimer ground state $\mathrm{Rb}(n\mathrm{s}) - \mathrm{Rb}(5\mathrm{s})(\nu = 0)$.
To excite a significant fraction of these trimer molecules the measurements described in Chap. 4.1.1 are repeated for the 35s, 36s and 37s states but the photoassociation is performed with much higher laser intensity. To reduce statistical fluctuations in the signal strength the spectra are averaged over 50 independent measurements.

In the same manner as before the spectra are plotted with respect to the atomic resonances and the line positions are determined by fits of Gaussian profiles (Fig. 4.3). In each of the spectra there appear additional bound states, where the leftmost of these lines can be assigned as vibrational ground state $\nu = 0$ of the ultralong-range Rydberg trimer. Their binding energies are compared to the dimer ones in Tab. 4.2 showing a good agreement between the measurement and the assumption of two independently bound ground state atoms. All other lines cannot be assigned by the simple theory of pure s-wave scattering. The origin of these bound states will be discussed in Chap. 4.4.
By comparison to the dimer spectra in Fig. 4.1 it is noticeable that

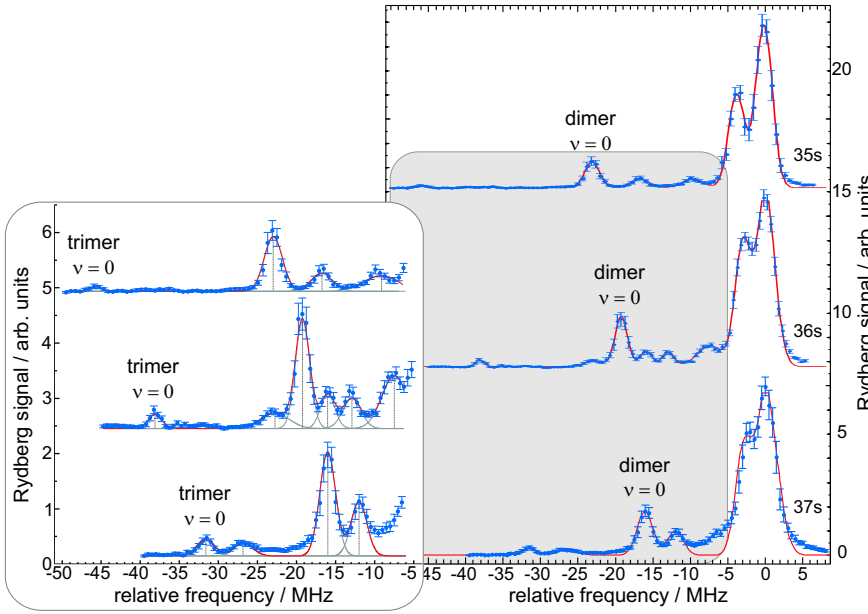

Fig. 4.3: Photoassociation spectra of dimers and trimers for $n = 35, 36, 37$. Frequencies are measured with respect to the atomic Rydberg state $ns_{1/2}, m_s = 1/2$. Line assignments result from bound states of the calculated s-wave potentials for a scattering length $A_0^T = -18.0\ a_0$.

the dimer lines in Fig. 4.3 are already broadened due to saturation probably caused by the van der Waals interaction just like in the case of the atomic Rydberg lines. Thus also in these spectra a direct comparison of the line strengths and a deduction of the Franck-Condon factors is not possible.

4.2 Stark effect

The model of C. Greene [6] to describe the binding mechanism of the ultralong-range Rydberg molecules is based on the polarization of the ground state atom by the Rydberg electron and considers the Rydberg wavefunction as unperturbed, i. e. there is no back action of the polarized ground state atom upon the Rydberg electron.
This assumption can be verified by a Stark spectroscopy which is a sensitive tool to probe changes in the isotropy of the wavefunction. If the influence of the ground state atom on the Rydberg wavefunction can be neglected the polarizabilities of the Rydberg atom and molecule should be the same. Otherwise the ground state atom would on its part attract the Rydberg electron and slightly increase its probability density at the position r of the ground state atom. The resulting dipole moment should be visible in a Stark spectrum.

The Stark spectroscopy is performed for the states 35s, 36s and 37s for electric fields in the range of -3 V/cm to +3 V/cm. The span in frequency is chosen that the spectra include the vibrational ground states of the ultralong-range dimer Rb(ns) − Rb(5s) as well as the atomic resonances. The Stark maps for the three principal quantum numbers $n = 35-37$ are plotted in Fig. 4.4. They are measured by applying a constant electric field F via the field plates also used for field ionization (see Fig. 3.2). Apart from the electric field the sequence is the same as for the photoassociation spectroscopy of Chap. 4.1.1 and 4.1.3. Here, each of the spectra is the average of five independent experiments.
Similar to the atomic Rydberg states Rb(ns) the molecular states Rb(ns) − Rb(5s)($\nu = 0$) of all three principal quantum numbers, n, show a quadratic shift in the electric field. To ascertain the atomic and molecular polarizabilites the spectra are first fitted by Gaussian profiles to extract the line positions of the dimer state $\nu = 0$ and the atomic line, respectively. Finally, the line positions versus electric field F are fitted by parabolas to determine the polarizabilities α (Tab. 4.3).

First, the results for the atomic polarizabilites are compared to experimental data of O' Sullivan and coworkers [36]. They characterized the ^{85}Rb(ns) states in electric field for a large range of principal quan-

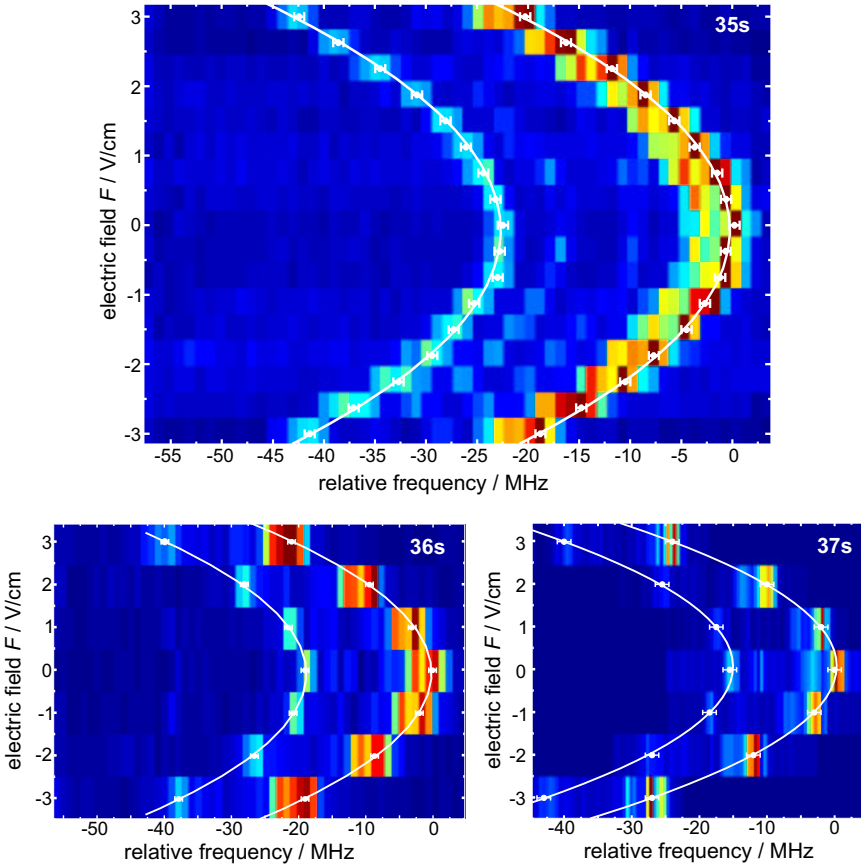

Fig. 4.4: Stark spectra of the atomic Rb(ns) state and the molecular $^3\Sigma(n\mathrm{s}-5\mathrm{s})(\nu=0)$ state for $n = 35, 36, 37$. For all three principal quantum numbers n the line centers of both the atomic state (right) and molecular state (left) show a quadratic Stark effect. The errorbars represent the final frequency resolution which is 0.5 MHz for the states 35s and 36s and 1 MHz for the 37s state. The uncertainty of absolute values for the electric field is discussed in the text. The polarizabilities corresponding to the parabola fits are summarized in Tab. 4.3.

tum numbers $15 \leq n \leq 80$ and interpolated the n-dependence of the polarizability by a power law (see 2.1.3). In Fig. 4.5 the atomic polarizabilities of Tab. 4.3 are plotted together with their interpolation for $n = 31 - 39$, where the width of the curve represents the uncertainty of the fit. The results of this work are very close to the prediction of their interpolation, although the value for the 36s state is slightly smaller.
It has to be noted that the atomic polarizabilities of this work together with other data have been used for the calibration of the electric field. In total, the Stark data for the 35s, 36s, 37s and the 43s state measured earlier in the same setup [64] were fitted to the experimental data of O' Sullivan as well as to *ab initio* results. A detailed description of the electric field calibration is given by J. Balewski [50]. The resulting calibration for the electric field

$$F = (0.191 \pm 0.001)\ \mathrm{cm}^{-1} \cdot U\ ,$$

where U is the voltage applied by the field plates, is also used in this work. The error in the calibration of 0.1% leads to an additional systematic uncertainty in the polarizability of 0.2%. This error is not included in the errors of the polarizabilities in Tab. 4.3 because this work focusses on the relative values.
A comparison of the atomic and molecular ground state polarizabilities shows a good agreement: The values for atomic and molecular states are very close. Under the consideration of the rela-

Ryd.	molecular polarizability		atomic polarizability	
state	$\alpha/10^7$ a.u.	$\alpha/\mathrm{MHz/(V/cm)^2}$	$\alpha/10^7$ a.u.	$\alpha/\mathrm{MHz/(V/cm)^2}$
35s	1670(4)	4.158(13)	1690(8)	4.21(2)
36s	1956(26)	4.87(7)	1945(31)	4.85(8)
37s	2572(96)	6.40(24)	2519(96)	6.27(24)

Tab. 4.3: Polarizabilities of the molecular states $^3\Sigma(n\mathrm{s} - 5\mathrm{s})(\nu = 0)$ and the atomic ns state of ^{87}Rb. The accuracies contain the quality of the quadratic fits. The polarizabilities given here are additionally affected by a systematic error of 0.2% originating from the electric field calibration [50].

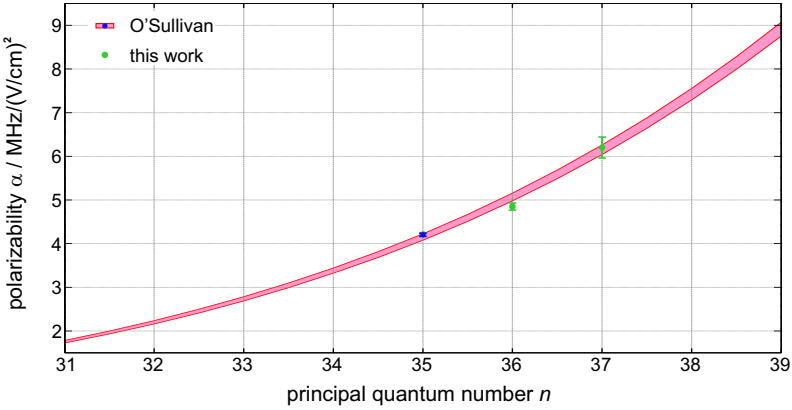

Fig. 4.5: Polarizabilities of the ns Rydberg states. The experimentally determined values (green) given in Tab. 4.3 are compared to the results of O' Sullivan and coworkers [36]. They measured the Stark shifts of ns Rydberg states for $15 \leq n \leq 80$ and interpolated the n-dependence (red).

tive errors only the polarizability of the molecular state Rb(35s) − Rb(5s)($\nu = 0$) deviates from the atomic one. This state was investigated with the highest precision in frequency and measurement statistics. Here, the difference between the mean values for the polarizability is 0.05 MHz/(V/cm)^2 where the sum of the errors is 0.03 MHz/(V/cm)^2. Thus the deviation of the atomic and molecular polarizability is only 0.5% which is a confirmation of the assumption, that the back action of the ground state atom upon the Rydberg electron is very weak and can be neglected for the modelling of the molecular potential.

4.3 Lifetimes

Aside from the Stark effect, the lifetime of the ultralong-range molecules is an important property giving a deeper insight in the molecular binding. If other decay mechanisms, based either on the presence of the ground state atom within the Rydberg wavefunction

or the high density of ground state atoms needed for the creation of these exotic molecules, do not play any role, the lifetime of the molecules is supposed to be equal to the atomic lifetime. However, the following data show a significant reduction of the molecular lifetimes compared to the atomic Rydberg states. Although this issue cannot be explained quantitatively within the scope of this thesis, this chapter summarizes the experimental observations and qualitatively discusses possible additional decay channels.

The effective lifetimes of the atomic states Rb(ns) are about $\tau_{\text{eff}} \approx 30$ μs (see Chap. 2.1.2) and the corresponding natural linewidths $\Delta\nu_{\text{nat}} = (2\pi\tau_{\text{eff}})^{-1} \approx 5$ kHz far below the resolution of this experiment. Thus the lifetime is measured by applying an excitation pulse of fixed length (3 μs) either to the molecular or the atomic resonance and changing the time delay between excitation and field ionization from 0 μs to 150 μs. The time constant of the exponentially decreasing number of detected ions is the lifetime, τ, of the molecules and Rydberg atoms, respectively. These experiments are performed for the trimer and dimer ground states as well as the atomic Rydberg states for 35s, 36s and 37s. The results are presented in Tab. 4.4, the original data can be found in the Appendix 6.1.

Ryd. state	calc. lifetimes /μs			measured lifetimes /μs		
	τ_{rad}	τ_{bb}	τ_{eff}	τ_{atom}	τ_{dimer}	τ_{trimer}
35s	50.3	58.5	27.0	65 ± 9	15 ± 3	15 ± 2
36s	55.2	61.9	29.2	57 ± 7	17 ± 4	15 ± 3
37s	60.4	65.3	31.4	57 ± 5	18 ± 6	16 ± 3

Tab. 4.4: Theoretical and experimental values for the lifetime. τ_{rad}, τ_{bb} and τ_{eff} are the calculated radiative [25], blackbody limited [31] and the resulting effective lifetimes of the atomic Rydberg state. The calculation includes blackbody induced transitions at 300 K (Chap. 2.1.2). Experimental values represent the time constant of the exponential decrease in ion signal, which are measured for the atomic state $ns_{1/2}, m_s = 1/2$ and the dimer and trimer ground states, $\nu = 0$. The errors (2σ) are determined from an exponential fit to the data.

First, it has to be noted that the observed atomic lifetimes are closer to the pure radiative lifetimes than to the effective ones corrected by the influence of blackbody induced transitions. This fact can be explained by the experimental procedure:
Blackbody induced transitions lead to a population transfer which dominantly occurs to the energetically closest Rydberg states, here the closest p states $(n-1)$p and np (Chap. 2.1.2). This transfer is only observed experimentally if a state-selective detection scheme is used: The electric field for ionizing the Rydberg states has to be chosen in a way that the states np, ns and $(n-1)$p are addressed independently. But even then the Rydberg state closest to the ionization threshold would ionize after short time due to tunneling of the Rydberg electron through the barrier (see Chap. 2.1). Therefore also a high time resolution in the detection scheme is needed to distinguish between the charges from the addressed Rydberg state and lower lying states, which can only be realized by detecting electrons instead of ions [27]. Hence, the current experiment is not sensitive to blackbody induced transitions as the detection scheme does not allow for a state-selective detection of the Rydberg ions.
Consequently, the observed atomic lifetimes should be compared to the theoretical prediction for the pure radiative lifetimes τ_{rad} rather than to the effective values. Under consideration of the error, the measured lifetimes for Rb(36s) and Rb(37s) agree with the pure radiative lifetime τ_{rad}. For the Rb(35s) state the measured lifetime is slightly longer than the theoretical radiative value.

Strikingly for the molecular states are the significantly shorter lifetimes, for the dimers as well as for the trimers, compared to the atomic lifetimes. They decay a factor of 3-4 faster than the corresponding atomic states. Aside from these much shorter lifetimes, molecular ions Rb_2^+ are detected in the experiment which were successfully identified by a time-of-flight analysis (Chap. 3.2.2) and which dominantly appear at the molecular resonances (Chap. 4.4). Therefore it is probable that they are a product of an additional decay occurring only for the molecules.
The following paragraph 4.3.1 starts with the description of their radiative and effective lifetime. The treatment is similar to the atomic case, but the molecules can not only decay to unbound states by

radiative or blackbody induced decay, the thermal radiation field couples them also to other bound states. Possible decay channels leading to the formation of molecular ions are discussed at the end of the chapter.

4.3.1 Decay channels

In analogy to the atomic Rydberg states, the molecules $^3\Sigma(n\mathrm{s} - 5\mathrm{s})(\nu = 0)$ can decay radiatively to a pair of free atoms

$$\mathrm{Rb}(n\mathrm{s}) - \mathrm{Rb}(5\mathrm{s}) \longrightarrow \mathrm{Rb}(n'\mathrm{p}) + \mathrm{Rb}(5\mathrm{s}) + h\nu,\ n' \ll n$$

and the corresponding radiative lifetime τ_{rad} is equal to the one of the atomic state $\mathrm{Rb}(n\mathrm{s})$ given in Tab. 4.4.

As already discussed for the atomic case blackbody induced transitions have a significant effect on the lifetime of Rydberg states (Chap. 2.1.2). The same is true for the molecular states, but the thermal radiation field couples a molecular state not only to other atomic Rydberg states, but also to all other *bound* states which are in reach by a single photon and whose wavefunctions have a significant overlap with the wavefunction of the initial state. Although these "bound–bound" transitions do not change the lifetime τ_{bb}, they are discussed here briefly.
The molecules studied in this work, the $^3\Sigma(n\mathrm{s} - 5\mathrm{s})$, can undergo transitions by stimulated absorption or emission of one photon either to the atomic states $n'\mathrm{p}$, or to molecular states $^3\Sigma(n'\mathrm{p} - 5\mathrm{s})$. From all possible transitions to $(n'\mathrm{p} - 5\mathrm{s})$ states, the molecular wavefunction $\nu = 0$ has the largest overlap with the energetically neighbouring states (see Fig. 4.6). This results from the fact that the position of the outermost well of the molecular potential $V_s(n, l, r)$, given by eq. (4.1), depends only slightly on the angular momentum, l, of the Rydberg state. The spatial overlap of the vibrational states is quantified by the Franck-Condon factor

$$P_{FC}(n\mathrm{s}\nu \to n'\mathrm{p}\nu') = \left| \int_0^\infty \phi_{n'\mathrm{p}\nu'}(r) \cdot \phi_{n\mathrm{s}\nu}(r)\, dr \right|^2 \tag{4.2}$$

where $\phi_{nl\nu}(r)$ are the vibrational wavefunctions also depicted in Fig. 4.6.
To calculate the decay rate caused by blackbody induced transitions $\tau_{bb}^{-1}(ns\nu)$, the Einstein-B-coefficient of the corresponding atomic state, $B_{ns\to n'p}$, defined in eq. (2.20), has to be weighted by the sum of the Franck-Condon factors:

$$B_{ns\nu\to n'p} = B_{ns\to n'p} \cdot \left[\sum_{\nu'} P_{FC}(ns\nu \to n'p\nu')\right] \tag{4.3}$$

and in analogy to the atomic states, the decay rate is the sum of the Einstein-B-coefficients over all states

$$\tau_{bb}(ns\nu) = \left[\sum_{n'p} B_{ns\nu\to n'p}\right]^{-1} . \tag{4.4}$$

But as each set of vibrational states ν' builds a basis of normalized eigenstates, the sum of the Franck-Condon factors is

$$\sum_{\nu'} P_{FC}(ns\nu \to n'p\nu') = 1 \ , \tag{4.5}$$

which means the blackbody reduced lifetime τ_{bb} of a molecular state (4.3) is equal to the lifetime of the corresponding atomic Rydberg state, and thus also the effective lifetimes τ_{eff} are the same.

As example, the Franck-Condon factors of the vibrational ground state of the dimer ${}^3\Sigma(35\mathrm{s} - 5\mathrm{s})(\nu = 0)$ with the vibrational states $\nu = 0, 1$ of the closest p-states are shown in Fig.4.6: The depth of the molecular potentials $V_s(n, l, r)$ scales with the angular momentum, l, of the Rydberg state as $2l + 1$. Therefore, the potentials of the closest states $(34\mathrm{p} - 5\mathrm{s})$ and $(35\mathrm{p} - 5\mathrm{s})$ are a factor of ≈ 3 deeper than of the addressed $35s$ state. This leads to a larger number of vibrationally excited states, where all of them can be populated by blackbody induced transitions. In Fig. 4.6 only the localized states $\nu = 0, 1$ are shown; higher vibrational states with a spread of the wavefunction over several potential wells are not considered.

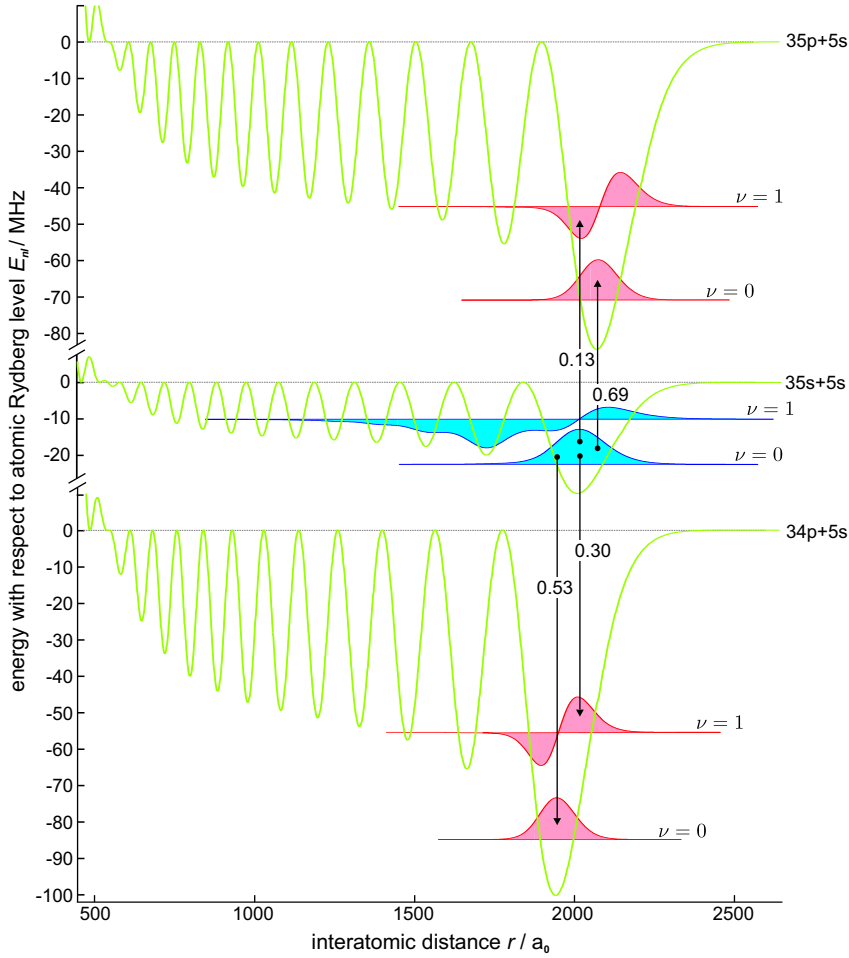

Fig. 4.6: Molecular state $^3\Sigma(35s - 5s)(\nu = 0)$ and molecular states $\nu = 0, 1$ of the energetically closest $p-$states from eq. (4.1). Exemplarily, the Franck-Condon factors defined by eq. (4.2) are included for the states $\nu = 0, 1$ for the $p-$states. Due to the limitations of the model (4.1), the calculation here is restricted to the states well localized in the outermost potential well, which largely arise from s-wave scattering.

In conclusion, the blackbody limited lifetimes of the molecular states are expected to be equal to those of the atomic Rydberg states. But unfortunately, the population transfer to other molecular as well as atomic Rydberg states cannot be detected in the experiment directly. In the future, it might be possible to determine the time constant of this decay from a rotary echo experiment [73] which is sensitive to decoherence processes. But therefore all other possible sources of decoherence, e. g. the linewidth of the excitation lasers, have to be well controlled on the time scale of the corresponding lifetime.
As the population transfer caused by blackbody radiation is not detected in the experiment, it is no explanation for the measured reduced lifetimes of the molecules. There have to be additional decay channels that only or dominantly affect the molecular Rydberg states and which are responsible for the difference in the measurement between atomic and molecular Rydberg states (Tab. 4.4) as well as the formation of molecular ions Rb_2^+. Two possible decay channels are described in the following paragraph.

Molecular ion formation

The observation of molecular ions Rb_2^+ (see Chap. 3.2.2) is a clear indication for an additional decay channel based on the presence of the ground state atom inside the Rydberg electron wavefunction. In the literature, two ionization processes in rubidium can be found which lead to the formation of Rb_2^+ and which are possibly responsible for the faster decay of the molecules, namely Hornbeck-Molnar ionization [79]

$$\mathrm{Rb}(ns) + \mathrm{Rb}(5s) \rightarrow \mathrm{Rb}_2^+ + e^- \tag{4.6}$$

and ion-pair formation [80]

$$\mathrm{Rb}(ns) + \mathrm{Rb}(5s) \rightarrow \mathrm{Rb}^+ + \mathrm{Rb}^-. \tag{4.7}$$

In the first process which is also called autoionization, the Rydberg atom and the ground state atom have to come as close as 1.5 nm [81], e. g. during a collision. At this distance, the repulsive branch $^3\Sigma$ of Rb(35s)-Rb(5s) and the attractive branch $^0\Sigma$ of $\mathrm{Rb}^+ - \mathrm{Rb}(5s)$ cross and Rb_2^+ can be formed.

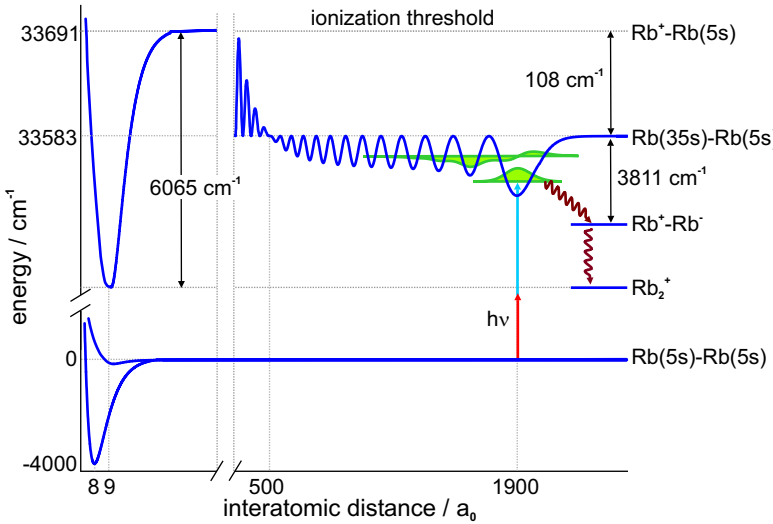

Fig. 4.7: Molecular potential curves for Rb_2 [62], $^3\Sigma(35s - 5s)$ and Rb_2^+ [62]. The electron affinity of rubidium (3919 cm^{-1}) [82] makes the ion-pair formation energetically possible. The ground state of the molecular ion lies 5957 cm^{-1} below the vibrational states of the Rydberg molecule and even below the ion-pair state. Energies are not to scale.

The ion-pair formation is based on the capture of the Rydberg electron by the ground state atom. This capture is energetically possible, as the electron affinity of rubidium is much larger than the binding energy of the Rydberg electron (Fig. 4.7). With high probability, the two oppositely charged ions will collide due to the strong Coulomb attraction and Rb_2^+ can be formed. Thus the molecular ion Rb_2^+ can result as a decay product of both channels.
Hornbeck-Molnar ionization and ion-pair formation have both been studied in the last decades and were detected for rubidium [79, 82, 80] and other alkalis [83, 84] in high-pressure vapor cells.

However, the study of these processes in the experiment is a hard task as the time scales of these decays are fast, e. g. the time for the ions Rb^+, Rb^- to collide classically is shorter than one nanosec-

ond. To distinguish between the two processes, the decay products, namely Rb^-, have to be observable in the experimental setup. The setup used in this work is restricted to the detection of ions, because electron detection requires a much better control of the electric fields and very short distances between excitation region and detector. The search for negative ions Rb^- in the work presented here was not successful. It might be that the ion pairs collide very fast and efficiently, so that not enough negative ions reach the detector. Therefore it is not possible to exclude the occurrence of ion-pair formation in the experiment from the current experimental data.
A promising theoretical task is the calculation of the inwards tunneling rates of the ground state atoms. They would give an estimate of the time constants for the formation of Rb_2^+ and maybe give a deeper insight in the origin of the reduced lifetimes of the molecules compared to the atomic states. Moreover, these tunneling rates should depend on the vibrational state and be significantly larger for the excited states with a large spread in r. A dependence of the lifetime on the vibrational states could be verified in future experiments.

4.4 Full solution of e^- – atom interaction

The results described in this paragraph are achieved in a cooperation and base on calculations of Weibin Li, T. Pohl and coworkers. Therefore and as this work has recently been published [85], only the essential conclusions are discussed.

The s-wave pseudopotential (2.54) describes the vibrational ground state $\nu = 0$ of the ultralong-range Rydberg molecules, but fails for the excited states which are clearly observed in the spectra. Consequently, p-wave contributions to the molecular potential curves have to be taken into account. The calculations of Weibin Li, T. Pohl and coworkers show, that also the perturbative approach by Omont for the p-wave (2.50), (2.53) cannot reproduce the vibrational spectra. They performed non-perturbative Green's function calculations of the molecular potentials and thus considered the full Hamilton operator $H_{\text{atom-e}^-}$ for the electron-atom interaction (2.43). The resulting molecular potential curve for Rb(35s) and the vibrational states

are shown in Fig. 4.8:
The outermost potential well is nearly unchanged compared to the pure s-wave potential, but the barriers between all other wells are lowered by the avoided potential crossing due to a p-wave shape resonance [3, 86], which is shown in the inset. In the inner region, $r < 1200\ a_0$, the molecular potential drops by more than 40 GHz, and hence the wavefunctions in this region behave like those of free particles. The molecular wavefunctions located in the outer region, $r > 1200\ a_0$, can be divided in two classes: Firstly, there are vibrational states which are confined in one of the potential wells, like the state ($\diamond$) and the state at $r \approx 1400\ a_0$ with a binding energy of $E_B = -26$ MHz. The second class are vibrational states with a large spread in r. Their binding energies are even smaller than the potential barriers, which means classically, these states would not be bound. It turns out that these states are stabilized in the outer region of the molecular potential by quantum reflection at the steep poten-

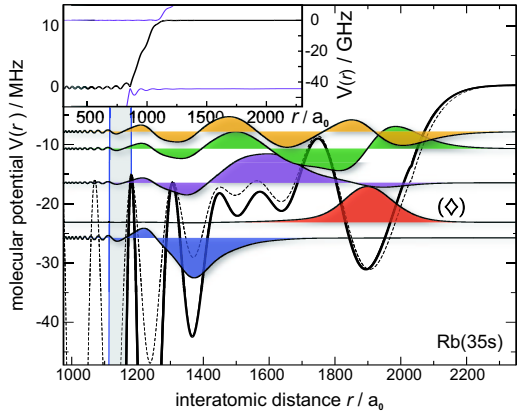

Fig. 4.8: Molecular potential curves for Rb(35s). Results from Green's function calculations (solid line) are compared to the model potential (4.8) with an effective s-wave scattering length $A_0^{\text{eff}} = -19.48\ a_0$ (dashed line).The rapid potential drop caused by the avoided crossing around $r = 1200\ a_0$ is shown in the inset. The vibrational ground state $\nu = 0$ of the pure s-wave potential is marked by $\diamond$ which constitutes the true vibrational ground state of the molecule.

tial drop at $r = 1200\ a_0$. Calculations of the reflexion coefficient $\Re$ of an outgoing wave show that the reflexion coefficient is as high as $\Re \geq 0.7$ for energies equal to those of the vibrational states of the Rydberg molecules [85].
Furthermore, Fig. 4.8 compares the potential from Green's function calculations to the pseudopotential (2.50) considering s- and p-wave scattering

$$\begin{aligned} V_{\text{pseudo}}(r) &= V_{\ell=0}(r) + V_{\ell=1}(r) \\ &= 2\pi A_0^T[k] \cdot |\psi_{nlm}(r)|^2 + \\ &\quad \frac{6\pi}{k^2} A_1^T[k] \, |\nabla \psi_{nlm}(r)|^2 \ . \end{aligned} \tag{4.8}$$

This pseudopotential reproduces the outermost potential well which arises dominantly from s-wave scattering, if the scattering length is adjusted to be $A_0^{\text{eff}} = -19.48\ a_0$. Thus the binding energy of the vibrational ground state ($\diamond$) can also be calculated from a pure s-wave potential, if an effective scattering length is used. But the excited vibrational states, especially the deep bound state at $r = 1400\ a_0$, occur only for the result of the full calculation.

The theoretical binding energies are compared to the experimental results in Tab. 4.5 and also included in the spectra in Fig. 4.9. From these Green's function calculations, all vibrational dimer states are assigned. Even deeper bound states than the state ($\diamond$) can be identified as dimer states, e. g. the the state at $r \approx 1400\ a_0$ in Rb(35s-5s), which otherwise would have been attributed to an excited state of the trimer molecule.
The theoretical results for the trimer ground states are also included, but as the dimer as well as the trimer ground states arise from s-wave scattering, also with this advanced calculation the binding energy of the trimer ground state is a factor of two larger than the one of the dimer state ($\diamond$).

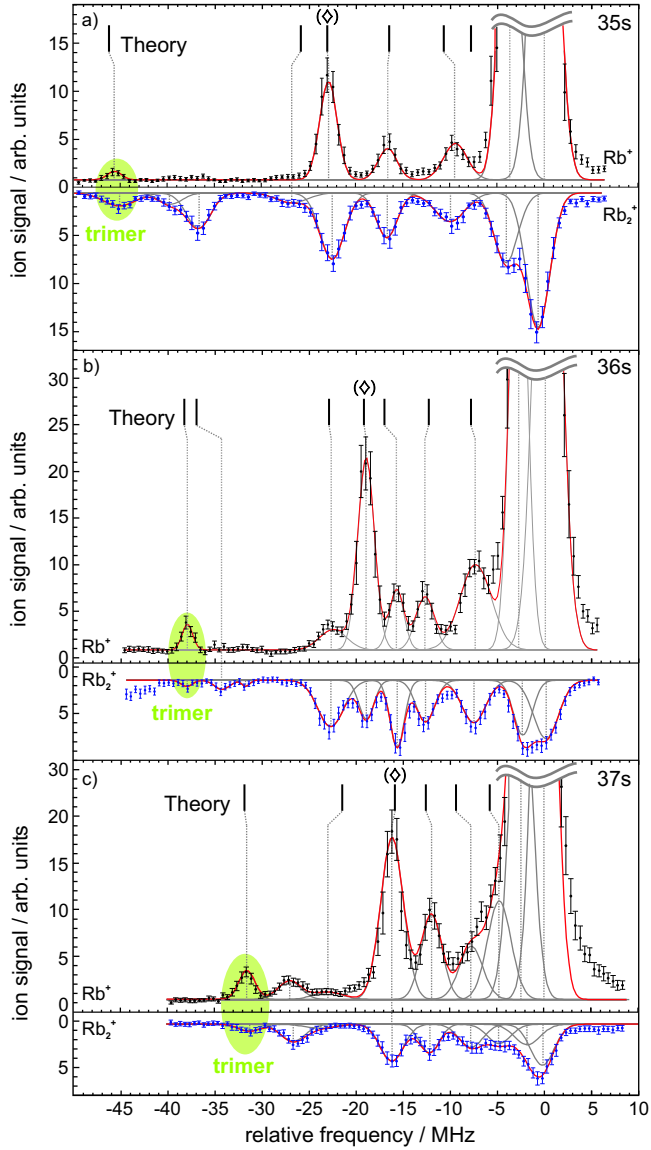

Fig. 4.9: Photoassociation spectra for $n = 35, 36, 37$. Frequencies in all spectra are measured with respect to the atomic transition $5s_{1/2} \rightarrow ns_{1/2}$. The upper parts show the atomic ion spectrum Rb^+(black) also shown in Fig. 4.3 and the lower ones the spectra of the molecular ions Rb_2^+ (blue). Calculated binding energies are indicated by vertical lines.

35s	measurement		theory	36s	measurement		theory	37s	measurement		theory
state	Rb_2^+	Rb^+		state	Rb_2^+	Rb^+		state	Rb_2^+	Rb^+	
	/	/	-7.8		−7.7(6)	−7.4(6)	−7.8		−4.8(10)	/	−5.8
	−9.9(7)	−8.9(7)	−10.7		−12.8(9)	−12.8(9)	−12.3		−7.8(10)	/	−9.4
	−16.6(5)	−16.5(5)	−16.5		−15.8(8)	−15.8(5)	−17.0		−12.2(5)	−12.0(5)	−12.6
♢	−22.4(5)	−22.8(5)	−23.1	♢	−19.0(5)	−19.0(5)	−19.2	♢	−16.2(5)	−16.2(5)	−15.9
	−26.3(7)	/	−25.9		−22.8(5)	−22.6(8)	−22.9		−23.8(15)	−23.0(15)	−21.5
	−36.6(5)	/	/		−31.9(10)	/	/		−26.7(10)	−27.1(10)	/
	−39.6(12)	/	/		−34.4(10)	/	−37.0		/	/	/
trimer	−45.0(8)	−45.5(8)	-46.3	trimer	−38.1(8)	−37.9(5)	-38.3	trimer	−31.3(8)	−31.6(8)	−31.9

Tab. 4.5: Observed and calculated molecular resonances. The frequencies are given in MHz. Errors (2σ) of the measured binding energies are determined by the fit of the spectra (see Fig. 4.9).

5. Rydberg molecule, quo vadis?

In this work the existence of a novel type of molecule has been shown whose binding is based solely on electron-atom scattering. These molecules are composed of a Rydberg atom and a ground state atom - here Rb(ns) and Rb(5s) - where the binding arises from scattering of the Rydberg electron from the ground state atom. The ground state atom is bound to the Rydberg wavefunction, which has radii on the order of 100 nm, and thus these molecules are of long-range. Although the theoretical description of this interaction goes back to the famous work of Fermi in the year 1934 which was expanded in the following decades by Omont [5] and Greene [6], the experimental proof of their existence was still missing. Up to now, experimental evidence for the ultralong-range Rydberg molecules was found only in spectral line broadenings [3].
The present experiments have demonstrated the direct photoassociation of these ultralong-range Rydberg molecules ${}^3\Sigma(ns - 5s)$ from a cold and dense sample of ^{87}Rb atoms for a range of principal quantum numbers, n, between 34 and 40. The high-resolution photoassociation spectra allowed for the observation of several vibrational states separated by only a few Megahertz. Based on the model by Greene [6] the vibrational ground states $\nu = 0$ are assigned and the dependence of their binding energy on the principal quantum number, n, is used to extract the triplet s-wave scattering length A_0^T for electron-Rb(5s) collisions from the data [7]. The remarkably good agreement between experiment and theory for the vibrational ground state $\nu = 0$ over a range of principal quantum numbers attests to the accuracy of Fermi's original pseudopotential approach in describing interactions in excited multi-atom systems.

Aside from this good agreement for the state $\nu = 0$, the measurements also show that contributions from p-wave scattering cannot be neglected, as a number of excited vibrational states is observed in the experiment that are not predicted from the theory assuming only s-wave scattering. Calculations of Li, Pohl and coworkers have shown that a full solution of the electron-atom scattering is necessary for the assignment of all vibrational states [85]. This work finds the molecular bound states to be very sensitive to both s-wave as well as p-wave electron-atom scattering and the Rydberg molecules turn out to be an accurate experimental platform to study electron-atom collisions in a previously inaccessible ultralow-energy regime.

In general, the ultralong-range Rydberg molecules investigated here for rubidium are expected for all species with negative scattering length for electron-atom interaction, e. g. the other alkali atoms [52, 53]. Rydberg atom and ground state atom do not even have to be of the same chemical element, the only requirement is a negative scattering length of the ground state atom for electron scattering. Moreover, the binding force of the Rydberg electron is not restricted to a single ground state atom [78] and molecules with more than one ground state atom can be created. The fact that these exotic molecules have huge bond lengths but nevertheless a vibrational spectrum with several states make a new type of ultracold Rydberg chemistry feasible. In the future, larger polymers or even heteronuclear molecules can be realized, where the number of atoms, the constituent atomic elements and the addressed Rydberg state allow to precisely select the properties of the long-range molecule.

A first step in this direction is already done in this work by demonstrating the photoassociation of triatomic molecules, composed of a single Rydberg atom and two independent ground state atoms which are both bound by the Rydberg electron. They are formed for principal quantum numbers $n = 35 - 37$. For all three states the binding energy of the trimer ground state $\nu = 0$ is systematically twice the binding energy of the dimer ground state. This result confirms the model of two independently bound ground state atoms.

To further characterize the ultralong-range dimers ${}^3\Sigma(ns{-}5s)(\nu = 0)$, their Stark effect is studied for electric fields of up to 3 V/cm and principal quantum numbers $n = 35 - 37$. The molecular states show a quadratic Stark effect similar to the atomic Rydberg states which

indicates that the ground state atom does not perturb the Rydberg wavefunction. But very recent measurements at this setup at higher electric fields and with an improved laser stability ($\Delta\nu < 100$ kHz) show that there is a line broadening for the molecular states either due to the rotational structure or an anisotropy or permanent dipole moment caused by the presence of the ground state atom [50]. Perspectives of this issue will be discussed in the following chapter.
Aside from the Stark effect also the lifetimes of the molecular states are studied and compared to the atomic lifetimes. For the molecular ground states a significantly shorter lifetime is measured. Furthermore, molecular ions Rb_2^+ are identified in time-of-flight which are only detected on the molecular resonances. These data show a clear evidence for an additional decay channel related to the presence of the ground state atom within the Rydberg wavefunction. This work discusses possible decay channels and processes explaining the ion formation. The clarification of the reduced lifetimes needs an extended theoretical investigation e. g. of the tunneling of the ground state atom through the potential barrier into the inner region of the Rydberg atom.

There is a variety of future experiments and applications of the ultralong-range Rydberg molecules investigated in this work, ranging from studies of low-energy electron-atom scattering for other chemical elements to coherent control of the population of a molecular state. The Rydberg molecules could also serve as a tool for manipulating the ultracold atomic sample, e. g. to tune the atom-atom scattering length by an optical Feshbach resonance [87, 88] or to change the correlation function of the ground state atoms. In the next paragraphs three topics are discussed, starting with the investigation of the rotational structure of the molecules in Chap. 5.1. Although the rotational constants can be calculated from the expected equilibrium distances (see Chap. 2.3.1), a rotationally resolved spectrum is worthwhile, as it is a direct measure of the bond length and hence an additional confirmation of the theoretical model [89]. Furthermore, the Stark effect of the Rydberg molecules and probable experiments to investigate the rotational structure in an electric field are discussed. This paragraph already shows that there are plenty physical questions to be answered in future experiments. Another topic are the

perspectives of coherent excitation of the molecular states, which are reconsidered in Chap. 5.2, and which might give insight in coherence properties of the Rydberg states that are normally hidden by their collective excitation dynamics (see Chap. 2.1.4). In the last paragraph 5.3, the properties of high-l Rydberg molecules, the so-called trilobite molecules [6], are summarized.

5.1 Rotational structure & electric fields

The extremely large bond lengths of the Rydberg molecules are responsible for their narrow rotational spectrum: The rotational constants of the ${}^3\Sigma(ns - 5s)(\nu = 0)$ states of rubidium studied here are in the range of $B \approx 10$ kHz (see Chap. 2.3.1), and the rotational states $E_{rot}(J)$ are thermally populated up to $J = 6$ (Fig. 2.13). Thus in the measurements of this thesis, the rotational structure of the Rydberg molecules is hidden by line broadenings caused by the Doppler shift of the ground state atoms ($\Delta\nu_D = 145$ kHz) and the laser linewidth ($\Delta\nu_L \approx 800$ kHz). Currently, the stability of the laser system has been improved significantly and the combined linewidth for the Rydberg excitation could be reduced to $\Delta\nu_L \leq 100$ kHz [50]. This improvement allows to resolve the Doppler width of the vibrational states, which can be further reduced by counterpropagating laser beams instead of copropagating beams. But even if the limitation by the Doppler effect could be overcome, the rotational constants would still be smaller or at least equal to the natural linewidth $\Delta\nu_{nat} = (2\pi\tau)^{-1}$, which is $\Delta\nu_{nat} = 11$ kHz for $\tau = 15$ μs, a typical value for the molecular ground states (see Tab. 2.3). It has to be noted that this lifetime does not include blackbody induced losses, i. e. the effective lifetime of the molecular state is probably even shorter. Therefore, the determination of the rotational constant is a challenging task.

One way to reach this goal could be to utilize the splitting of the rotational levels in an electric field. Although the perturbative approach for the molecular potential curves by Greene [6] neglects the influence of the ground state atom on the Rydberg wavefunction, there has to be an effect on the Rydberg wavefunction, even if it might

be very weak. Due to the polarization of the ground state atom the probability density of the Rydberg atom will increase at the position of the ground state atom, which will lift the isotropy of the Rydberg wavefunction and lead to a permanent dipole moment μ_p as well as an anisotropy $\delta\alpha$ in the polarizability. Therefore there will be an M-dependent Stark shift of the rotational states $|J, K = 0, M\rangle$. A clear evidence for a permanent dipole moment or an anisotropy has been found in recent Stark spectra [50], but the rotational lines could not be resolved and thus a line assignment and quantitative analysis of the Stark pattern is still missing.

The full complexity of the problem of understanding the molecular Stark pattern becomes visible if one goes further and asks: *What is the influence of the polarized Rydberg wavefunction on the molecular potential, and hence on the bond length and rotational constant?*
A polarized wavefunction will lift the isotropy of the molecular potential and lead to an alignment of the molecule along the electric field axis $\vec{F}$. Moreover, the dependence of the molecular potential depth on the angle θ between the molecular axis $\vec{a}$ and the electric field direction $\vec{F}$ could give rise to another rotational motion, the so-called *pendular states* [90], which have been observed for chemically bond ground state molecules in intense laser fields [91].
To conclude, the Stark effect of the Rydberg molecules keeps many open questions ready, from the influence of the ground state atom on the Rydberg wavefunction and thus the magnitude of the dipole moment of the molecule to the question for the change of the molecular potential in the presence of an electric field and its consequences for the motional degrees of freedom of the molecule.

5.2 Coherent excitation

Another interesting topic is the coherent dynamic of the Rydberg molecules which is expected to be different from that of the atomic Rydberg states. If a number, N, of ground state atoms $|g\rangle$ are coupled to an excited state $|e\rangle$ by a laser of Rabi frequency Ω_0, the population oscillates between the states $|g\rangle$ and $|e\rangle$ with a period of $2\pi\Omega_0^{-1}$ (Fig. 5.1a). The situation changes if the excited state is

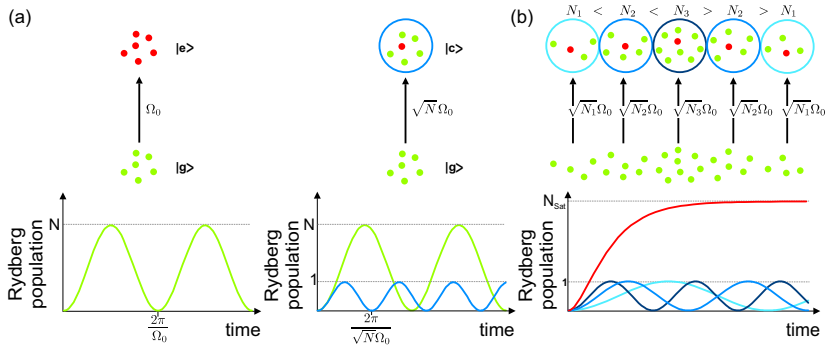

Fig. 5.1: Illustration of collective Rydberg excitation. a) Comparison of the dynamics of a single-atom excitation of N individual atoms with Rabi frequency Ω_0, and the collective excitation of N atoms caused by the Rydberg-Rydberg blockade. b)Excitation dynamics of the Rydberg population in a sample with inhomogeneous density. The Rabi oscillations of different collective frequencies $\sqrt{N}\Omega_0$ sum up to a saturation curve.

a Rydberg state: the strong Rydberg-Rydberg interaction, for $|ns\rangle$ states the isotropic van der Waals interaction, suppresses the excitation of a second Rydberg atom in the direct vicinity of a Rydberg atom. The size of the volume with just one Rydberg excitation, the blockade sphere, is determined by the coupling strength of the laser, Ω_0, and the C_6-coefficient (see Chap. 2.1.4). Due to this blockade all ground state atoms within a blockade sphere are excited collectively to the state $|c\rangle$, which is a superposition of all possible configurations with a single excitation. As a consequence, the Rabi frequency is increased by a factor $\sqrt{N}$. But as this factor depends on the density of ground state atoms, the local Rabi oscillations in a dense atomic sample sum up to a saturation curve shown in Fig. 5.1b). Thus the Rabi frequency of the driving laser cannot be determined directly from the evolution of the Rydberg population with time but has to be calculated from the slope and saturation value of the saturation curve [38, 44].

The Rabi frequency Ω_0 as well as the C_6-coefficient are characteristic properties of the Rydberg state and should not be influenced by the

presence of the ground state atom. Therefore, their values should be the same for the Rydberg molecules and atoms. The big difference in the molecular excitation dynamics will be the collectivity: N is the number of atoms within a blockade sphere that are in resonance with the addressed transition, which means for an atomic Rydberg state N is just the number of ground state atoms and for the densities in this experiment on the order of 1000 in the center of the cloud [38]. But for a molecular state, N is the number of atom pairs within a blockade sphere, whose distance matches the bond length of the addressed molecular state. This number will be much smaller and determined by the Franck-Condon factor which is on the order of 0.01. Hence the highest value for the factor $\sqrt{N}$ in a dense sample will not be $\sqrt{N_{atom}} \approx 30$ but only $\sqrt{N_{mol}} \approx 3$.

In experiments focussing on coherent dynamics, the ultralong-range Rydberg molecules could thus be considered as additional Rydberg state with essentially the same properties as the atomic Rydberg state, but with a drastically reduced collectivity. The only restriction for the coherence time is the shorter lifetime of the Rydberg molecules.
First experiments comparing the ${}^3\Sigma(36s - 5s)(\nu = 0)$ state to the atomic 36s have already shown, that the excitation dynamics of the molecular state is much slower than the atomic one [92], but the coherence times in these measurements were limited by the laser linewidth. In the current status of the setup, i. e. with an improved laser stability of $\Delta\nu_L \leq 100$ kHz, the observation of Rabi oscillations on the molecular resonance could be within reach.

5.3 Trilobites – high-l states

In this work, the formation of ultralong-range Rydberg molecules has been demonstrated for Rb(ns) states. Their binding energies are in the range of 10-30 MHz for principal quantum numbers $n = 34 - 40$. For Rydberg states with higher angular momentum l, the binding energy increases due to the factor $(2l + 1)$ in the s-wave potential (2.54), but the general shape of the molecular potential curve does not change for the non-degenerate np, nd and nf states of rubidium.

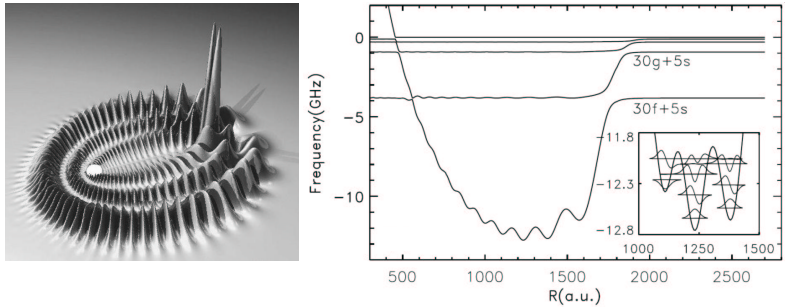

Fig. 5.2: Ultralong-range Rydberg molecule for high-l states. Pictures are taken from Ref. [6]. Left: Probability density of the hydrogen-like $n = 30$ manifold of rubidium. The ground state atom Rb(5s) is located underneath the "twin towers", the position of the ion Rb^+ is indicated as white sphere. Right: Molecular potential curves of the $^3\Sigma$ Rb_2 molecules for the $n = 30$ manifold and their lowest lying vibrational states.

In contrast, the states with high angular momentum $l \geq 3$ have no quantum defect, i. e. they are degenerate, and consequently their s-wave potential curve is given by the sum over all states of a certain n-manifold [6, 93]

$$V_s(n,r) = 2\pi \cdot A\left[k(r)\right] \sum_{l=3}^{n-1} \frac{(2l+1)}{4\pi} \left|R_{nl}(r)\right|^2 . \tag{5.1}$$

The resulting potential is much deeper than for the low-l states studied here and due to the summation over all radial probability densities $\left|R_{nl}(r)\right|^2$ in (5.1), the oscillatory character of the wavefunctions is less pronounced. The molecular potential for the states $n = 30$ in rubidium is presented in Fig. 5.2. The potential has several minima each possessing an own vibrational structure. The depth of the potential exceeds 12 GHz and is thus three orders of magnitude larger than for the $l = 0$ states. Fig. 5.2 also shows a surface plot of the Rydberg electron probability density that shows a pronounced maximum at the position of the ground state atom. Owing to its shape Chris Greene named this type of Rydberg molecule *trilobite molecule* [6].

Special about these trilobite molecules are not only their comparably large binding energies, but also their response to an electric field: The Rydberg states of a hydrogen-like manifold show a linear Stark effect, and thus although they are homonuclear, also the Rydberg molecules of these states will have a permanent dipole moment. For the trilobite molecule in Fig. 5.2 it is supposed to be $\mu_p = 313$ D (Debye) [6] which is extremely large: The most polar diatomic molecules are the alkali halides with electric dipole moments of $\mu_p = 6.28$ D for LiF up to $\mu_p = 11.69$ D for CsI [94]. The huge dipole moments of the trilobite molecules arise from the size of the Rydberg wavefunction. Furthermore, the lifetimes of the trilobite molecules around $n = 30$ are expected to be one order of magnitude larger than those of the Rydberg molecules in low-l states [6].
The selection rules do not allow transitions from the ground state Rb(5s) to the high-l states by a two-photon excitation. Hence to address the trilobite states with the current laser setup, the Rydberg excitation has to be performed in an electric field F to admix the closest lying s and d states to the high-l state.

6. Appendix

6.1 Photoassociation spectra of Rb(34s) and Rb(40s)

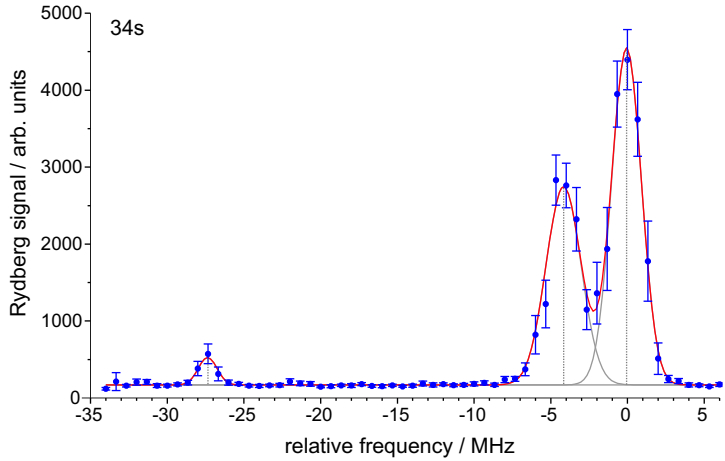

Fig. 6.1: Photoassociation spectrum of the Rb(34s) state. The spectrum is the average of 30 independent measurements and the errorbars indicate the 2σ error.

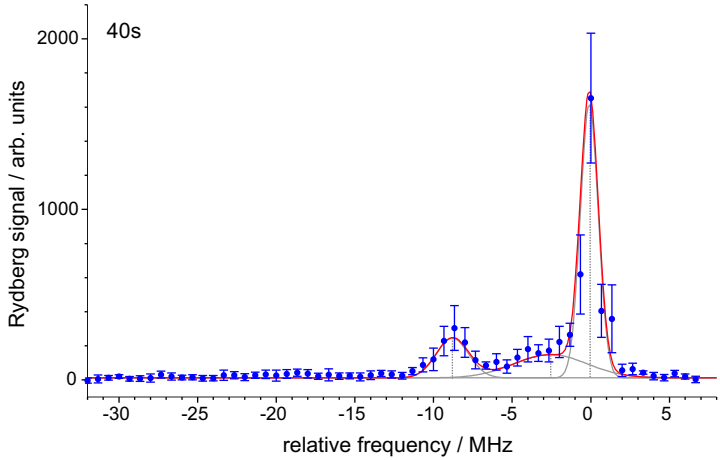

Fig. 6.2: Photoassociation spectrum of the Rb(40s) state. The spectrum is the average of 16 independent measurements and the errorbars indicate the 2σ error.

6.2 Lifetime data

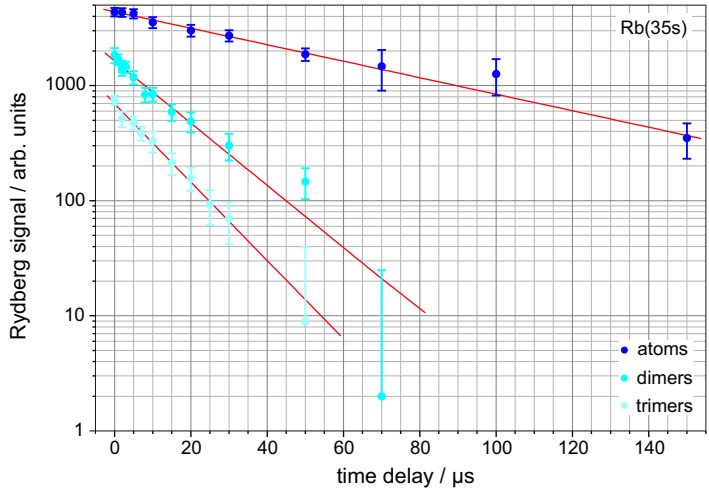

Fig. 6.3: Lifetime measurements for the Rb(35s) state. Each datapoint is the mean value of 60 independent excitations (atomic resonance) and 90 independent excitations for the molecular ground states $\nu = 0$. The errorbars indicate the 2σ error.

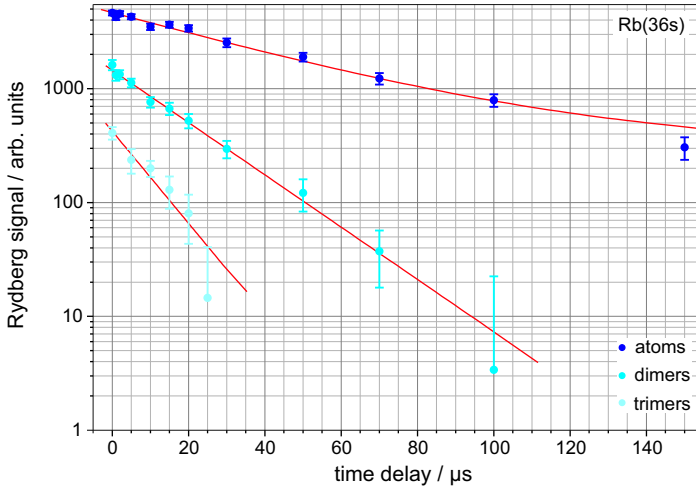

Fig. 6.4: Lifetime measurements for the Rb(36s) state. Each datapoint is the mean value of 90 independent excitations on the atomic resonance and the molecular ground states $\nu = 0$, respectively. The errorbars indicate the 2σ error.

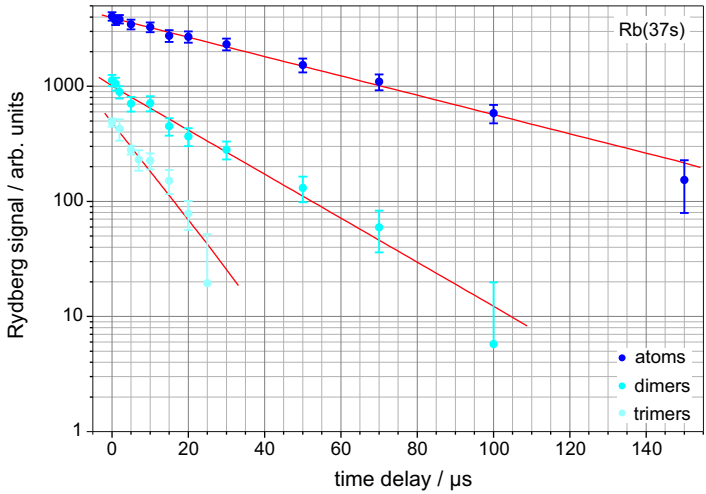

Fig. 6.5: Lifetime measurements for the Rb(37s) state. Each datapoint is the mean value of 90 independent excitations on the atomic resonance and the molecular ground states $\nu = 0$, respectively. The errorbars indicate the 2σ error.

Bibliography

[1] E. Amaldi and E. Segrè. Effetto della Pressione Sui Termini Elevati Degli Alcalini. *Nuovo Cimento*, **11**, 145–156, 1934.

[2] E. Fermi. Sopra lo spostamento per pressione delle righe elevate delle serie spettrali. *Nuovo Cimento*, **11**, 157–166, 1934.

[3] C. H. Greene, E. L. Hamilton, H. Crowell, C. Vadla, and K. Niemax. Experimental Verification of Minima in Excited Long-Range Rydberg States of Rb_2. *Physical Review Letters*, **97**, 233002, December 2006.

[4] H. Faxén and J. Holtsmark. Beitrag zur Theorie des Durchganges langsamer Elektronen durch Gase. *Zeitschrift für Physik*, **45**, 307–324, May 1927.

[5] A. Omont. On the theory of collisions of atoms in Rydberg states with neutral particles. *Journal de Physique*, **38**, 1343–1359, 1977.

[6] C. H. Greene, A. S. Dickinson, and H. R. Sadeghpour. Creation of Polar and Nonpolar Ultra-Long-Range Rydberg Molecules. *Physical Review Letters*, **85**, 2458–2461, September 2000.

[7] V. Bendkowsky, B. Butscher, J. Nipper, J. P. Shaffer, R. Löw, and T. Pfau. Observation of ultralong-range Rydberg molecules. *Nature*, **458**, 1005–1008, April 2009.

[8] S. Jochim, M. Bartenstein, A. Altmeyer, G. Hendl, S. Riedl, C. Chin, J. Hecker Denschlag, and R. Grimm. Bose-Einstein Condensation of Molecules. *Science*, **302**, 2101–2103, December 2003.

[9] C. A. Regal, C. Ticknor, J. L. Bohn, and D. S. Jin. Creation of ultracold molecules from a Fermi gas of atoms. *Nature*, **424**, 47–50, July 2003.

[10] G. Thalhammer, K. Winkler, F. Lang, S. Schmid, R. Grimm, and J. Hecker Denschlag. Long-Lived Feshbach Molecules in a Three-Dimensional Optical Lattice. *Physical Review Letters*, **96**, 050402, February 2006.

[11] Jeremy M. Sage, Sunil Sainis, Thomas Bergeman, and David DeMille. Optical Production of Ultracold Polar Molecules. *Physical Review Letters*, **94**, 203001, May 2005.

[12] S. Ospelkaus, A. Pe'er, K.-K. Ni, J. J. Zirbel, B. Neyenhuis, S. Kotochigova, P. S. Julienne, J. Ye, and D. S. Jin. Efficient state transfer in an ultracold dense gas of heteronuclear molecules. *Nature Physics*, **4**, 622–626, August 2008.

[13] E. Rutherford. The Scattering of α and β Particles by Matter and the Structure of the Atom. *Philosophical Magazine*, **21**, 669, April 1911.

[14] S. A. Lee, J. Helmcke, J. L. Hall, and B. P. Stoicheff. Doppler-free two-photon transitions to Rydberg levels: convenient, useful, and precise reference wavelengths for dye lasers. *Optical Letters*, **3**, 141–143, 1978.

[15] C.-J. Lorenzen and K. Niemax. Quantum defects of the $n^2P_{1/2,3/2}$ levels in ^{39}K I and ^{85}Rb I. *Physica Scripta*, **27**, 300, April 1983.

[16] W. Li, I. Mourachko, M. W. Noel, and T. F. Gallagher. Millimeter-wave spectroscopy of cold Rb Rydberg atoms in a magneto-optical trap: Quantum defects of the ns, np, and nd series. *Physical Review A*, **67**, 052502, May 2003.

[17] A. Sommerfeld. *Atombau und Spektrallinien*. Harry Deutsch, 1978.

[18] U. Litzén. The 5g Levels of the Alkali Metals. *Physica Scripta*, **1**, 253, 1970.

[19] Axel Grabowski. Aufbau einer Messapparatur zur Laserkühlung und hochaufgelöste Rydberg-Spektroskopie an ^{87}Rb-Atomen. *Dissertation, Universität Stuttgart*, March 2006. http://www.pi5.uni-stuttgart.de/dissertations/grabowski2006.pdf.

[20] S. A. Bhatti, C. L. Cromer, and W. E. Cooke. Analysis of the Rydberg character of the $5d7d\,^1D_2$ state of barium. *Physical Review A*, **24**, 161–165, July 1981.

[21] F. Gounand, M. Hugon, and P. R. Fournier. Radiative lifetimes of highly excited states in rubidium. *Journal de Physique*, **41**, 119–121, February 1980.

[22] F. Gounand, P. R. Fournier, J. Cuvellier, and J. Berlande. Determination of natural radiative lifetimes for highly excited P states in rubidium. *Physics Letters A*, **59**, 23–24, November 1976.

[23] M. Hugon, F. Gounand, and P. R. Fournier. Radiative lifetimes of highly excited F states in rubidium. *Journal of Physics B: Atomic Molecular Physics*, **11**, L605–L609, October 1978.

[24] F. Gounand, M. Hugon, P. R. Fournier, and J. Berlande. Superradiant cascading effects in rubidium Rydberg levels. *Journal of Physics B: Atomic Molecular Physics*, **12**, 547–553, February 1979.

[25] A. L. Oliveira, M. W. Mancini, V. S. Bagnato, and L. G. Marcassa. Measurement of Rydberg-state lifetimes using cold trapped atoms. *Physical Review A*, **65**, 031401, March 2002.

[26] V. A. Nascimento, L. L. Caliri, A. L. de Oliveira, V. S. Bagnato, and L. G. Marcassa. Measurement of the lifetimes of S and D states below n=31 using cold Rydberg gas. *Physical Review A*, **74**, 054501, November 2006.

[27] L. L. Caliri and L. G. Marcassa. Reply to "Comment on 'Measurement of the lifetimes of S and D states below n=31 using cold Rydberg gas"'. *Physical Review A*, **75**, 066503, June 2007.

[28] F. Gounand. Radiative lifetimes of highly excited states in rubidium. *Journal de Physique*, **40**, 457–460, May 1979.

[29] T. F. Gallagher. *Rydberg Atoms*. Cambridge University Press, October 1994.

[30] T. F. Gallagher and W. E. Cooke. Interactions of Blackbody Radiation with Atoms. *Physical Review Letters*, **42**, 835–839, March 1979.

[31] I. I. Beterov, I. I. Ryabtsev, D. B. Tretyakov, and V. M. Entin. Quasiclassical calculations of blackbody-radiation-induced depopulation rates and effective lifetimes of Rydberg nS , nP , and nD alkali-metal atoms with nℓ80. *Physical Review A*, **79**, 052504, May 2009.

[32] L. D. Landau and E. M. Lifschitz. *Lehrbuch der Theoretischen Physik, Band III Quantenmechanik*. Akademie-Verlag Berlin, 1979.

[33] W. H. Wing. Electrostatic Trapping of Neutral Atomic Particles. *Physical Review Letters*, **45**, 631–634, August 1980.

[34] E Vliegen and F Merkt. Stark deceleration of hydrogen atoms. *Journal of Physics B: Atomic, Molecular and Optical Physics*, **39**, L241–L247, 2006.

[35] S. D. Hogan and F. Merkt. Demonstration of Three-Dimensional Electrostatic Trapping of State-Selected Rydberg Atoms. *Physical Review Letters*, **100**, 043001, January 2008.

[36] M. S. O'Sullivan and B. P. Stoicheff. Scalar polarizabilities and avoided crossings of high Rydberg states in Rb. *Physical Review A*, **31**, 2718–2720, April 1985.

[37] D. Tong, S. M. Farooqi, J. Stanojevic, S. Krishnan, Y. P. Zhang, R. Côté, E. E. Eyler, and P. L. Gould. Local Blockade of Rydberg

Excitation in an Ultracold Gas. *Physical Review Letters*, **93**, 063001, August 2004.

[38] R. Heidemann, U. Raitzsch, V. Bendkowsky, B. Butscher, R. Löw, L. Santos, and T. Pfau. Evidence for Coherent Collective Rydberg Excitation in the Strong Blockade Regime. *Physical Review Letters*, **99**, 163601, October 2007.

[39] T. Vogt, M. Viteau, A. Chotia, J. Zhao, D. Comparat, and P. Pillet. Electric-Field Induced Dipole Blockade with Rydberg Atoms. *Physical Review Letters*, **99**, 073002, August 2007.

[40] K. Singer, J. Stanojevic, M. Weidemüller, and R. Côté. Long-range interactions between alkali Rydberg atom pairs correlated to the ns-ns, np-np and nd-nd asymptotes. *Journal of Physics B: Atomic Molecular Physics*, **38**, 295, January 2005.

[41] K. Singer. *PotCalc: Atomic Interaction Potential Calculator*. Universität Freiburg, January 2005. Available Online, http://quantendynamik.physik.uni-freiburg.de/potcalc/index.html.

[42] E. Urban, T. A. Johnson, T. Henage, L. Isenhower, D. D. Yavuz, T. G. Walker, and M. Saffman. Observation of Rydberg blockade between two atoms. *Nature Physics*, **5**, 110–114, January 2009.

[43] A. Gaetan, Y. Miroshnychenko, T. Wilk, A. Chotia, M. Viteau, D. Comparat, P. Pillet, A. Browaeys, and P. Grangier. Observation of collective excitation of two individual atoms in the Rydberg blockade regime. *Nature Physics*, **5**, 115–118, January 2009.

[44] Rolf Heidemann. Rydberg Excitation of Bose-Einstein Condensates: Coherent Collective Dynamics. *Dissertation*, *Universität Stuttgart*, March 2008. http://www.pi5.uni-stuttgart.de/dissertations/heidemann2008.pdf.

[45] R. Heidemann, U. Raitzsch, V. Bendkowsky, B. Butscher, R. Löw, and T. Pfau. Rydberg Excitation of Bose-Einstein Condensates. *Physical Review Letters*, **100**, 033601, January 2008.

[46] C. Ramsauer. Über den Wirkungsquerschnitt der Gasmoleküle gegenüber langsamen Elektronen. *Annalen der Physik*, **369**, 513–540, June 1921.

[47] C. Ramsauer. Über den Wirkungsquerschnitt der Gasmoleküle gegenüber langsamen Elektronen. II. Fortsetzung und Schluß. *Annalen der Physik*, **377**, 345–352, June 1923.

[48] J. M. Blatt and J. D. Jackson. On the Interpretation of Neutron-Proton Scattering Data by the Schwinger Variational Method. *Physical Review*, **76**, 18–37, July 1949.

[49] T. F. O'Malley, L. Spruch, and L. Rosenberg. Modification of Effective-Range Theory in the Presence of a Long-Range (r^{-4}) Potential. *Journal of Mathematical Physics*, **2**, 491–498, 1961.

[50] Jonathan Balewski. Hochauflösende Photoassoziationsspektroskopie von Rydberg-Dimeren und Trimeren. *Diplomarbeit, Universität Stuttgart*, December 2009. http://www.pi5.uni-stuttgart.de/dissertations/balewski.pdf.

[51] R. W. Molof, H. L. Schwartz, T. M. Miller, and B. Bederson. Measurements of electric dipole polarizabilities of the alkali-metal atoms and the metastable noble-gas atoms. *Physical Review A*, **10**, 1131–1140, October 1974.

[52] I. I. Fabrikant. Interaction of Rydberg atoms and thermal electrons with K, Rb and Cs atoms. *Journal of Physics B: Atomic and Molecular Physics*, **19**, 1527–1540, 1986.

[53] C. Bahrim, U. Thumm, and I. I. Fabrikant. ${}^3S^e$ and ${}^1S^e$ scattering lengths for e^- + Rb, Cs and Fr collisions. *Journal of Physics B: Atomic, Molecular and Optical Physics*, **34**, L195–L201, 2001.

[54] C. Bahrim and U. Thumm. Low-lying ${}^3P^o$ and ${}^3S^e$ states of Rb^-, Cs^-, and Fr^-. *Physical Review A*, **61**, 022722, January 2000.

[55] R. J. Le Roy. *LEVEL 8.0: A Computer Program for Solving the Radial Schrödinger Equation for Bound and Quasibound Levels.* University of Waterloo Chemical

Physics Research Report CP-663, 2007. Available Online, http://leroy.uwaterloo.ca/programs/.

[56] W. Demtröder. *Molekülphysik*. Oldenbourg Verlag, 2003.

[57] F. Engelke. *Aufbau der Moleküle*. B. G. Teubner Stuttgart, 1996.

[58] H. Kroto. *Molecular Rotation Spectra*. John Wiley & Sons, 1975.

[59] Schawlow A. L. Townes, C. H. *Microwave Spectroscopy*. Dover Publications, 1975.

[60] S. Golden and Jr. E. Bright Wilson. The Stark Effect for a Rigid Asymmetric Rotor. *The Journal of Chemical Physics*, **16**, 669–685, 1948.

[61] K. M. Jones, E. Tiesinga, P. D. Lett, and P. S. Julienne. Ultracold photoassociation spectroscopy: Long-range molecules and atomic scattering. *Review of Modern Physics*, **78**, 483–535, May 2006.

[62] Boris M. Smirnov. *Physics of Atoms and Ions*. Springer-Verlag Heidelberg, 2003.

[63] Ulrich Raitzsch. Aufbau einer UHV-Kammer zur Durchführung von Experimenten mit Bose-Einstein-Kondensaten in optischen Gittern. *Diplomarbeit*, *Universität Stuttgart*, December 2004. http://www.pi5.uni-stuttgart.de/dissertations/raitzsch.pdf.

[64] Robert Löw. A versatile setup for experiments with Rubidium Bose-Einstein condensates: From optical lattices to Rydberg matter. *Dissertation*, *Universität Stuttgart*, December 2006. http://www.pi5.uni-stuttgart.de/dissertations/loew2006.pdf.

[65] Helmar Bender. Mikrowellen-Anregung von ultrakalten Atomen. *Diplomarbeit*, *Universität Stuttgart*, December 2006. http://www.pi5.uni-stuttgart.de/dissertations/bender.pdf.

[66] S. Bize, Y. Sortais, M. S. Santos, C. Mandache, A. Clairon, and C. Salomon. High-accuracy measurement of the ^{87}Rb ground-state hyperfine splitting in an atomic fountain. *Europhysics Letters*, **45**, 558–564, March 1999.

[67] B. K. Teo, D. Feldbaum, T. Cubel, J. R. Guest, P. R. Berman, and G. Raithel. Autler-Townes spectroscopy of the $5S_{1/2} - 5P_{3/2} - 44D$ cascade of cold ^{85}Rb atoms. *Physical Review A*, **68**, 053407, November 2003.

[68] A. Grabowski, R. Heidemann, R. Löw, J. Stuhler, and T. Pfau. High resolution Rydberg spectroscopy of ultracold rubidium atoms. *Fortschritte der Physik*, **54**, 765–775, August 2006.

[69] A. K. Mohapatra, T. R. Jackson, and C. S. Adams. Coherent Optical Detection of Highly Excited Rydberg States Using Electromagnetically Induced Transparency. *Physical Review Letters*, **98**, 113003, 2007.

[70] D. A. Steck. *Rubidium 87 D Line Data*. University of Oregon, August 2009. Available Online, http://steck.us/alkalidata/.

[71] Björn Butscher. Kollektive kohärente Anregung von ultrakalten Rydberg-Atomen. *Diplomarbeit, Universität Stuttgart*, June 2007. http://www.pi5.uni-stuttgart.de/dissertations/butscher.pdf.

[72] D. J. McCarron, S. A. King, and S. L. Cornish. Modulation transfer spectroscopy in atomic rubidium. *Measurement Science and Technology*, **19**, 105601, 2008.

[73] U. Raitzsch, V. Bendkowsky, R. Heidemann, B. Butscher, R. Löw, and T. Pfau. Echo Experiments in a Strongly Interacting Rydberg Gas. *Physical Review Letters*, **100**, 013002, January 2008.

[74] W. C. Stwalley, Y.-H. Uang, and G. Pichler. Pure Long-Range Molecules. *Physical Review Letters*, **41**, 1164–1167, October 1978.

[75] R. E. Grisenti, W. Schöllkopf, J. P. Toennies, G. C. Hegerfeldt, T. Köhler, and M. Stoll. Determination of the Bond Length and Binding Energy of the Helium Dimer by Diffraction from a Transmission Grating. *Physical Review Letters*, **85**, 2284–2287, September 2000.

[76] J. Léonard, M. Walhout, A. P. Mosk, T. Müller, M. Leduc, and C. Cohen-Tannoudji. Giant Helium Dimers Produced by Photoassociation of Ultracold Metastable Atoms. *Physical Review Letters*, **91**, 073203, August 2003.

[77] K. R. Overstreet, A. Schwettmann, J. Tallant, D. Booth, and J. P. Shaffer. Observation of electric-field-induced Cs Rydberg atom macrodimers. *Physical Review Letters*, **88**, 133004, March 2002.

[78] I. C. H. Liu and J. M. Rost. Polyatomic molecules formed with a Rydberg atom in an ultracold environment. *European Physical Journal D*, **40**, 65–71, October 2006.

[79] M. Chéret, L. Barbier, W. Lindinger, and R. Deloche. Penning and associative ionisation of highly excited rubidium atoms. *Journal of Physics B: Atomic Molecular Physics*, **15**, 3463–3477, October 1982.

[80] L. Barbier and M. Chéret. Experimental study of Penning and Hornbeck-Molnar ionisation of rubidium atoms excited in a high s or d level ($5d \leq nl \leq 11s$). *Journal of Physics B: Atomic Molecular Physics*, **20**, 1229–1248, March 1987.

[81] A. A. Mihajlov and R. K. Janev. Ionisation in atom-Rydberg atom collisions: ejected electron energy spectra and reaction rate coefficients. *Journal of Physics B: Atomic Molecular Physics*, **14**, 1639–1653, May 1981.

[82] L. Barbier, M. T. Djerad, and M. Chéret. Collisional ion-pair formation in an excited alkali-metal vapor. *Physical Review A*, **34**, 2710–2718, October 1986.

[83] Y.-T. Lee and B. H. Mahan. Photosensitized Ionization of Alkali-Metal Vapors. *The Journal of Chemical Physics*, **42**, 2893–2896, April 1965.

[84] M. Ciocca, M. Allegrini, E. Arimondo, C. E. Burkhardt, W. P. Garver, and J. J. Leventhal. Negative-ion formation in Rydberg atom interactions (n=7-40). *Physical Review Letters*, **56**, 704–707, February 1986.

[85] V. Bendkowsky, B. Butscher, J. Nipper, J. Balewski, J. P. Shaffer, R. Löw, T. Pfau, W. Li, J. Stanojevic, T. Pohl, and J. M. Rost. *Rydberg trimers and excited dimers bound by internal quantum reflection.* December 2009. submitted, http://arxiv.org/abs/0912.4058.

[86] E. L. Hamilton, C. H. Greene, and H. R. Sadeghpour. LETTER TO THE EDITOR: Shape-resonance-induced long-range molecular Rydberg states. *Journal of Physics B: Atomic Molecular Physics*, **35**, L199–L206, May 2002.

[87] John L. Bohn and P. S. Julienne. Prospects for influencing scattering lengths with far-off-resonant light. *Physical Review A*, **56**, 1486–1491, Aug 1997.

[88] M. Theis, G. Thalhammer, K. Winkler, M. Hellwig, G. Ruff, R. Grimm, and J. Hecker Denschlag. Tuning the Scattering Length with an Optically Induced Feshbach Resonance. *Physical Review Letters*, **93**, 123001, Sep 2004.

[89] S. D. Hogan and F. Merkt. A New Perspective on the Binding Power of an Electron. *ChemPhysChem*, **10**, 2931–2934, October 2009.

[90] J. M. Rost, J. C. Griffin, B. Friedrich, and D. R. Herschbach. Pendular states and spectra of oriented linear molecules. *Physical Review Letters*, **68**, 1299–1302, Mar 1992.

[91] H. Sakai, C. P. Safvan, J. J. Larsen, K. M. Hilligsøe, K. Hald, and H. Stapelfeldt. Controlling the alignment of neutral molecules by a strong laser field. *The Journal of Chemical Physics*, **110**, 10235–10238, 1999.

[92] B. Butscher. Unpublished data.

[93] B. E. Granger, E. L. Hamilton, and C. H. Greene. Quantum and semiclassical analysis of long-range Rydberg molecules. *Physical Review A*, **64**, 042508, October 2001.

[94] K. P. Huber and G. Herzberg. *Molecular Spectra and Molecular Structure, IV. Constants of Diatomic Molecules.* van Nostrand Reinhold Company, 1979.

Danksagung

Zu dem Erfolg dieser Arbeit haben eine ganze Reihe von Menschen beigetragen, denen ich an dieser Stelle danken möchte.

Zunächst danke ich Tilman Pfau für die Aufnahme in die Arbeitsgruppe und die Unterstützung während der Zeit der Doktorarbeit. Auch für seine richtige Einschätzung der Messungen und die Entscheidung, die Ergebnisse bei Nature einzureichen, bin ich ihm sehr dankbar. Diese Kühnheit hätte ich wohl nicht besessen.

Außerdem muß ich dem gesamten Rydberg-Team für seine Vorarbeiten und die Unterstützung danken:

- Axel und Rolf, die die ersten Rydberg-Experimente gemacht haben und von denen ich viel gelernt habe.
- Robert und Ulrich für die eigenwillige, aber solide BEC-Apparatur.
- Dem Team am Experiment Björn, Johannes und Jonathan für die tatkräftige Unterstützung bei den Messungen, die vielen Diskussionen und den Spaß bei der Arbeit. Björn möchte ich außerdem für sein Engagement bei der Auswertung, seine kryptischen Matlab-Skripte und die Unterstützung beim Paperschreiben danken. Dank Johannes, dem anderen "Südschweden" am Experiment, war die Heimat nicht ganz so fern. Jonathan: Danke für die vielen kritischen Fragen und Deinen Enthusiasmus ("Also die Moleküle sind hübsch.").

Ein großer Dank geht auch an Jim Shaffer, der während meiner Messungen Gast am Institut war. Er hat mir beim theoretischen Verständis sehr weitergeholfen und viel Know-How zur Berechnung der Molekülzustände beigesteuert.

Auf der theoretischen Seite möchte ich mich außerdem bei Weibin Li, Thomas Pohl und Jan Michael Rost vom Max-Planck Institut in Dresden für die fruchtbare Zusammenarbeit bedanken.

An alle Mitglieder des Instituts ein Dankeschön für die Hilfsbereitschaft und die freundschaftliche Atmosphäre.

Herr Schumacher war sofort bereit, den Beisitz der Prüfung zu übernehmen und in so kurzer Zeit das Gutachten zu erstellen, wofür ich ihm nochmals danken möchte.

Schließlich möchte ich mich bei meinen Freunden und meiner Familie für den Rückhalt während der Hochs und Tiefs der letzten vier Jahre bedanken. Insbesondere bei Stephan, der immer ein offenes Ohr für mich hatte und mich fachlich und moralisch sehr unterstützt hat.
Ein ganz herzlicher Dank geht an meinen Freund Björn. Danke für Deine Unterstützung, die Ablenkung und Dein Verständnis während der nervenaufreibenden Phase des Schreibens dieser Arbeit.

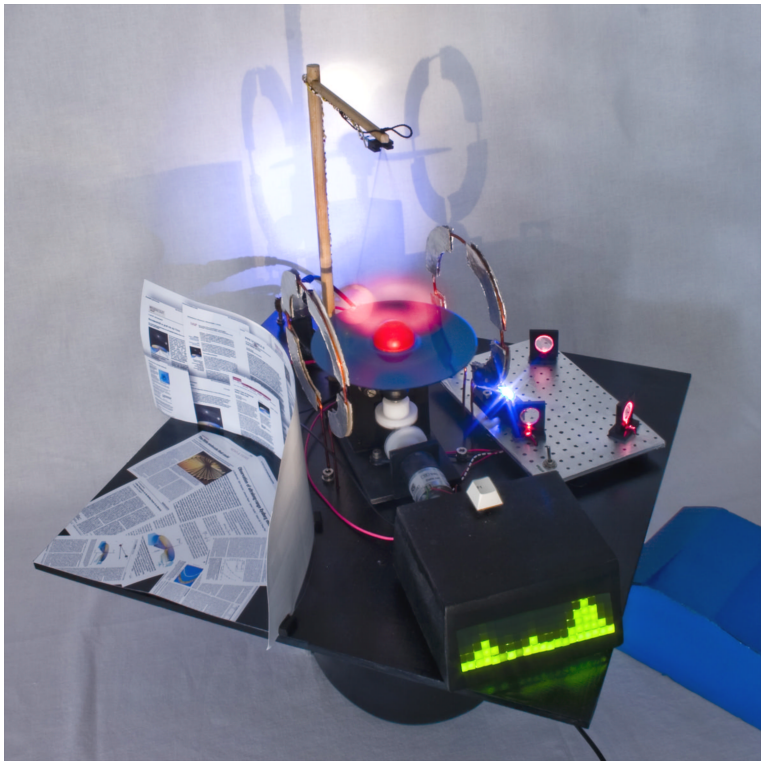

"Decades ago, chemists and physicists identified the various types of molecular bonding that are possible, including the standard ionic and covalent schema presented today in every introductory chemistry text. In the meantime, most practitioners of quantum chemistry have meandered on to larger species with the goal of predicting and elucidating the properties of huge molecules containing dozens, hundreds or even thousands of atoms. Yet the simplest molecules of all, the diatomics, which have a mere two atoms, still present puzzles and surprises. A case in point is the beautiful experiment by Bendkowsky et al. (...). The authors used the delicate techniques of ultracold atomic physics to create and detect molecules made up of two rubidium atoms that are bound together by a ghostly quantum-mechanical force field at distances as large as 100 nanometres - greater than the size of a small virus.
The interaction depends on one of the partners being a Rydberg atom - an atom in an excited state with at least one electron having a high principal quantum number, meaning that it roams far from its parent nucleus. (...) In Bendkowsky and colleagues experiment, it is a distant rubidium atom in its ground (lowest-energy) state that this spirited Rydberg pup keeps from drifting away; and the spectroscopic signature measured precisely in laser-light absorption is strong evidence that the atom is in fact trapped and vibrating back and forth in a delicate potential well as one member of a diatomic molecule. The measured vibrational binding energy, in temperature units, is only around 1 millikelvin, or 4 billionths of an electronvolt, which explains why, in practice, such a molecule can be formed only in an ultracold experimental environment."

Chris H. Greene, Nature 458, p. 975 (2009)